UNIVERSITY OF BIRMINGHAM

An Investigation of the Microscale Geometry and Liquid Flow through an Isolated Foam Channel Network

Christopher Richard Clarke

A thesis submitted to
The University of Birmingham
for the degree of
DOCTOR OF PHILOSOPHY

School of Chemical Engineering
College of Engineering and Physical Sciences
The University of Birmingham
2020

Abstract

Liquid foams represent an extremely diverse and highly functional form of soft matter, whose application is widespread throughout industry. These can range from luxurious and low calorie applications in food and beverages, structural and insulating properties in building and manufacture, right through to dynamic and transport abilities in the petrochemical industry, among others. A common feature of all of these foams is they are required to exhibit longevity, however as foams are thermodynamically unstable systems, this is not always a trivial feat.

Foams are highly complex systems, with dynamic processes occurring on the molecular scale that influence properties at the scale of individual bubbles and subsequently at the macroscopic scale of bulk foams. A particular challenge of foam research is to unite these length scale processes, requiring robust theoretical and experimental studies to be made at all size regimes. This PhD thesis is concerned specifically with the microscale process of liquid flow between bubbles, as these liquid channels form the primary network through which liquid 'drains' through a foam under the force of gravity; one of the key mechanisms governing foam instability.

The initial focus of this PhD thesis was the design and implementation of an experimental technique to isolate and image liquid foam channels formed under controlled liquid flow rates. This was developed with a view to producing highly accurate and reproducible measurements of the channel geometries, which would enable the comparison to theory derived to describe such systems.

Measurements of low molecular weight surfactants and higher molecular weight emulsifiers clearly demonstrated three previously unseen geometries of foam channel that could not be

described using existing theory. Instead, a new geometric model was developed which was able to account for these differences, relating the bulk and surface properties of the foam channel to its length and the rate of liquid flow passing through it. When used as a fitting parameter, the new model was able to clearly demarcate between the characteristic low and high surface viscosities of the surfactant and emulsifier species respectively.

The surface viscosity of the surfactant foam channel interfaces was examined throughout this PhD study, as the values extracted from model fitting were consistently lower than the majority found in literature, but in line with predictions made from hyper-sensitive measurement techniques. Ultimately, it was proposed that these differences could be attributed to a combination of the limited measurement sensitivity of commercial systems, combined with a liquid flow velocity dependence of surfactant concentration at the channel surface.

It was suggested that, in the case of low molecular weight surfactants, a surface tension gradient can exist along the length of a foam channel, that is dependent upon the rate of liquid flow, the concentration of surfactant and the rate of surfactant adsorption to the interface. In the case of high liquid flow velocities, it was shown that surface tensions in some channel regions could be almost as high as pure water, despite surfactant concentrations being above the CMC. As such, this could have significant consequences for stability in macroscopic foams where these conditions are present.

Dedication

To Delia, whose ability to tolerate my unrelentingly single-track mind, incessant self-doubt and general insanity throughout this process has been nothing short of miraculous. I am forever in your debt.

Acknowledgements

Firstly, I would like to thank my supervisors, Prof. Ian Norton, Dr. Fotis Spyropoulos and, for the first half of the battle, Dr. Aris Lazidis. Despite claiming, during my initial interview, that I would start a science themed coffee shop with the fruits of my labour, Ian still took me on and has since been instrumental in providing me with opportunities to challenge myself as a person and a researcher. I still cannot guarantee that the *café Scientifique* will not one day open its doors. Fotis, I thank you for the countless hours of pouring over the minute details of my work, alongside your unofficial roles as music advisor and navigator of the University financial systems. Your constant reassurance has been invaluable throughout this process, not to mention the hard rock. And to Aris, my Post-Doctoral supervisor and team mate, thank you for taking a lab inexperienced physicist and showing him the way of the Chemical Engineer with your practical wizardry. Here's to many future projects and schemes together.

From the financial side, I would like to acknowledge the EPSRC for funding my time here, without which this could never have happened. I would also like to further thank my supervisors in this regard, for trusting me with a range of paid project work that has provided me with a wealth of industry and technical experience.

I could not possibly give thanks without mentioning my various friends and colleagues who have been with me throughout this process. All of you have helped me to bare the, sometimes gruelling, process with your good humour and bottomless optimism. I couldn't have asked for a finer bunch to do this with.

To my parents, I would like to promise that this is the last studying I will be doing and I will now be living a grown up lifestyle; however, we all know I can't guarantee that. Without you

I could never have followed my dream of doing this and I will be eternally grateful for all of your love and support.

Finally, to Delia, to whom this thesis is dedicated, my thanks alone are not nearly enough. I hope you will always be there to challenge me to be my best and I look forward to a lifetime of adventures together.

Table of Contents

List of Illustrations

List of Tables

Nomenclature

Symbols

B_0	Boussinesq Number (or Inverse Mobility)
$C_{wt\%}$	Weight Percent Concentration
C_0	Initial Bulk Liquid Emulsifier Concentration
D	Viscous Flow Parameter
d	Plateau Border Profile Width
D_s	Emulsifier Diffusion Coefficient
$\hat{F}_1$	Dimensionless Marangoni Force
H	Channel Width
h	Tripod Frame leg height
I	Inertial Flow Parameter
L	Plateau Border Relaxation Length
L_c	Capillary Length
l_1	Upper Plateau Border Length
m	Straight Line Gradient
M	Molar Mass

n	Ideal Ionic Activity Correction Factor
P_e	Péclet Number
Q	Liquid Flow Rate
Q_{crit}	Critical Liquid Flow Rate
R	Plateau Border Radius
R_0	Plateau Border Initial Radius
R_D	Plateau Border Radius Measured in Cylindrical Region
R_e	Plateau Border Equilibrium Radius
R_{eH}	Reynolds Number for Thin Filmed Plateau Border
S	Plateau Border Cross-Sectional Area
S_e	Plateau Border Equilibrium Cross-Sectional Area
S_{Exp}	Plateau Border Minimum Expansion Cross-Sectional Area
S_{min}	Plateau Border Minimum Cross-Sectional Area
t	Time
T	Temperature
u	Point Liquid Flow Velocity
U	Average Liquid Flow Velocity of PB Horizontal Cross-Section
U_0	Vertical Channel Flow Velocity Relative to Immobile Interface
V	Average Liquid Flow Velocity of Vertical PB Profile Region
w	Film thickness
x	Tripod Frame Central Axis to Leg Distance
y	Tripod Frame Leg-to-Leg Inner Edge Separation
Y	Horizontal Distance Axis (image focal plane)
Z	Vertical Distance Axis
Z_D	Cylindrical to Ideal PB Cross-Section Transition Length

Z_{offset}	Z-axis Zero Offset
Z_{swell}	Distance between Distortion and Liquid Injection Nozzle
Z_T	Geometric PB Expansion Vertical Zero Offset
α	Ratio of Surface Dilational to Surface Shear Viscosities
Φ_e	Plateau Border Expansion Fraction
Γ_e	Equilibrium Surface Excess
Γ_{SDS}	Interfacial Concentration of SDS
Γ_m	Limiting Surface Excess
Γ_{max}	Average Max. Available Moles of SDS per Unit of PB Interfacial Area
γ	Surface Tension
γ_0	Pure Solvent Surface Tension
γ_e	Equilibrium Surface Tension
γ_{LT}	Long Time Approximation for Dynamic Surface Tension
γ_{ST}	Short Time Approximation for Dynamic Surface Tension
$\dot{\gamma}_s$	Liquid Shear Rate
μ	Dynamic Viscosity
μ_s	Apparent Surface Viscosity
ν	Kinematic Viscosity
ρ	Liquid Density
τ_{Res}	Average Surfactant Residence Time in PB
τ_γ	Characteristic adsorption time

Constants

c	Geometric Constant $= \sqrt{3} - \pi/2 \approx 0.161$
g	Acceleration due to Gravity = 9.81 m/s^2
R_g	Molar Gas Constant

Abbreviations

DOH	Dodecanol
DST	Dynamic Surface Tension
CCD	Charge Coupled Device
CMC	Critical Micelle Concentration
HPP	Hydrolysed Pea Protein
HPMC	Hydroxypropyl Methylcellulose
IIA	Ideal Ionic Activity
LMWS	Low Molecular Weight Surfactant
PB	Plateau Border
SDS	Sodium Dodecyl Sulfate
TTAB	Tetradecyltrimethylammonium Bromide
T20	Tween 20
T80	Tween 80
W-T	Ward-Tordai

Chapter 1

An Introduction to the Research and Layout of this PhD Thesis

1.1 Context for this Study

The simple incorporation of gas bubbles into a liquid system can have the ability to dramatically alter its physical properties and potential applications. Foams exists in a massively diverse range of industrial applications, from foods to construction, petrochemical to medicine and cosmetics. The reason for their wide uptake throughout these industries is their unique structural characteristics, which can be tailored based on the formulation and incorporation of gas under a range of conditions. Whether the aim is to create luxurious foods and beverages or highly efficient insulation in eco-friendly buildings, the scope for innovation in foams continues to expand.

Despite their many positives as a functional material, foams represent an extremely complex medium, which in their liquid form are often highly unstable. In cases where foams may be undesirable, such as during the processing of various liquids, this is beneficial; however, in the majority of cases where foam stability is required, this represents a significant problem.

Controlling foam stability is a major area of academic and industrial research, where solutions to the fundamental thermodynamic instability of liquid foams are sought. Whether this is to create a long lasting beer head that appeals to consumers, or efficiently extract minerals during froth flotation; there is a need to understand the dynamic processes that underpin the inevitable collapse of these systems. Ultimately, these processes will only be truly controlled by forming a complete understanding of foam dynamics from the nanoscale interaction of molecular ingredients; the microscale interaction bubbles and liquid channels; right up to the macroscale properties of bulk foams.

1.2 Motivation

The study of liquid flow at the microscale in-between bubbles of foam is currently based primarily on theoretical modelling, with very little in the way of direct experimental observation in the literature. This has largely been due to difficulties in controlling and measuring these systems in macroscopic foams. The motivation for this study is to be able to add to the current bulk of experimental observation of these microscale systems, therefore better informing microscale drainage theory and thus the overall understanding of macroscopic foam drainage.

1.3 Aim and Objectives

The ultimate aim of this thesis is to create a measurement technique that is capable of analysing the microscale flow through liquid foam channels under strictly controlled conditions. By deliberately isolating these foam channels and studying their structures under forced liquid flow rates, it is hypothesised that simple geometric measurements could be used to describe the relationship between bulk liquid and interfacial flow dynamics. Overall, this research would add to the limited body of experimental observations made of liquid foam channels and aid in providing a more complete understanding of microscale foam drainage. As this research is funded as part of the EPSRC's Centre for Innovative Manufacturing in Food (CIM) at the University of Birmingham, a particular focus will be paid towards food grade liquid formulations, although the author feels that this does not limit the applicability of this research to other industries. The key research objectives of this thesis can therefore be broken down as follows:

- Design and build an experimental setup capable of producing, and capturing high-resolution images of, isolated liquid foam channels in controlled arrangements and at controlled liquid flow rates.

- Develop a theoretical background capable of accurately describing the microscale geometries of liquid foam channels based on the bulk liquid flow and interfacial properties.

- Examine the relationship between surface rheology and bulk liquid flow for a range of formulations, with an emphasis on those with particular relevance to the food industry.

- To better understand the impact of liquid flow on the stabilising action of chemical emulsifiers and how this may ultimately affect stability in macroscopic foam systems.

1.4 Thesis Layout

This thesis follows the alternative thesis format of the University of Birmingham, where results chapters (Chapters 4-6) are either published or under review by peer-reviewed journals.

Chapter 2. This chapter provides an introduction to the subject of liquid foams and foam stability in the literature, with an emphasis on foam systems relevant to the food industry. A more comprehensive review of the literature relating to foam drainage follows.

Chapter 3. This chapter describes the design and development of the experimental setup, the 'PB-Node Setup', used throughout this thesis to gather experimental data on foam channel geometries and apply theory developed to describe these systems.

Chapter 4. This chapter describes the application of existing theory describing microscale foam geometries to experimental data for formulations of Sodium Dodecyl Sulfate (SDS) at controlled liquid flow rates and channel lengths. The results of this study demonstrated the existence of a previously unseen microscale channel geometry, which could not be described by existing theory. It was shown that foam channel length and liquid flow rate directly influenced the channel geometry. This work has been published under the title: 'Measuring the Impact of Channel Length on Liquid Flow through an Ideal Plateau Border and Node System' (Clarke *et al.*, 2019).

Chapter 5. This chapter derives a new theory to describe the geometries of isolated foam channels and demonstrates its ability to fit well to experimental profiles for a range of food grade liquid formulations. An additional, previously unseen, microscale channel geometry was observed for formulations of high molecular weight emulsifiers. The length dependence of channel geometries is attributed to the geometry and position of the adjoining node in relation to the equilibrium geometry of the foam channel. This work has been published under the title: 'Surface Rheological Measurements of Isolated Food Foam Systems' (Clarke *et al.*, 2019).

Chapter 6. This chapter describes an extension of the method and theory developed in Chapter 5, to incorporate the adsorption dynamics of surfactant molecules. This study demonstrates how the rate of surfactant adsorption could lead to a non-uniform surface tension along foam channel interfaces that varies with liquid flow rate. This provides an initial indication that the stability of macroscopic foams could be inhibited by high velocity liquid flow through its foam channels, as is often the case both during and shortly after foam

formation. This work has been published under the title: 'A Flow Velocity Dependence of Dynamic Surface Tension in Plateau Borders of Foam' (Clarke *et al.*, 2020).

Chapter 7. This chapter provides a summary of the key research findings of this thesis, along with proposals for future studies that could be conducted as a continuation of this work.

Appendix A. This appendix contains details of the Matlab code used to process data from the 'PB-Node' experimental setup.

1.5 Publications and Presentations

1.5.1 Publications

- C. Clarke; A. Lazidis; F. Spyropoulos; I. T. Norton, Measuring the Impact of Channel Length on Liquid Flow through an Ideal Plateau Border and Node System, *Soft Matter* **2019**, *15*, 1879-1889.

- C. Clarke; F. Spyropoulos; I. T. Norton, Surface Rheological Measurements of Isolated Food Foam Systems, *Physics of Fluids* **2019**, *31*, 092002.

- C. Clarke; F. Spyropoulos; I. T. Norton, A Flow Velocity Dependence of Dynamic Surface Tension in Plateau Borders of Foam, *Journal of Colloid and Interface Science* **2020**, *573*, 348-359.

1.5.2 Presentations

- C. Clarke; A. Lazidis; F. Spyropoulos; I. T. Norton, Foam Drainage: Microscale Flow in an Ideal System, *EPSRC CIM in Food 2nd Annual Conference,* Birmingham, 2017.

- C. Clarke; A. Lazidis; F. Spyropoulos; I. T. Norton, Food Foams on the Microscale, *Food Matters Live,* London, 2017.

- C. Clarke; A. Lazidis; F. Spyropoulos; I. T. Norton, Food Foams on the Microscale, *17th Food Colloids Conference,* Leeds, 2018.

- C. Clarke; A. Lazidis; F. Spyropoulos; I. T. Norton, Foam Drainage: Microscale Flow in an Ideal System, *EPSRC CIM in Food 3rd Annual Conference,* Nottingham, 2018.

- C. Clarke; F. Spyropoulos; I. T. Norton, Measuring the Interfacial Rheology of Soluble Surfactants using controlled Foam Plateau Border and Node Geometries, *8th International Symposium on Food Rheology,* Zurich, 2019.

Chapter 2

An Introduction to Liquid Foams and Review of the Existing Literature.

2.0 Abstract

The aim of this literature review has been to provide an introduction to aqueous foams, with a basic overview of the physical and chemical aspects relating to their production and eventual decay. In particular, this work has focused on the destabilising role played by liquid drainage, with a more in depth discussion of the current theoretical and experimental work that has sought to describe and characterise two-phase aqueous foam systems. A more specific background relating to each of the sections of this thesis is given in the introduction to each of the experimental chapters.

2.1 An Introduction to Aqueous Foams

The formation of a foam is a fascinating phenomenon, wherein a simple liquid is transformed into an expansive and complex dynamic structure. In its most simplistic sense, a liquid foam is a dispersion of gas in a liquid where the tightly packed gas bubbles occupy most of the volume[1]. An example of a so-called two-phase foam can be seen in Figure 2.1, where the continuous phase (or 'matrix') surrounds the discrete phase of gas bubbles. In reality, things are rarely this simple, with the liquid phase often incorporating additional discrete particles and/or exhibiting viscoelastic characteristics due to its chemical composition[2]. Indeed, Berkman*, et al.*[3] state that it can only be produced in systems possessing the proper combination of surface tension, viscosity, volatility, and concentration of solute or suspended solids[4].

Overall, these systems are unique in their structural characteristics, giving them a diverse range of applications across different industries, from petrochemical[5] through to food[6], fire-

fighting[7], healthcare[8] and many others. One thing that unites all of these foams, however, is their fundamental complexity, and the need for researchers to break this down in order to optimise their production and functionality.

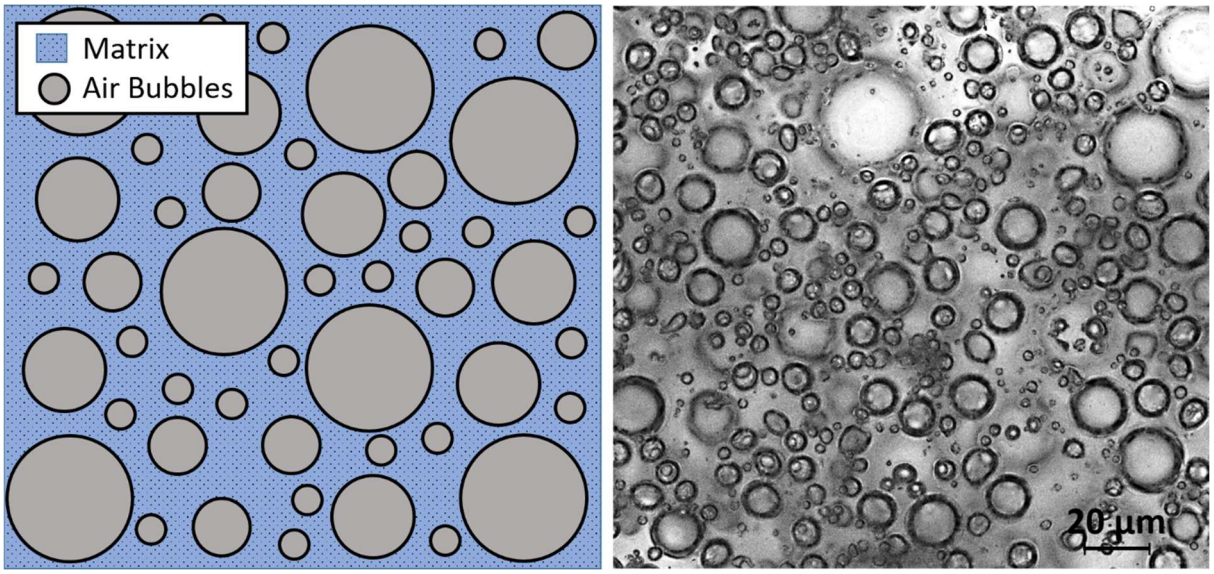

Figure 2.1. Simple two-phase foam schematic and micrograph of a commercial confectionary foam.

2.2 Industrial Example: Foams in the Food and Beverage Industry

While foams in general have been the subject of intensive research for many years, the application of theory to foams in the food industry is often secondary. In this regard, food foams tend to be formulated largely by a trial and error, 'top-down', approach with theory applied during their subsequent characterisation. This being said, significant improvements have been made in the last 20 years since Campbell*, et al.*[9] noted in 1999 that in many cases a quantitative understanding of aerated foods was distinctly lacking. Much of this work has been to do with the action of chemical stabilisers such as proteins at the bubble interfaces[10],

however, there remains significant gaps, especially when it comes to uniting the quantitative understanding of such molecular scale interactions with macroscopic foam dynamics.[11]

The need to understand these systems is becoming a matter of increasing importance in the food industry, with new formulations and structures being investigated for their often remarkable properties. Just a few of these benefits include reduced product density, improvements in texture, mouthfeel and appearance, as well as increased absorbance and control of digestibility[12]. The inherent increase in surface area and ability to encapsulate gases can also have a significant impact on flavour release through a variety of mechanisms[13]. This may include the gradual release of flavour volatiles with foam collapse, such as hop aromas being released from a beer head (a highly sought after characteristic in the brewing industry), and the possibility of either intensified *or* reduced flavour perception[9].

Campbell*, et al.*[9] identify seven broad groups of what they call 'aerated foods' that they categorise as follows:

- Beverages[14,15]
- Baked products[15,16]
- Other cereal-based products[17]
- Dairy products[16,18]
- Egg products[15]
- Chocolate and confectionary products[16,19]
- Others; e.g. sorbets, vegetable paste foams…

With the exception of most cereal-based products, this list demonstrates aerated foods that at least *begin* as liquid foams, therefore showcasing the extreme variability of chemical

compositions and structures available. As such, it is the job of researchers to understand such systems and thus provide the basis for innovation that can reflect and meet increasing consumer demands.

One example of such demands, is the increasingly environmentally and health conscious western public, which is driving a major trend towards green label, eco-friendly products[20]. In this case, long-standing, highly functional ingredients, often animal or synthetic in origin, are beginning to be replaced with plant-based alternatives. Notable examples include the replacement of gelatine with plant-based polysaccharides[21], or egg white proteins with proteins derived from different legumes[22]. Such substitutions to existing products require an in-depth understanding of the physicochemical role of each ingredient in order to find a suitable replacement that does not alter consumer perception in any way. This understanding must extend to the complex interaction of multiple ingredients in a range of processing environments, as well as to post-production, where stability of the foam system becomes a key concern. Therefore, it is clear that the existing 'top-down' approach to foam design must begin to give way to a more 'bottom-up' approach of tailored formulation.

2.3 Fundamentals of Foam Structure

There are *many* variables at work within a foam structure that produce its final characteristics, with contributions from the gas bubbles, the solid/liquid 'matrix', and even the interface that divides the two phases. Perhaps one of the more simplistic factors determining the functionality of the final foam however, is the ratio of gas to liquid, wherein the contributions of these phases is determined.

2.3.1 Wet Foams and Dry foams

Liquid foam can be divided into two main categories of 'wet' and 'dry', which is based on the fraction of gas and liquid, ϕ_g and ϕ_l, respectively. Early in the foam lifetime, the majority of foams are 'wet', where the liquid fraction dominates[7]. Over time however, ϕ_l decreases as liquid leaves the foam, partially through evaporation, but primarily by draining under the force of gravity, resulting in a 'dry' foam[23]. In reality, these categories represent either end of a spectrum of foam states (see Figure 2.2), but are useful for broadly describing certain key characteristics.

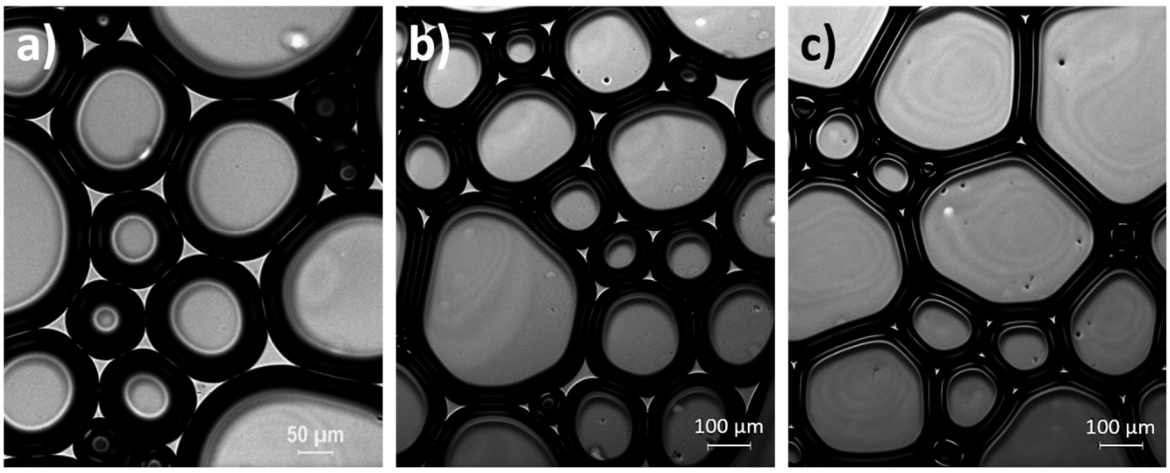

Figure 2.2. Micrographs of 'wet' and 'dry' foam structures: a) Higher liquid fraction ($\phi_l \approx 0.08$) with approximately spherical bubbles. b) Decreasing liquid fraction ($\phi_l \approx 0.06$) with distortion to spherical bubbles. c) Dry foam structure with low liquid fraction ($\phi_l \approx 0.03$) and polyhedral shapes appearing.

2.3.1.1 Wet Foams

A wet foam is generally defined as having a liquid fraction that is over 5% of the overall foam volume, but less than the so-called 'critical liquid fraction', ϕ_l^*, where bubbles are no longer in contact with one another, also known as the 'wet limit' (i.e. $0.05 \lesssim \phi_l < \phi_l^*$)[1]. The wet

limit is usually based on an estimated value for the optimised packing of hard spheres[23], which varies based on foam polydispersity[24]. For example the 'Bernal Packing Density of Hard Spheres' gives a critical liquid fraction of $\phi_l^* = 0.36$, however this decreases with increasing polydispersity, where packing becomes more efficient. It has been widely noted that these bubble size distributions play an important role in the foam's structural properties, such as yield stress and elastic properties, as well as appearance[9,12].

Above the wet limit, the interaction of bubbles with one another drops off dramatically, reducing the solid-like behaviour of the foam structure. A liquid containing a dispersion of a few spherical bubbles where the liquid spacing is of a similar order (or higher) to the gas bubble size, can be thought of as a 'gas emulsion'[25], where a more liquid-like behaviour is generally observed.

The wide range of foam applications are based in the wet foam regime, where the liquid formulation contains highly desirable functional attributes. To once again use food foams as a prime example, a chocolate mousse can generally contain a liquid fraction anywhere between 0.5 and 0.9 depending on the desired texture and perceived 'richness' of the product, which can categorise it as a wet foam or gas emulsion respectively. As with many foams in the food industry, too low a liquid fraction can produce an overly 'light' texture, which detracts from the desired creamy and luxurious mouthfeel[11].

2.3.1.2 Dry Foams

The dry foam regime is one where we expect the gas fraction to dominate over liquid by a substantial margin. This regime is usually entered towards the end of a foam's lifetime, where the majority of liquid has drained from the system. Ultimately, all liquid foams will evolve

towards a 'true' dry foam structure, where $\phi_l \to 0$, however a more general dry foam definition can be given as those having a liquid fraction that is less than 5% of the overall volume (i.e. $\phi_l \lesssim 0.05$)[1]. This category can apply to many everyday foams, including washing up foams, whose liquid fraction is generally less than 1% of the overall volume[26].

As can be seen in Figure 2.2c, bubbles within a dry foam tend to take on polyhedral shapes owing to the distortions caused by their close proximity to one another. A concise description of these fundamental structures is given by Cantat*, et al.*[1], namely:

'[The bubble's] faces are thin films that are gently curved either because of the pressure differences between the bubbles, or simply because its perimeter does not lie in one plane. The films intersect in threes along the edges …, which are liquid carrying channels known as Plateau borders ... The curvature of the liquid/gas interfaces must remain finite (by the Young-Laplace Law), which imposes a non-zero thickness on the Plateau borders ... The cross-section of each border is a small triangle with concave sides. Four Plateau borders intersect at the vertices (or nodes) of each polyhedral bubble.' (See Figure 2.3).

This description of a dry foam structure highlights some of the key physical laws that underpin the formation and stability of foam systems. It is these laws that transform the apparently random arrangement of gas cells in a liquid, into predictable geometric arrangements during the drying of foams.

2.3.2 Foam Stability: Minimisation of Surface Area

From a thermodynamic perspective, liquid foams are inherently unstable due their high surface area to volume ratios and the associated energy 'cost' of these interfaces (see below). Indeed, the lowest energy state of a foam is one where the foam does not exist at all, with a

single interface between the unaerated bulk liquid and the surrounding gas. Ultimately, this is the state that liquid foams evolve towards and the reason that increasing foam longevity is such a major topic of research[27].

The 'cost' of creating a gas-liquid interface is that of the surface free energy, which decreases with the surface area of the interface[28]. This can also be described in terms of the surface tension, where the intermolecular attractions along the liquid surface mean that a force is required to extend or distort it. As such, the minimum surface area is the least energy intensive[23]. This fundamental law is responsible for many of the phenomena seen in bubbles. It is the reason individual bubbles take on spherical geometries and similarly the reason for the distinctive polyhedral shapes that arise in dry foams.

While a sphere is an intuitive shape for minimising surface area, the range of polyhedral shapes observed in dry foams are perhaps less obvious. This was the subject of intensive study by Belgian physicist Joseph Plateau, who derived a series of laws to describe the bubble arrangements. Two of these laws are contained within Cantat's[1] description of the dry foam structure, wherein a dry foam can only be at equilibrium if:[23,29]

1) Films intersect three at a time and only at 120 degrees.

2) There are no more than four intersection lines at a stable vertex, with all angles at the Maraldi Angle (~109.5˚).

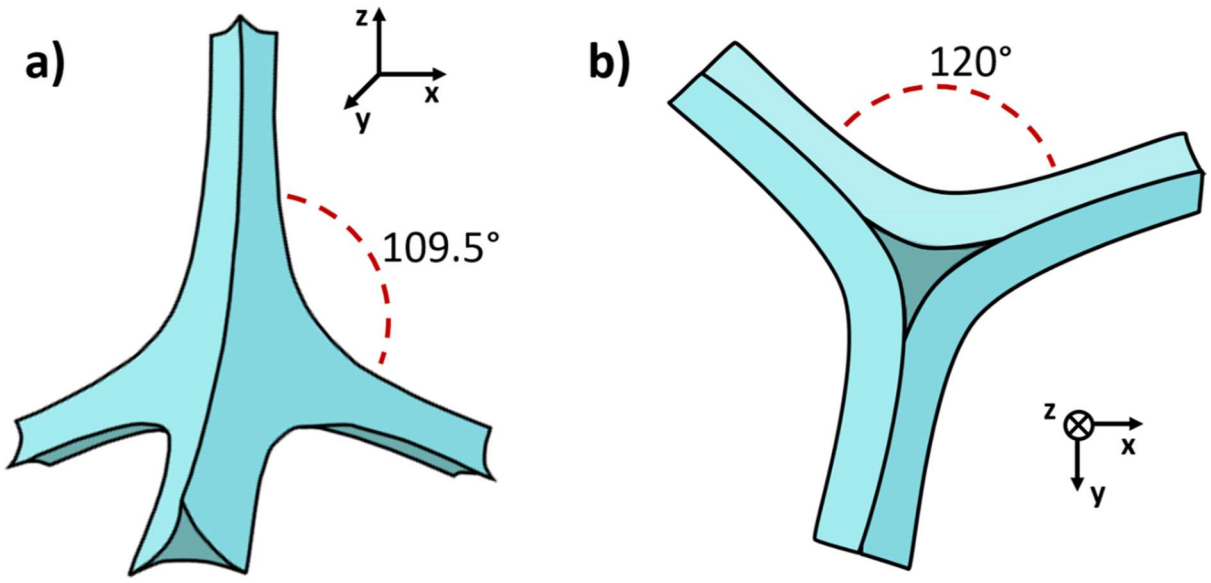

Figure 2.3. Example schematics of fundamental dry foam channel microstructures i.e. Plateau borders intersecting at a Node. a) Side view. b) Top down view.

Due to the strict, thermodynamically imposed, geometries present in dry foam structures, they have proven to be a highly useful feature for studying the fundamental dynamics of foam systems.

2.4 Stabilisation of the Gas-Liquid Interface

In order to maximise foam longevity, it is necessary to minimise the energy cost associated with forming and maintaining gas-liquid interfaces. This is a fundamental consideration of foam formulation where either chemical emulsifiers/surfactants or macroscopic particles can be used to disrupt the attractive intermolecular forces at the surface and thus reduce the surface tension. These can be highly effective when used individually, but can also be combined to either further improve or reduce their surface disruptive effects depending upon whether foams are desirable or not. During this study, we will take the assumption that longer

foam lifetimes are a desirable attribute, and will therefore not consider antifoaming agents and/or combinations.

2.4.1 Surfactants

Surfactants are a group of molecules that exhibit strong surface activity and high surface lateral diffusion, while being able to adsorb and desorb from the gas-liquid interface[30]. They are usually of a relatively low molecular weight and consist of a hydrophilic 'head' group and one or several hydrophobic 'tails'[31].

When surfactant molecules diffuse to the gas-liquid interface, they adsorb by arranging the hydrophobic region within the gas phase and the hydrophilic section in the liquid phase[32]. Being of a low molecular weight means that they generally highly mobile both in the bulk liquid and at the interface[33], therefore giving them the ability to rapidly coat newly created air–liquid interfaces during foaming[31]. Due to their size, low molecular weight surfactant molecules (LMWS) have a tendency to pack efficiently at the interface, making them effective at lowering surface tension[28] (See Figure 2.4); however, this can also be affected by factors such as molecular charge[34] and Hydrophilic Lipophilic Balance (HLB)[32].

Initially, monomeric LMWS adsorption leads to the formation of a surfactant monolayer at the interface, whose concentration increases with bulk concentration until the interface becomes saturated. The point at which this occurs is known as the *critical micelle concentration* (CMC) and denotes the point at which no additional surfactant is able to adsorb at the interface[35]. This is noted in various instances by the appearance of a constant surface tension despite increasing surfactant concentration[2,7,23]. The increase in bulk monomeric surfactant as one exceeds the CMC favours the formation of *micelles*, aggregations of 50-100 molecules[23]

where the hydrophobic regions are hidden in the centre. Therefore, above the CMC, LMWS exists as a monolayer at the interface and in both micellar and monomeric forms in the bulk, which can affect the adsorption dynamics of the system[36].

While the lowering of surface tension is obviously a key factor in their fundamental ability to create foams, it is the highly mobile nature of LMWS at the interface that helps to provide longer term foam stability, especially in the case of dry foams. Any localised deformations of bubble films results in an increase in the film surface area and a resulting decrease in the surfactant concentration at this region of the interface as well as an increase in surface tension. The resulting surface tension gradient that forms results in the fast diffusion of surfactant both across the surface and within the film, dragging liquid with it[23]. As a result of this 'Gibbs-Marangoni' mechanism, the film is able to resist localised thinning and hence reduce the probability of rupture[9,37].

Despite LMWS solutions generally exhibiting excellent foaming characteristics, there are also significant drawbacks to the dynamic interfaces they produce. Despite their dense coverage of the foam interfaces, the dynamic nature of this layer allows for short term exposure of gaps that can allow for diffusion of gas molecules through the membrane. As such, LMWS do not render foams completely impervious to gas transfer between bubbles, which is a major driving force for foam collapse[10,38]. Furthermore, the mobile nature of the bubble interfaces often makes them less robust than their higher molecular weight emulsifier or particle stabilised counterparts, leaving interfaces more prone to rupture due to the penetration of larger particles or application of shear forces[10].

2.4.2 Emulsifiers

While it can be said that all surfactants can be classed as emulsifiers, it is not the case that all emulsifiers can be classed as surfactants. As discussed above, the ability of surfactants to easily adsorb and desorb from the interface forms a key part of their definition, whereas this is not necessarily the case for all emulsifiers. More generally, emulsifiers are compounds which concentrate around the interface of two immiscible phases, reducing interfacial tension and also providing a barrier against coalescence of the discrete phase[39]. This barrier can be through electrostatic and/or steric repulsion between neighbouring droplet/bubble interfaces thus helping to form stable foams or emulsions[31,40]. This broader grouping includes molecules with high molecular weights and low mobility, which can adsorb slowly and practically irreversibly to the interface[41]. It should be noted however, that this description is not definitive, as has been highlighted by a class of near spherical polar molecules called 'hydrophobins', which blur the lines between emulsifiers and particles[42,43].

Proteins provide a very good example of a broad class of emulsifiers, with diverse properties and functionality. Proteins are highly complex polymers whose functional properties are related to their structural and other physicochemical properties[44,45]. A formal definition would yield their classification as macromolecules composed of a linear polypeptide backbone to which amino-acid side chains with various degrees of polarity and charge are attached[4]. The overall protein conformation is determined by the sequence of the amino acids (the primary structure) which ultimately results in further arrangements of the substructure (e.g. α-helices, β-sheets, random coils) and further connections and arrangements of these substructures[4].

For those not of a bio-chemistry persuasion, a more simplistic picture sees proteins as complex coiled and contorted chains, with some regions exhibiting hydrophobic properties and some hydrophilic. In aqueous solution therefore, a water-soluble protein will generally arrange into conformations that hide their hydrophobic regions from solution (e.g. whey proteins in dairy)[31,46]. However, upon encountering an air-water interface the protein will begin to unfold, projecting its hydrophobic groups above the liquid interface in order to minimise contact[9,46] (See Figure 2.4). The protein conformational changes that occur as a result of this adsorption are usually referred to as *surface denaturation*[40]. These tendencies have been variously noticed, in part as a result of the positive correlation between increased foamability and *average* protein hydrophobicity rather than just *surface* hydrophobicity[45]. It is therefore the properties of the unfolded protein rather than the native protein that dictate its behaviour at the air-water interface[45].

On a macroscopic scale, the main stabilisation mechanism of proteins adsorbed at the air/water interface (at least those not in a micellar arrangement, e.g. casein micelles[47]) is to subsequently form a strong viscoelastic network which significantly reduces the mobility of individual proteins[48]. These robust interfaces can impart a high degree of foam stability, not least because their elasticity renders them less prone to film rupture. While the viscoelastic layer that forms around the interface is not sufficient to dramatically alter the mean-free path of gas molecules passing through, and thus prevent gas transfer between bubbles[38,49], they can at least provide some resistance to bubble shrinkage. Citing the theoretical work of Meinders*, et al.*[50] and the experimental work of Dickinson*, et al.*[51], Murray*, et al.*[38] note that while only a purely elastic interface would be able to prevent bubble shrinkage outright, the partial elasticity of the protein film is at least enough slow the process. Furthermore, the

low mobility of protein molecules at the interface can slow the flow of liquid between bubbles, which can be highly efficient at promoting foam stability, as will be discussed in Section 2.4.

The functional properties of proteins at the air-water interface are highly dependent on the conditions within the aqueous phase. Lexis*, et al.*[52] note that the pH and ionic strengths of the protein solutions can have major impacts on their stabilisation properties. In the case of ionic strength for example, a reduction in the electrostatic repulsion between proteins can lead to their closer packing and thereby increase the probability of aggregation. This in turn can lead to an increased ability to 'plug' the nodes of Plateau borders, a further means by which proteins can help to promote stability by reducing the liquid flow from foams[52].

2.4.3 Particles

As will be discussed in the section on foam drainage, the ability to 'plug' nodes does not lie solely with aggregated proteins, but is a role that can be played by a wide range of particle systems[53-57]. Far from being just an additional suspension in the liquid foam matrix however, particles are increasingly being utilised for their own interfacial stabilising properties in foams[32,58].

Particle stabilised foams are those that are partially or entirely stabilised by small (often nano-scale), stable, surface active particles[38]. These foams are often significantly more stable than their standard emulsifier stabilised counterparts, remaining stable for days, weeks or even years in some cases[59]. Ultimately, particles of a sufficient size with suitable surface energy or contact angle are able to adsorb at interfaces in a way that is comparable to surfactants[28,32,38] (see Figure 2.4). The difference however, is that once adsorbed, this attachment energy can be several orders of magnitude higher than that of other emulsifiers. The huge amount of

energy (the maximum being at a contact angle of 90˚) required in order to remove the particle from the interface, renders its adsorption essentially irreversible[26,38].

The major outcomes of a particle coated bubble interface is that its ability to shrink is dramatically reduced; as this would require at least the partial desorption from the interface[38]. Instead, depending upon the relative size of particles to bubbles, the bubbles either tend towards a faceted or crumpled shape until a local energy minimum is reached[28]. Indeed, the tendency of the interface to fold or crumple was demonstrated experimentally early on by Aveyard, *et al.*[60] who demonstrated the folding of their particle layer under compression as opposed to the expulsion of particles. This mechanism has become commonly known as 'armouring'[26,28], with a 'jamming effect' used to describe the resistive friction between adsorbed particles that occurs as the interface attempts to shrink[61].

One slight drawback of an armoured interface however is that the requirement of a 90˚ contact angle with the aqueous phase demands particles which exhibit a high degree of hydrophobicity. As such, these ideal particles would also be likely to form aggregations within the liquid phase, paradoxically reducing their stabilising ability at the interface[38]. In fact, for particles that are too hydrophobic, it is likely that they will actively induce bubble coalescence by bridging and consequently rupturing bubble films.

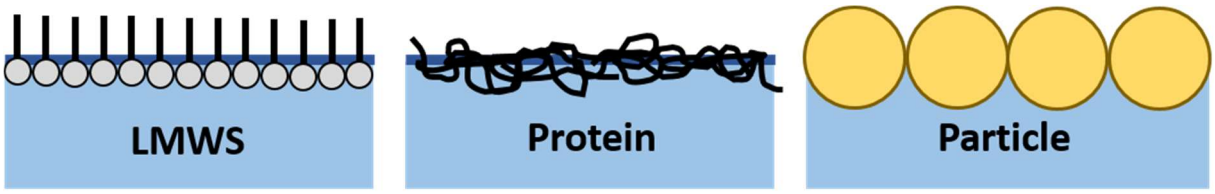

Figure 2.4. Example schematics of LMWS, protein and particle stabilised interfaces.

2.5 Destabilisation of Liquid Foams

When observing the structure of a freshly foamed solution for any length of time, the head on a beer for example, more often than not a gradual change of the bubble size distribution can be seen. Thermodynamically speaking, for a simple two-phase foam, there is more surface energy when the gas phase is highly subdivided than there is when it is coarsely subdivided[62]. As such, the gradual coarsening of the foam is to be expected with time as the foam strives towards thermodynamic equilibrium and ultimately collapse.

There are three primary mechanisms that ultimately determine foam lifetimes, bubble coalescence, disproportionation and the drainage of the liquid phase[63]. While these mechanisms are each of great significance this study we will focus on foam drainage as a major factor influencing foam lifetimes.

2.5.1 Disproportionation

Disproportionation refers to the gradual transfer of gas between bubbles due to pressure gradients between them[23]. These pressure gradients arise due to the surface tension of each bubble giving them their own internal pressure, which is inversely proportional to the radius of curvature of the bubble interface. This 'Laplace Pressure' means that smaller bubbles have a higher internal pressure than larger bubbles[1]. This can act as a driving force for diffusion of gas across the interface, the net result being the loss of gas from smaller bubbles and the uptake of gas by larger ones.

There are various methods that can be employed to reduce disproportionation, such as minimising the initial bubble size distribution to minimise pressure gradients[26], however it is

universally accepted that maintaining a high foam liquid fraction can significantly reduce the rate of gas diffusion between bubbles. As such, loss of the foam liquid fraction a major driving force for disproportionation.

2.5.2 Bubble Coalescence

A further process at work during bubble coarsening is that of coalescence, which occurs as a result of film rupture in the bulk foam[23]. The rupture of bubble interfaces can occur through various mechanisms, such as the bridging-dewetting of films by particles[26,64] or the localised thinning of films due to the presence of antifoaming agents[28]. Regardless of the mechanism involved however, the rupture and subsequent coalescence of bubbles leads to sudden and unpredictable changes to the foam structure. These 'topological changes' and can often be seen as rapid shifts in recorded data relating to the foam's structure and mechanical responses[23].

A decrease in foam liquid fraction will ultimately result in the thinning of the films that divide gas cells and increase the likelihood of their rupture[7]. As such, foam drainage can also be seen to be a major driving force for this type of foam instability.

2.5.3 Foam Drainage

Foam drainage describes the decrease of the foam liquid phase due to the passage of liquid through bubble films and the adjoining network of liquid channels, driven by the competition between gravitational and capillary forces[2]. The decrease in foam liquid fraction that results from drainage serves to increase the probability of bubble coalescence and can also increase the rate of gas transfer between bubbles, thus driving disproportionation. As such, halting or slowing foam drainage is often seen as a key way of prolonging foam lifetimes.

A popular method of reducing or halting foam drainage is to target the bulk rheology of the aqueous phase as this is a relatively simple approach that is highly effective. By increasing the liquid viscosity for example, liquid flow can be greatly reduced and dramatically increase foam lifetimes (Schramm, 2014). A simple addition of sugar to egg white albumen for example, transforms the whipped system from a fast draining dry foam, to a highly stable wet foam with desirable textural properties. In order to halt liquid drainage altogether, it is also possible to tailor bulk rheology such that the liquid yield stress, when combined with other flow resistive elements such as capillary and hydrodynamic forces, is greater than the stress imparted by gravity. By doing this it has been shown that the drainage can be effectively halted, albeit for a more limited range of formulations[7].

While the fairly standard technique of manipulating bulk liquid rheology can reduce drainage rates, this is not always a feasible technique when one considers the very broad range of applications for foams. A yield stress stabilised foam may be ideal for a meringue, but it may not be cost effective or practical in other circumstances e.g. froth flotation in the oil and gas industry. Furthermore, altering rheology may have other detrimental effects to the foam system. For example, increasing liquid viscosity may actually inhibit the initial formation of the foam due to a lower efficiency of incorporation of air, thus requiring longer aeration times or just making it impossible to attain desired foam overruns. For example, while pea proteins have recently become desirable for food foam applications, high viscosity solutions are required to improve long term stability, but negatively impact foamability[65]. In cases such as these therefore, compromise and innovation are required to achieve desirable results.

A different approach to retarding drainage can be through the physical blocking of foam channels through the use of an additional solid particle phase. Such three phase foams can occur naturally, as can be seen in the crema of a coffee where coffee solids can be seen to restrict flow through foam channels and their nodes. More recently however, investigations have been made into better understanding the phenomenon of node 'clogging' and ways in which this can be intentionally instigated through the inclusion of particles designed for this purpose[53,54]. While this has been shown to be a potentially effective means of slowing drainage rates, there are problems associated with the presence of macroscopic particles in the liquid phase. Primarily, there is the danger that sufficiently large particles can penetrate neighbouring gas-liquid interfaces, bridging bubbles and thus enhancing instability through bubble coalescence. This issue becomes increasingly prevalent if drainage is still able to proceed to some degree, where the decreasing liquid fraction increases the likelihood of particles bridging liquid films[2].

Perhaps the least explored mechanisms explored to deliberately target foam drainage are those that focus on the design of the gas-liquid interface and its effect on liquid flow. In reality however, this is unsurprising given that choices of appropriate particles/surfactants/emulsifiers are fundamental in determining the foamability and subsequent stability of the foam against disproportionation and coalescence[66]. Indeed, the impact of the interfacial properties on limiting gas transfer between bubbles and preventing coalescence have been well explored and tend to be more intuitive. As such, the design of foam interfaces and the effects on drainage are still largely seen as secondary, despite it being well-established that the relationship is significant[63,67].

A great deal of theoretical work and a far more limited body of experimental work has been conducted into the surface properties of liquid films and foam channels[2,63,68]. This work falls into two main categories: those analysing the problem from the perspective of macroscopic foam drainage; and those investigating from the perspective of individual liquid channels and films at the microscale[2,69]. The major benefit of macroscopic studies is that theoretical predictions are far easier to verify experimentally, with various experimental techniques commercially available to measure foam drainage. However, as such studies are based on simplifying the highly complex foam structures into idealised theoretical models, it is essential that the assumptions made by such models also receive scrutiny. As will be shown, macroscopic drainage models must take into account drainage through the foam microstructure, and it is therefore the job of microscale theory and measurements to inform these models and improve their reliability and applicability.

2.5.3.1 Macroscopic Drainage Models

The vast majority of experimental research into foam drainage is concerned with macroscopic systems, where a range of models have been developed in order to describe them. These models have evolved over time as our understanding has improved[63], going from simple two-phase Newtonian dry foams[69,70], to those that attempt to include non-Newtonian bulk and interfacial rheologies[71].

Macroscopic foam models are generally based on the premise that macroscopic foams can be treated in the same manner as flow through a porous medium. Indeed, it has been shown that, in many cases, Darcy's Law for low Reynold number liquid flow through a porous medium, gives a good description of foam drainage[68,72-76]. This being said, the complexity of

foam systems means that these models are generally based on the assumptions that foam channels have constant dimensions, as well as constant interfacial properties throughout the entire foam network. In reality, the foam channels can vary dramatically in size between the top and bottom of a draining foam network, directly affecting liquid flow rates and interfacial properties such as the surface shear viscosity in turn[2]. It is for these reasons that measurement of foam drainage rates in macroscopic foams can be quite variable and thus fit reasonably well to such approximated theoretical fits.

An additional approach applied by Stevenson[74] has been to model foam drainage using dimensional analysis. By replacing dimensional quantities with non-dimensional counterparts, it was shown that greatly simplified drainage models could be produced that ultimately related liquid drainage rates and liquid holdup in the foam via a simple power law. This was able to accurately predict the relationship of between drainage rate and bubble size, albeit in systems where inertial losses were neglected[74]. Two key parameters were required in order to develop Stevenson's technique into a mechanistic approach; however, the viscous losses in the PBs and the relative losses in the nodes.

Regardless of the approach taken, macroscopic foam drainage has been found to fall into one of two regimes that are defined by whether or not the viscous dissipation (and consequently hydrodynamic resistance) is dominant in the PBs (*Channel Dominated*), or the nodes (*Node Dominated*)[63,72]. In short, whether the majority of time liquid spends within a foam system is in the passage through the PBs, or through the nodes. Ultimately, it has been shown that this depends upon the surface viscosity of the air-liquid interface, where the resulting hydrodynamic resistances of each channel and node combine to produce an overall picture of

foam permeability. It is this proposed importance of viscous dissipation on macroscopic drainage that has led to a great deal of theoretical, and much more limited experimental, scrutiny on the surface rheological properties of the interface at the microscale.

2.5.3.2 Microscale Drainage Models

Unlike their macroscopic counterparts, microscale foam drainage models generally strive to make as few approximations as reasonably possible. This is largely due to the fact that, at the scale of individual foam channels and nodes, even the smallest inaccuracies can be significant. When one considers the substantial scaling required to translate microscale findings to macroscale systems, this makes sense. As a pertinent example, combining the hydrodynamic resistances calculated for isolated foam channels and nodes into foam comprised of hundreds of such units, errors could propagate into a substantially distorted picture of foam permeability[77,78]. Given the complexity of these systems however, it is virtually impossible to proceed without at least some assumptions being made.

While some models maintain the assumption that these channels are cylindrical[71], others have described them as triangular prisms[79] or incorporated the ideal PB geometries shown in Figure 2.3. This has either been done with[54,77,80-82] or without[79,83-88] accounting for the effects of the nodes[89]. What unites these models is that they attempt to describe the drainage of microscale systems at the level of PBs and nodes in terms of the balance between gravitational, capillary and viscous forces[63]. This means that without exception, there is an inclusion of surface viscosity, which has been used as a fitting parameter to macroscale[67,90] or microscale[77,85-89,91] drainage experiments, in an attempt to better understand transitions between channel and node dominated drainage regimes.

While microscale drainage theory continues to develop and evolve, its development has far exceeded that of complimentary experimental investigation. Indeed, dedicated experimental studies of foam channels and nodes at the microscale remain few and far between, a review of which was recently published by Anazadehsayed*, et al.*[89]. As will be discussed extensively throughout this thesis, this has largely been due to the difficulties in creating, controlling and observing such structures. This is a hugely important deficit in the current literature, as models and simulations of idealised cases must be compared to real systems. In the case of channel and node dominated drainage for example, separating the complex geometric transition between PB and node into a single perfectly uniform PB vs. a single perfect node may not be an accurate representation (See Figure 2.5).

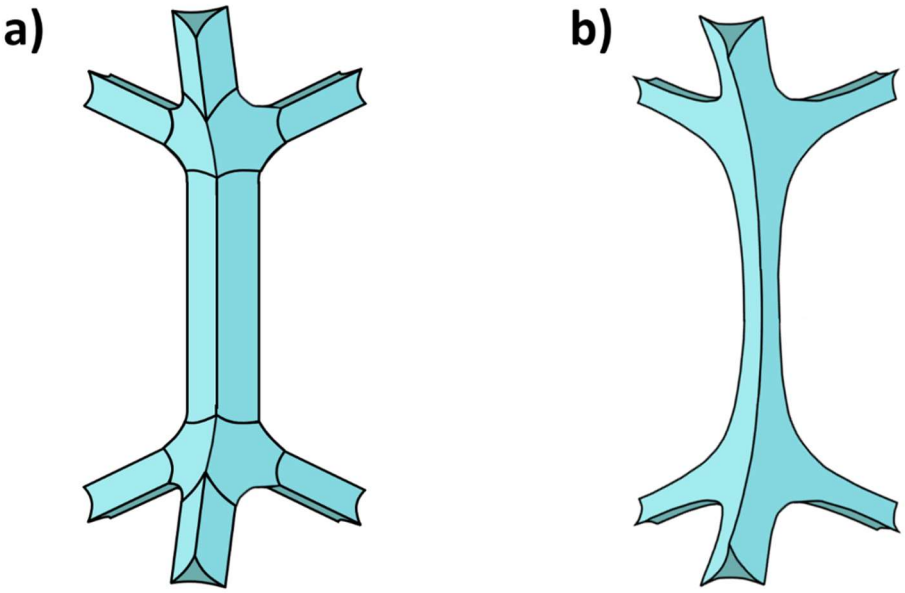

Figure 2.5. Schematics of conjoined nodes and Plateau borders from: a) an idealised theoretical description; b) a real foam system.

It is important to note that the majority of microscale drainage models only apply to foam systems below the wet limit, after which the dissipative network of PBs and nodes is no longer

a valid representation of the system. It can be said that at this point, these structures no longer exist, instead being replaced by elastic bubbles in close contact with one another[63]. As such, there are still many questions that remain in the theoretical domain of microscale foam drainage modelling, and certainly from the experimental perspective.

2.6 Conclusions

In general, aqueous foams are an incredibly broad and versatile form of soft matter, with a myriad of applications. They can be produced with a wide range of chemical and physical stabilisers introduced at the stage of formulation and targeted to bring different functional attributes. The decisions made at the stage of formulation ultimately determine the mechanisms by which foams are produced and stabilised against the onset of drainage, disproportionation, coalescence and ultimately, collapse.

Of the key mechanisms of foam destabilisation, retarding liquid drainage has proven to be a particularly effective tool for extending foam lifetime and functionality. While tailoring liquid bulk rheology and including particle structures feature heavily in the literature, the other key drainage factor of viscous dissipation at the bubble interface remains a largely secondary consideration.

Understanding the role of the gas-liquid interface in foam drainage remains an ongoing investigation. Theory and experiment have been able to clearly demonstrate that the surface viscosity of the interface plays a significant role in macroscopic foam drainage, placing it in regimes of either node-dominated or channel-dominated drainage. At the microscale however, the picture becomes far more complex, where the precise influences of foam

channel geometries, and corresponding variations in surface tension and surface viscoelasticity can all come in to play. Furthermore, a significant deficit in experimental work at the microscale has been identified in the existing literature.

Overall, it is the opinion of this author that the geometry and interfacial rheology of foam channel interfaces during liquid flow requires additional experimental analysis in order to confirm theoretical predictions. It is only by doing this that current drainage theory can be fully integrated into real foam systems across length scales.

2.7 References

1 I. Cantat; S. Cohen-Addad; F. Elias; F. Graner; R. Höhler; O. Pitois; F. Rouyer; A. Saint-Jalmes; S. Cox, *Foams: Structure and Dynamics*; Oxford University Press: New York, **2013**.

2 J. Wang; A. V. Nguyen; S. Farrokhpay, A Critical Review of the Growth, Drainage and Collapse of Foams, *Advances in Colloid and Interface Science* **2016**, *228*, 55-70.

3 S. Berkman; G. Egloff, Gas-in-Liquid Dispersions. In *Perry's Chemical Engineers' Handbook*, 7 ed.; Perry, R.; Green, D.; Maloney, J., Eds. McGraw-Hill: **1997**; p 1409.

4 A. K. H. Heuer. Formulation and Stability of Model Food Foam Microstructures. University of Birmingham, Birmingham, 2009.

5 R. Hansen, Handbook of Polymeric Foams and Foam Technology, Daniel Klempner and Kurt C. Frisch, Eds., Hanser Publishers, Munich, Germany, 1992, 442 Pp. Price: $148.00.

(Distributed in the U.S. And Canada by Oxford University Press, New York.), *Journal of Polymer Science Part A: Polymer Chemistry* **1993**, *31*, 1344-1344.

6 G. M. Campbell; M. G. Scanlon, *Bubbles in Food 2 : Novelty, Health and Luxury*; Egan Press: St. Paul, Minn., **2008**.

7 R. J. Pugh, *Bubble and Foam Chemistry*; Cambridge University Press: Cambridge, United Kingdom, **2016**.

8 L. Cook; J. Stephenson; S. D. Bateman, Foam Dressings: A Review of the Literature and Evaluation of Fluid-Handling Capacity of Four Leading Foam Dressings, *Wounds UK* **2015**, *11*, 75-81.

9 G. M. Campbell; E. Mougeot, Creation and Characterisation of Aerated Food Products, *Trends in Food Science & Technology* **1999**, *10*, 283-296.

10 B. S. Murray, Stabilization of Bubbles and Foams, *Current Opinion in Colloid & Interface Science* **2007**, *12*, 232-241.

11 A. Lazidis; L. Parizotto; F. Spyropoulos; I. Norton, *Microstructural Design of Aerated Food Systems by Soft-Solid Materials*, **2017**; Vol. 73, p 110-119.

12 J. C. Germain; J. M. Aguilera, Structural Image Analysis of Food Foams and Aerated Food Products. In *Bubbles in Food 2: Novelty, Health and Luxury*, Campbell, G. M.; Scanlon, M. G.; Pyle, D. L., Eds. Elsevier: **2016**; pp 109-116.

13 J. Chandrashekar; D. Yarmolinsky; L. von Buchholtz; Y. Oka; W. Sly; N. J. Ryba; C. S. Zuker, The Taste of Carbonation, *Science (New York, N.Y.)* **2009**, *326*, 443-5.

14 A. Vilela; F. Cosme; T. Pinto, Emulsions, Foams, and Suspensions: The Microscience of the Beverage Industry, *Nutrafoods* **2018**, *4*.

15 G. M. Campbell, Chapter 1 - a History of Aerated Foods. In *Bubbles in Food 2*, Campbell, G. M.; Scanlon, M. G.; Pyle, D. L., Eds. AACC International Press: **2008**; pp 1-21.

16 A. Mondal; K. Niranjan, Chapter 4 the Role of Bubbles in the Development of Food Structure. In *Handbook of Food Structure Development*, The Royal Society of Chemistry: **2020**; pp 93-114.

17 C. Raboutet; C. Fernandez; B. LeBlanc; G. D. Valle; A. Ndiaye, Chapter 36 - a Knowledge Base on Cereal Food Foams Processing and Behaviour. In *Bubbles in Food 2*, Campbell, G. M.; Scanlon, M. G.; Pyle, D. L., Eds. AACC International Press: **2008**; pp 381-388.

18 B. M. Adhikari; T. Truong; N. Bansal; B. Bhandari, Use of Gases in Dairy Manufacturing: A Review, *Critical Reviews in Food Science and Nutrition* **2018**, *58*, 2557-2569.

19 R. Hartel; J. Elbe; R. Hofberger, Aerated Confections. **2018**; pp 301-327.

20 G. W. A. Angus *Top 10 Global Consumer Trends 2019*; Euromonitor International: 2019; pp 18-24.

21 N. V. Nepovinnykh; O. N. Klyukina; Y. A. Kodatskiy; N. M. Ptichkina; S. Yeganehzad, Study of the Stability of Foam and Viscoelastic Properties of Marshmallow without Gelatin, *Foods and Raw materials* **2018**, *6*, 90-98.

22 T. Lafarga; C. Álvarez; S. Villaró; G. Bobo; I. Aguiló-Aguayo, Potential of Pulse-Derived Proteins for Developing Novel Vegan Edible Foams and Emulsions, *International Journal of Food Science & Technology* **2020**, *55*, 475-481.

23 D. Weaire; S. Hutzler, *The Physics of Foams*; Oxford University Press: New York, **1999**.

24 M. Lexis; N. Willenbacher, Yield Stress and Elasticity of Aqueous Foams from Protein and Surfactant Solutions – the Role of Continuous Phase Viscosity and Interfacial Properties, *Colloids and Surfaces A: Physicochemical and Engineering Aspects* **2014**, *459*, 177-185.

25 D. Exerowa; P. M. Kruglyakov, *Foam and Foam Films: Theory, Experiment, Application*; Elsevier Science B. V.: Amsterdam, **1998**.

26 M. Vignes-Adler; D. Weaire, New Foams: Fresh Challenges and Opportunities, *Current Opinion in Colloid & Interface Science* **2008**, *13*, 141-149.

27 D. Langevin, Surface Energy and Surface Rheology Relation to Foam Properties. In *Foams and Emulsions*, Sadoc, J. F.; Rivier, N., Eds. Springer Netherlands: Dordrecht, **1999**; pp 1-20.

28 E. Dickinson, Food Emulsions and Foams: Stabilization by Particles, *Current Opinion in Colloid & Interface Science* **2010**, *15*, 40-49.

29 J. A. F. Plateau, *Statique Expérimentale Et Théorique Des Liquides Soumis Aux Seules Forces Moléculaires*; Gauthier-Villars: Paris, **1873**.

30 Y. He; P. Yazhgur; A. Salonen; D. Langevin, Adsorption-Desorption Kinetics of Surfactants at Liquid Surfaces, *Advances in Colloid and Interface Science* **2014**, *222*.

31 L. A. Pugnaloni; E. Dickinson; R. Ettelaie; A. R. Mackie; P. J. Wilde, Competitive Adsorption of Proteins and Low-Molecular-Weight Surfactants: Computer Simulation and Microscopic Imaging, *Advances in Colloid and Interface Science* **2004**, *107*, 27-49.

32 B. P. Binks, Particles as Surfactants - Similarities and Differences, *Current Opinion in Colloid and Interface Science* **2002**, *7*, 21-41.

33 Z. A. Zell; A. Nowbahar; V. Mansard; L. G. Leal; S. S. Deshmukh; J. M. Mecca; C. J. Tucker; T. M. Squires, Surface Shear Inviscidity of Soluble Surfactants, *Proceedings of the National Academy of Sciences* **2014**, *111*, 3677-3682.

34 H. Vatanparast; F. Shahabi; A. Bahramian; A. Javadi; R. Miller, The Role of Electrostatic Repulsion on Increasing Surface Activity of Anionic Surfactants in the Presence of Hydrophilic Silica Nanoparticles, *Scientific Reports* **2018**, *8*, 7251.

35 A. Patist; S. S. Bhagwat; K. W. Penfield; P. Aikens; D. O. Shah, On the Measurement of Critical Micelle Concentrations of Pure and Technical-Grade Nonionic Surfactants, *Journal of Surfactants and Detergents* **2000**, *3*, 53-58.

36 T. M. Ferreira; D. Bernin; D. Topgaard, Chapter Three - Nmr Studies of Nonionic Surfactants. In *Annual Reports on Nmr Spectroscopy*, Webb, G. A., Ed. Academic Press: **2013**; Vol. 79, pp 73-127.

37 L. E. Scriven; C. V. Sternling, The Marangoni Effects, *Nature* **1960**, *187*, 186-188.

38 B. S. Murray; R. Ettelaie, Foam Stability: Proteins and Nanoparticles, *Current Opinion in Colloid & Interface Science* **2004**, *9*, 314-320.

39 M. De Villiers, Surfactants and Emulsifying Agents. **2009**; pp 251-256.

40 D. J. McClements, Protein-Stabilized Emulsions, *Current Opinion in Colloid & Interface Science* **2004**, *9*, 305-313.

41 G. Narsimhan, Role of Food Emulsifiers, Proteins, and Polysaccharides in Stabilization. In *Aerated Foods*, John Wiley & Sons: **2019**; pp 3-110.

42 A. R. Cox; F. Cagnol; A. B. Russell; M. J. Izzard, Surface Properties of Class Ii Hydrophobins from Trichoderma Reesei and Influence on Bubble Stability, *Langmuir* **2007**, *23*, 7995-8002.

43 A. J. Green; K. A. Littlejohn; P. Hooley; P. W. Cox, Formation and Stability of Food Foams and Aerated Emulsions: Hydrophobins as Novel Functional Ingredients, *Current Opinion in Colloid & Interface Science* **2013**, *18*, 292-301.

44 S. Damodaran; P. Paraf, *Food Proteins and Their Applications*. Marcel Dekker, Inc.: New York, **1997**.

45 S. Damodaran, Protein Stabilization of Emulsions and Foams, *Journal of Food Science* **2005**, *70*, R54-R66.

46 T. M. Herrington; S. S. Sahi, Desorption of Bovine Serum Albumen from the Air Water Interface. In *Food Emulsions and Foams*, Dickinson, E., Ed. Elsevier Science and Technology: **1987**.

47 A. H. Martin; H. Douglas Goff; A. Smith; D. G. Dalgleish, Immobilization of Casein Micelles for Probing Their Structure and Interactions with Polysaccharides Using Scanning Electron Microscopy (Sem), *Food Hydrocolloids* **2006**, *20*, 817-824.

48 A. R. Mackie; A. P. Gunning; P. J. Wilde; V. J. Morris, Orogenic Displacement of Protein from the Oil/Water Interface, *Langmuir* **2000**, *16*, 2242-2247.

49 B. S. Murray; E. Dickinson; Z. Du; R. Ettelaie; T. Kostakis; J. Vallet, Foams and Emulsions. Disproportionation Kinetics of Air Bubbles Stabilized by Food Proteins and Nanoparticles. In *Food Colloids: Interactions, Microstructure and Processing*, Dickinson, E., Ed. The Royal Society of Chemistry: **2005**; pp 257-272.

50 M. B. J. Meinders; W. Kloek; T. van Vliet, Effect of Surface Elasticity on Ostwald Ripening in Emulsions, *Langmuir* **2001**, *17*, 3923-3929.

51 E. Dickinson; R. Ettelaie; B. S. Murray; Z. Du, Kinetics of Disproportionation of Air Bubbles beneath a Planar Air–Water Interface Stabilized by Food Proteins, *Journal of Colloid and Interface Science* **2002**, *252*, 202-213.

52 M. Lexis; N. Willenbacher, Relating Foam and Interfacial Rheological Properties of [Small Beta]-Lactoglobulin Solutions, *Soft Matter* **2014**, *10*, 9626-9636.

53 A. L. Ellis; A. B. Norton; T. B. Mills; I. T. Norton, Stabilisation of Foams by Agar Gel Particles, *Food Hydrocolloids* **2017**, *73*, 222-228.

54 F. Rouyer; B. Haffner; N. Louvet; Y. Khidas; O. Pitois, Foam Clogging, *Soft Matter* **2014**, *10*, 6990-6998.

55 A. Lazidis; R. D. Hancocks; F. Spyropoulos; M. Kreuß; R. Berrocal; I. T. Norton, Whey Protein Fluid Gels for the Stabilisation of Foams, *Food Hydrocolloids* **2016**, *53*, 209-217.

56 P. Yazhgur. Flows in Foams : The Role of Particles, Interfaces and Slowing Down in Microgravity. Université Paris-Saclay, 2015.

57 B. P. Binks; T. S. Horozov, Aqueous Foams Stabilized Solely by Silica Nanoparticles, *Angewandte Chemie International Edition* **2005**, *44*, 3722-3725.

58 S. Lam; K. P. Velikov; O. D. Velev, Pickering Stabilization of Foams and Emulsions with Particles of Biological Origin, *Current Opinion in Colloid & Interface Science* **2014**, *19*, 490-500.

59 A. R. Cox; D. L. Aldred; A. B. Russell, Exceptional Stability of Food Foams Using Class Ii Hydrophobin Hfbii, *Food Hydrocolloids* **2009**, *23*, 366-376.

60 R. Aveyard; J. H. Clint; D. Nees; V. N. Paunov, Compression and Structure of Monolayers of Charged Latex Particles at Air/Water and Octane/Water Interfaces, *Langmuir* **2000**, *16*, 1969-1979.

61 A. B. Subramaniam; C. Mejean; M. Abkarian; H. A. Stone, Microstructure, Morphology, and Lifetime of Armored Bubbles Exposed to Surfactants, *Langmuir* **2006**, *22*, 5986-5990.

62 L. L. Schramm, *Emulsions, Foams, Suspensions, and Aerosols : Microscience and Applications (2)*; Wiley-VCH: Somerset, DE, **2014**.

63 P. M. Kruglyakov; S. I. Karakashev; A. V. Nguyen; N. G. Vilkova, Foam Drainage, *Current Opinion in Colloid & Interface Science* **2008**, *13*, 163-170.

64 R. J. Pugh, Experimental Techniques for Studying the Structure of Foams and Froths, *Advances in Colloid and Interface Science* **2005**, *114–115*, 239-251.

65 P. Moll; L. Grossmann; I. Kutzli; J. Weiss, Influence of Energy Density and Viscosity on Foam Stability – a Study with Pea Protein (Pisum Sativum L.), *Journal of Dispersion Science and Technology* **2019**, 1-8.

66 A. Saint-Jalmes; M. L. Peugeot; H. Ferraz; D. Langevin, Differences between Protein and Surfactant Foams: Microscopic Properties, Stability and Coarsening, *Colloids and Surfaces A: Physicochemical and Engineering Aspects* **2005**, *263*, 219-225.

67 M. Safouane; A. Saint-Jalmes; V. Bergeron; D. Langevin, Viscosity Effects in Foam Drainage:Newtonian and Non-Newtonian Foaming Fluids, *The European Physical Journal E* **2006**, *19*, 195-202.

68 A. Saint-Jalmes, Physical Chemistry in Foam Drainage and Coarsening, *Soft Matter* **2006**, *2*, 836-849.

69 S. A. Koehler; S. Hilgenfeldt; H. A. Stone, Foam Drainage on the Microscale: I. modeling Flow through Single Plateau Borders, *Journal of Colloid and Interface Science* **2004a**, *276*, 420-438.

70 G. Verbist; D. Weaire; A. M. Kraynik, The Foam Drainage Equation, *Journal of Physics: Condensed Matter* **1996**, *8*, 3715.

71 Z. Wang; G. Narsimhan, Model for Plateau Border Drainage of Power-Law Fluid with Mobile Interface and Its Application to Foam Drainage, *Journal of Colloid and Interface Science* **2006**, *300*, 327-337.

72 S. A. Koehler; S. Hilgenfeldt; H. A. Stone, A Generalized View of Foam Drainage: Experiment and Theory, *Langmuir* **2000**, *16*, 6327-6341.

73 E. Lorenceau; N. Louvet; F. Rouyer; O. Pitois, Permeability of Aqueous Foams, *The European Physical Journal E* **2009**, *28*, 293-304.

74 P. Stevenson, Dimensional Analysis of Foam Drainage, *Chemical Engineering Science* **2006**, *61*, 4503-4510.

75 A. Saint-Jalmes; Y. Zhang; D. Langevin, Quantitative Description of Foam Drainage: Transitions with Surface Mobility, *Eur. Phys. J. E* **2004**, *15*, 53-60.

76 F. Rouyer; O. Pitois; E. Lorenceau; N. Louvet, Permeability of a Bubble Assembly: From the Very Dry to the Wet Limit, *Physics of Fluids* **2010**, *22*, 043302.

77 O. Pitois; N. Louvet; E. Lorenceau; F. Rouyer, Node Contribution to the Permeability of Liquid Foams, *Journal of Colloid and Interface Science* **2008**, *322*, 675-677.

78 A. Saint-Jalmes; D. Langevin, Time Evolution of Aqueous Foams: Drainage and Coarsening, *Journal of Physics: Condensed Matter* **2002**, *14*, 9397-9412.

79 D. Desai; R. Kumar, Liquid Holdup in Semi-Batch Cellular Foams, *Chemical Engineering Science* **1983**, *38*, 1525-1534.

80 P. Stevenson; X. Li, A Viscous and Inertial Model of Foam Drainage, *Chemical Engineering Research and Design 88*, 928-935.

81 S. J. Neethling; H. T. Lee; J. J. Cilliers, A Foam Drainage Equation Generalized for All Liquid Contents, *Journal of Physics: Condensed Matter* **2002**, *14*, 331.

82 A. Anazadehsayed; N. Rezaee; J. Naser, Numerical Modelling of Flow through Foam's Node, *Journal of Colloid and Interface Science* **2017**, *504*, 485-491.

83 R. A. Leonard; R. Lemlich, A Study of Interstitial Liquid Flow in Foam. Part I. Theoretical Model and Application to Foam Fractionation, *AIChE Journal* **1965**, *11*, 18-25.

84 R. A. Leonard; R. Lemlich, A Study of Interstitial Liquid Flow in Foam. Part Ii. Experimental Verification and Observations, *AIChE Journal* **1965**, *11*, 25-29.

85 O. Pitois; C. Fritz; M. Vignes-Adler, Liquid Drainage through Aqueous Foam: Study of the Flow on the Bubble Scale, *Journal of Colloid and Interface Science* **2005a**, *282*, 458-465.

86 O. Pitois; C. Fritz; M. Vignes-Adler, Hydrodynamic Resistance of a Single Foam Channel, *Colloids and Surfaces A: Physicochemical and Engineering Aspects* **2005b**, *261*, 109-114.

87 F. Elias; E. Janiaud; J.-C. Bacri; B. Andreotti, Elasticity of a Soap Film Junction, *Physics of Fluids* **2014**, *26*, 037101.

88 K. Koczó; G. Rácz, Flow in a Plateau Border, *Colloids and Surfaces* **1987**, *22*, 95-96.

89 A. Anazadehsayed; N. Rezaee; J. Naser; A. V. Nguyen, A Review of Aqueous Foam in Microscale, *Advances in Colloid and Interface Science* **2018**, *256*, 203-229.

90 A. Cervantes-Martínez; A. Saint-Jalmes; A. Maldonado; D. Langevin, Effect of Cosurfactant on the Free-Drainage Regime of Aqueous Foams, *Journal of Colloid and Interface Science* **2005**, *292*, 544-547.

91 S. A. Koehler; S. Hilgenfeldt; E. R. Weeks; H. A. Stone, Foam Drainage on the Microscale Ii. Imaging Flow through Single Plateau Borders, *Journal of Colloid and Interface Science* **2004b**, *276*, 439-449.

Chapter 3

A novel experimental setup for the measurement of isolated foam channel geometries at controlled liquid flow rates.

.

3.0 Abstract

This chapter focuses on the development of a novel experimental setup to enact high-precision measurements of an isolated Plateau Border and Node foam geometry at controlled and varied liquid flow rates. Preliminary measurements on a PB formed in the presence of Sodium Dodecyl Sulfate (SDS) solution were used to assess the functionality, flexibility and practicality of the setup, which will form the basis for subsequent investigations throughout this thesis.

3.1 Framework

As discussed in Chapter 2, the phenomenon of foam drainage is a complex multi-scale process. Macroscopic foam drainage is ultimately dependent on the microscale liquid flow between bubbles, which in turn, is heavily influenced by molecular level interactions both in the liquid bulk and at the gas-liquid interface[1]. It is only by uniting our physical understanding of these different regimes that a full understanding of foam systems can be achieved[2].

The aim of this PhD thesis was to further the current physical understanding of 2-phase foam systems, using a well-defined, isolated foam channel geometry. This required accurate control over key variables, such as channel lengths, liquid flow rates and surfactant formulations. The appeal of these isolated systems is that they are spatially well defined, as well as being easy to manipulate and study, unlike macroscopic foam systems[3]. Here a purpose built experimental setup is proposed for the study and characterisation of spatially ideal, isolated PB-Node geometries at controlled liquid flow rates. The precision measurement of these geometries is key to enabling the successful application of theory to describe liquid flow

through such systems. The microscale studies of Pitois*, et al.*[4],[5,6] for example, were designed to try and apply theory describing the hydrodynamic resistance of ideal single foam channels and nodes[7] to real experimental systems.

3.1.1 Setup Requirements

The key requirements for an isolated PB-Node geometric analysis technique were as follows:

- *The technique should be practical to implement and adapt.*

A fundamental aspect of any measurement technique is that it should be reproducible, enabling the replication and comparison of experimental data. Attempts to reproduce existing measurement systems[6,8] have proven to be highly challenging, with the lack of available detailed data and required manufacturing capabilities confounding such efforts. It has therefore become apparent that a well-characterised experimental setup, using universally available components and manufacturing techniques, is necessary.

Furthermore, the use of off the shelf components and simplified manufacture improves the scope for setup adaptation. Even when simplified to an idealised microscale structure, fluid flow through PBs and nodes can be monitored and influenced in a variety of ways. For example, Elias*, et al.*[9] applied deliberate distortions to foam channels to monitor their elastic response, while Rouyer*, et al.*[8] injected particles into the channels to monitor their behaviour at the node. The measurement of these systems can be undertaken in a number of ways, be it via pressure measurements[4-6], particle tracking[10], simple geometric analysis[9], or various other methods. As such, flexibility and versatility in the fundamental design of the setup could prove highly valuable for improving the comparability of future studies.

- *The technique should be applicable to a variety of surfactant/emulsifier formulations.*

Owing to the wide variety of foamable surfactant/emulsifier formulations available to industry, designing a flexible technique to accommodate such differences could maximise its potential as a diagnostic tool. It should be stressed however, that the ability of formulations to form stable films (at least for the required duration of the experimental study) will always be a limiting factor in the production of these setups. To this end, there is likely to be greater uptake of this technique for the study of low molecular weight surfactant systems with fast film forming capabilities, rather than, for example, the more limited variety of high molecular weight polymeric emulsifiers with this property.

- *The technique should be able to directly or indirectly measure interactions between bulk liquid and channel interfaces during drainage.*

The ultimate goal of this study is to identify and quantify microscale interactions between channel interfaces and bulk liquid. This is a key aspect in determining a 'bottom-up' approach to foam formulation, wherein foam structure and lifetime can be efficiently tailored to suit foam applications. Measurement of such properties will require knowledge of a wide range of parameters, which includes, but is not limited to:

Surface Parameters – e.g. Surface Tension, Surface Viscosity, Surface Elasticity…

Bulk Parameters – e.g. Dynamic Viscosity, Liquid Density, Flow Velocity…

Molecular Surfactant/Emulsifier Parameters – e.g. Charge, Maximum Surface Concentration, Critical Micelle Concentration…

As such, the proposed technique should be able to account for and compare variables from each of these subsets. As will be demonstrated in later chapters, the accurate measurement of PB geometries at controlled liquid flow rates will form the basis for applied theory that achieves this requirement.

3.2 Development of the PB-Node Setup

3.2.1 Producing Isolated Foam Geometries

The production of isolated foam geometries dates back to Belgian physicist Joseph Plateau, who submerged and withdrew various wire frame geometries from surfactant solutions. The films produced in the wire frames self-assembled into their most thermodynamically stable arrangements according to Plateau's Laws[11]. A tetrahedral frame for example, produces four PBs meeting in a single ideal node, while a triangular prism produces two nodes that share a common PB down the central axis (Figure 3.1).

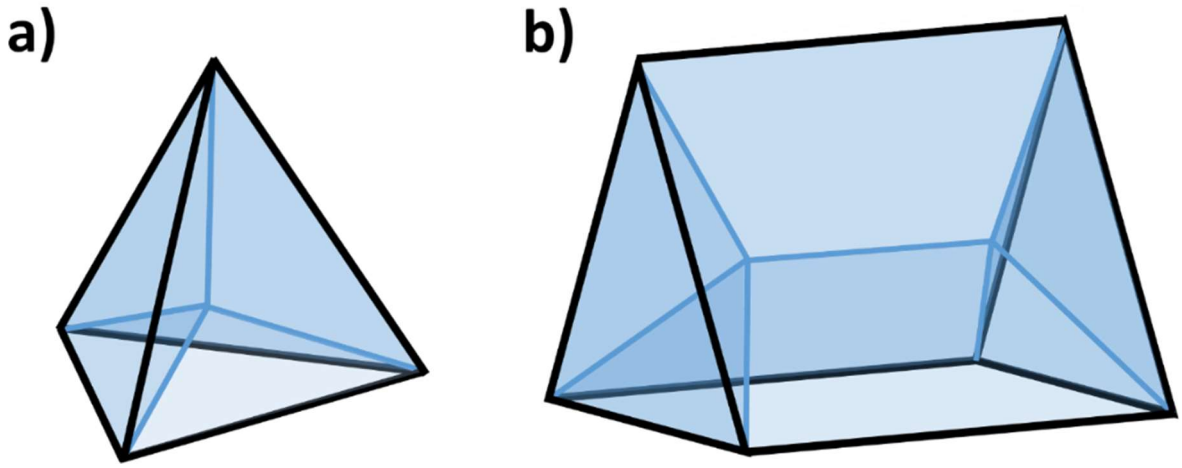

Figure 3.1. Examples of frame geometries producing an ideal PB/Node systems when withdrawn from surfactant solution. a) Single node tetrahedral frame, b) Dual node triangular prism frame.

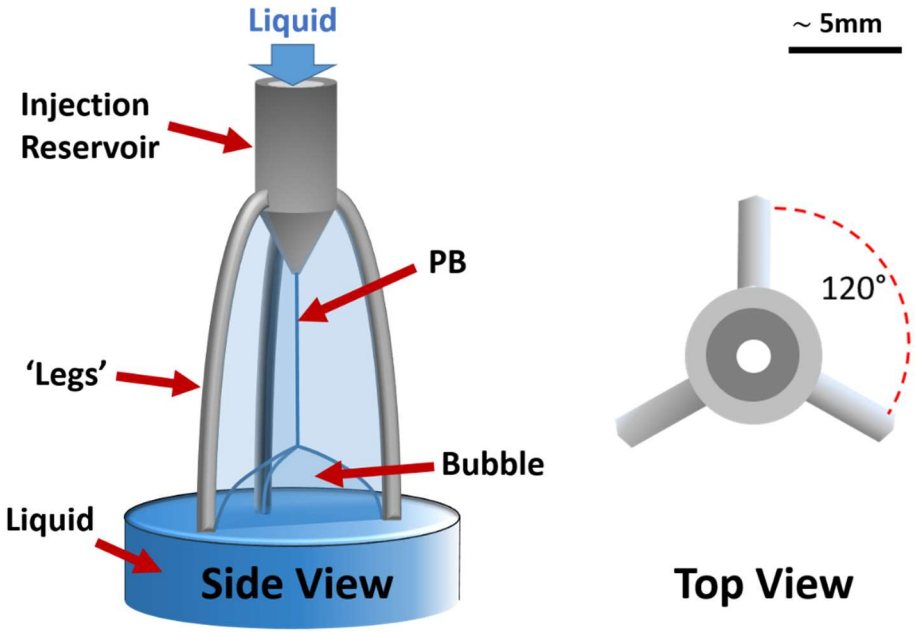

Figure 3.2. Illustration of the Plateau Border Apparatus[4] frame from the side (left) and the top (right). Three cylindrical 'legs' come off the central body at 120˚ to one another, producing an ideal PB when submerged and partially withdrawn from surfactant solution. The PB attaches to the central liquid injection reservoir, allowing flow rates through the PB to be controlled via a syringe pump.

An example of the triangular prism frame geometry can be seen in the study of Elias, *et al.*[9]. In this case, the added instability of the second node coupled with the difficulty of liquid injection, made it impractical for the study of low flow rates. Of the few existing studies however, most set ups are closer to the tetrahedral frame geometry, albeit without a base[4-6,8,12]. The 'Plateau Border Apparatus' of Pitois, *et al.*[4] for example, comprised of a metal tripod frame that could be submerged and partially withdrawn from surfactant solution, to produce a central vertical PB terminating in the bulk liquid instead of a node. This was later adapted, by injecting a single bubble at the base of the tripod such that a node would form[6,13] (see Figure 3.2). However, this had implications both for the geometry of the node produced

and for the practicality of producing it. Despite this, a major benefit of the tripod geometry was that the central PB would naturally attach itself to a central liquid injection nozzle, thereby allowing excellent control over liquid flow rates.

3.2.2 Frame & Injection System Design and Manufacture

In order to meet the design targets of the setup, it was necessary to adapt features of previous frame designs. From trials it was deduced that the most accurate and versatile way to produce consistent PB-Node geometries with direct PB liquid injection was via a closed single-node frame (e.g. tetrahedral).

In order to create precision frame geometries without the need for extensive machining capabilities, frames were designed using Tinkercad software (Autodesk inc., USA) and 3D printed using stereolithography on a FormLabs Form®2 printer. Stereolithography was chosen over conventional extrusion-based 3D printing techniques due to the higher resolutions achievable (up to 0.25mm).

The tripod frame of Pitois*, et al.*[4] was redesigned to include a base that would produce an ideal node when the frame was withdrawn from surfactant solution. Initially the base was designed to be adjustable to enable controlled variations of the upper PB length (see Figure 3.3a); however, this was later replaced with a fixed base in order to ensure measurement consistency. As frames could easily be adjusted in CAD software and reprinted, this was found to be a more effective and accurate method to alter PB-node geometries. Initially, a simple flat base design was implemented (Figure 3.3b); however, pooling of the draining solution on the surface and additional film formation due to the base thickness, necessitated adaptations to be made. Subsequently, the base surfaces were minimised and bevelled to prevent liquid

pooling, and made to converge into a single inner edge to prevent multiple film formation (Figure 3.3c).

The tripod legs were redesigned to triangular rather than circular cross-sections in order to minimise any fluctuation in the position of attached films. After trialling a variety of different leg separations, the distance between the inner edge of each neighbouring tripod leg was set as y=11.1mm (See Figure 3.3c). The aim was to ensure that y was large enough to ensure that the film attachment to the tripod legs did not influence the PB and node, but small enough to minimise the film surface area and thereby reduce the chance of rupture. The chosen value of y was able to produce stable PB-node systems of 0.5wt% SDS solution for tripods with a height range of 5mm$< h <$35mm and a range of liquid flow rates of 10µl/min$\leq Q \leq$300µl/min.

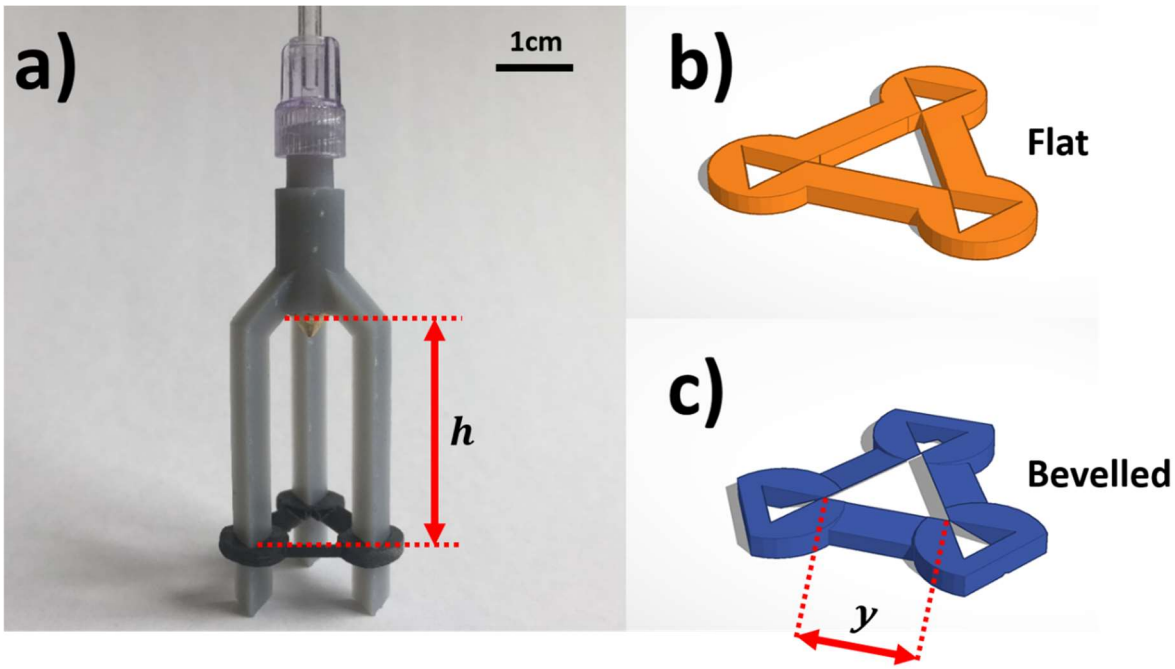

Figure 3.3. a) 3D printed frame with adjustable base, liquid injection nozzle and Luer connection for controlled flow injection of surfactant solution. b) & c) CAD drawings of frame base showing initial flat and subsequent bevelled designs respectively.

As liquid flow rate was a key control variable of the setup, great care was taken to ensure an easily reproducible liquid injection system was designed. The injection reservoir included a standard male Luer-lock connection, making it compatible with standardised disposable 1.5mm OD IV tubing and syringes. This simplified the cleaning process, reducing the chances of cross-contamination between samples. Syringes could be loaded with surfactant solution and injected directly into the upper PB at controlled liquid flow rates, Q, via a Cole-Parmer Dual Syringe Pump (Cole-Parmer Instrument Co Ltd, UK).

Initially, the liquid injection nozzle was 3D printed as part of the frame with outlet diameters of 1mm based on the dimensions used by Pitois*, et al.*[4]. However, tests using this system found that this outlet diameter caused the upper PB to 'pin' to one side at low flow rates ($Q <$ 50µl/min), causing a poorly defined vertical axis offset of the PB. Furthermore, the 0.25mm maximum print resolution meant that error margins in the outlet diameter were high. As Elias*, et al.*[9] points out, the diameter of the nozzle outlet alters fluid velocity at the point of injection, which affects the distortion of the upper PB where it attaches to the injection nozzle. In order to maintain consistency of the injection nozzle therefore, frames were printed to accommodate the attachment of commercial brass 3D extrusion printer nozzles. As these nozzles are machined to a high tolerance and a range of outlet diameters, it was possible to optimise the outlet diameter to minimise PB offsets and distortions. To this end, a final outlet diameter of 0.4mm was selected for further analysis, where liquid flow rates as low as $Q = 10$µl/min did not produce vertical axis offsets.

The final frame design was mounted inside a glass and acrylic enclosure designed to reduce disturbance from air currents as well as to increase humidity so that evaporative losses from the PB-Node geometry would be minimised.

3.2.3 PB-Node Imaging

In order to measure PB geometries, a high-resolution optical setup was required. This also necessitated the development of an appropriate image analysis technique to quantify image data into measurements of the PB radius, R, and vertical height, Z.

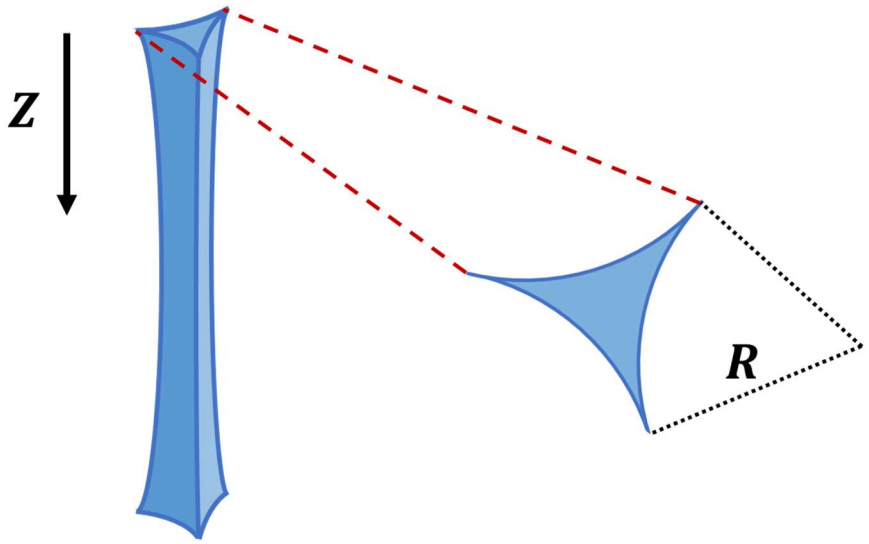

Figure 3.4. Schematic of PB profile indicating orientation of the vertical axis, Z, and the radius of the ideal PB cross-section, R.

Figure 3.5 shows the optical setup, where the enclosed frame was mounted on an optical rail, and imaged via a Manta G-031B camera (Allied Vision Technologies GmbH) with a maximum resolution of 1.5µm/pixel. An LED panel light with diffuse filter was used to illuminate the frame from behind, creating sharp contrast between the PB-node geometry and its adjoining films. The camera was mounted on a custom micrometre stage with linear translation along the Z-axis and the focal plane, as well as 90° of angular rotation such that portrait or landscape images were available. Portrait was found to maximise the information of from single images of the upper PB, while landscape could be used to image the full width of the node and lower PB's even at high magnifications.

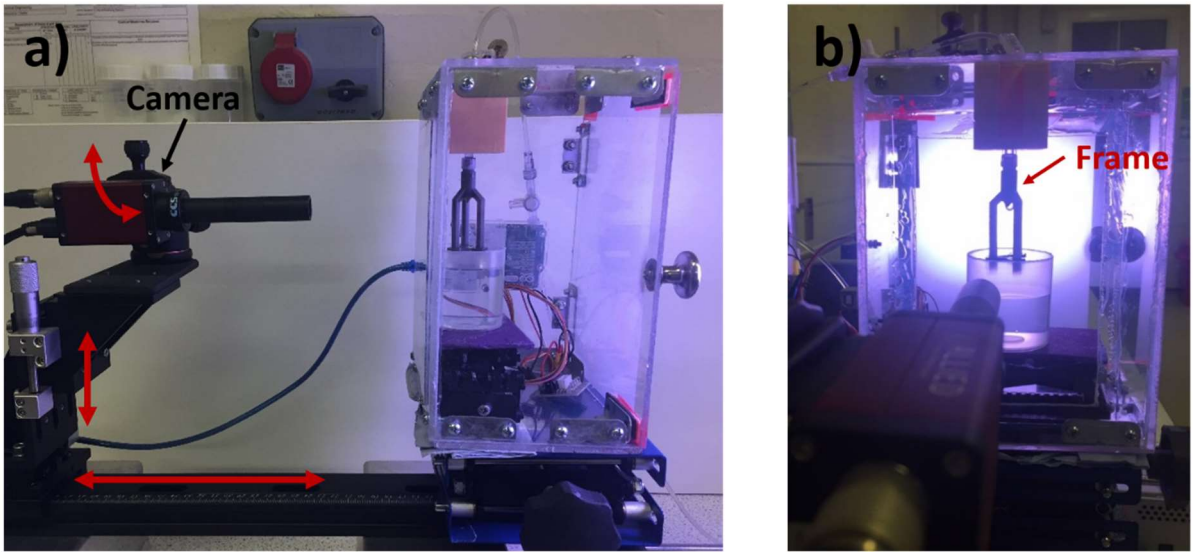

Figure 3.5. Photographs of node imaging setup. a) Side view showing mounting of CCD camera and backlit enclosure on an optical rail. b) Camera view of backlit frame inside enclosure.

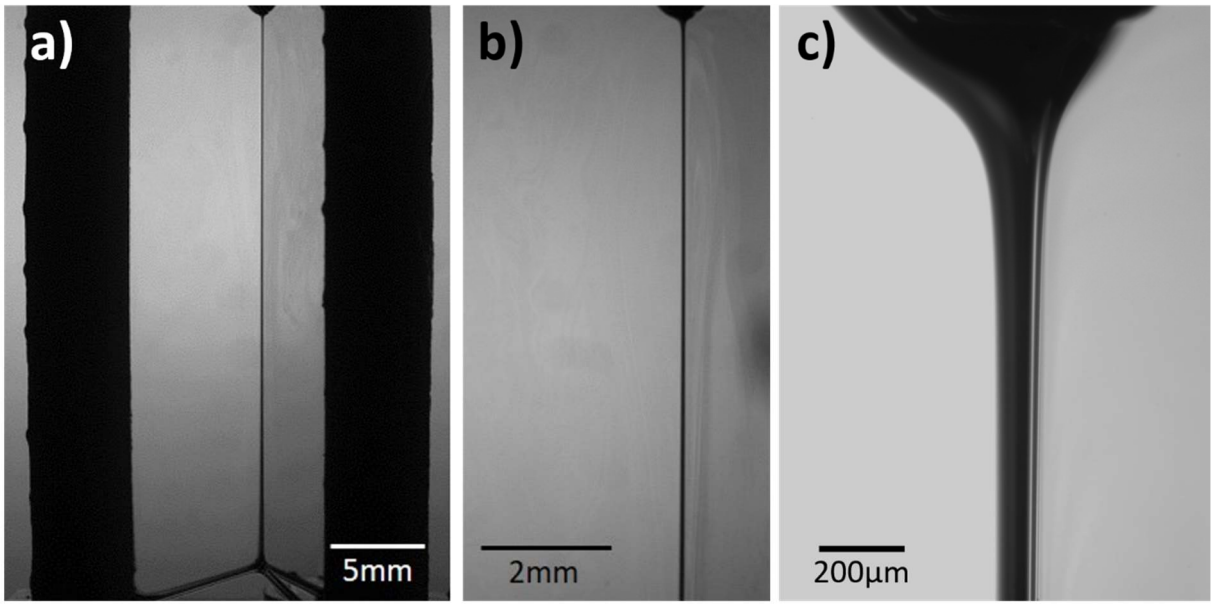

Figure 3.6. Example images of PB-node arrangement made from 0.5% SDS solution with magnifications indicated by scale bars of a) 5mm, b) 2mm, c) 200µm.

Figure 3.6 demonstrates a range of image magnifications obtained from this setup using appropriate lenses. The huge range in scale demonstrates the effectiveness of this setup for imaging effects occurring from the micrometre to millimetre scale across the entirety of the PB-node system.

3.2.3.1 PB Image Calibration

Calibration images taken at all magnifications used a 1250µm diameter syringe needle as a reference width, allowing conversion of spatial coordinates from pixels to micrometres. Measurement of the needle width was performed using digital callipers, while the corresponding image distance in pixels was undertaken using point-to-point measurement in ImageJ imaging software. From this, pixel to micrometre conversion factors could be obtained for different camera lenses.

A reference height for each experiment was performed by taking an initial image of the liquid injection nozzle at the desired magnification and using the outlet position as the vertical origin ($z = 0$).

In order to calibrate for any rotational offsets (i.e. misalignment of the camera image axis with the PB vertical axis), an initial PB image at a flow rate of 10µl/min was used. Comparison of the PB edges to an overlaid rectangular wireframe, meant that manual adjustments to image orientation would yield a rotational offset value that could be used for all subsequent images in that series of tests.

3.2.4 PB-Node Setup Loading Procedure

With the physical PB-Node setup constructed, it was necessary to define a standard experimental procedure for its effective use. This procedure was devised based on a test

solution of 0.5wt% SDS, and may require minor adaptations when considering other surfactant/emulsifier solutions.

First, a BD Plastipak 20ml syringe was filled with surfactant solution and connected to the IV tubing input of the PB-Node setup. The syringe was locked into the syringe pump and allowed to infuse until surfactant emerged from the injection nozzle and no bubbles were visible in the tubing. The CCD camera was focused on the tip of the PB injection nozzle and then adjusted vertically such that the tip of the injection nozzle (corresponding to $Z = 0$) was at the very top of the image.

Once in position, the desired liquid flow rate was set on the syringe pump and the PB-node frame was submerged and withdrawn from a beaker of surfactant solution, producing an isolated PB-Node system within the frame. Focal adjustments of the camera were made to ensure well-defined PB boundaries in the image. One minute was allowed for PBs to equilibrate at each liquid flow rate before image acquisition commenced, based on tests of equilibration time. This was inspected visually, where a halt in continuous changes to the PB geometry after its formation was taken to represent an equilibrium state. It is recommended that such tests be repeated for different surfactant solutions in order to ensure PBs are at equilibrium before measurements commence.

A minimum of three images were obtained at each liquid flow rate, where new PB-node arrangements were produced at each liquid flow rate to prevent hysteresis effects. This step may be particularly important for surfactants/emulsifiers that form permanent structures at the PB-node interfaces (e.g. surface gelation).

For high-resolution images of the full PB-node system, multiple images were required at discrete vertical increments, which were obtained by vertical translation of the camera. As the camera vertical translation was parallel to the PB vertical axis, the scale calibrations were deemed valid for all images. The number of increments was dependent upon the camera magnification, with images spanning the region of interest and partially overlapping to ensure no missing regions. These vertical 'scans' of the PB were combined during image processing (see below).

3.2.5 Image Processing

Images were captured from the CCD camera using VimbaViewer imaging software and then exported for further processing using Matlab. Initial scale calibrations were undertaken using ImageJ imaging software. The Matlab code, written for this study and used in all subsequent image processing, is provided in Appendix A.

3.2.5.1 Plateau Border Edge Detection and Radius Calculation

In order to define the edges of the upper PB and node, an edge detection algorithm was applied to raw images in Matlab. Figure 3.7 demonstrates the Canny edge detection method, which employs a user defined upper and lower intensity threshold in order to identify edges within an image. This method has been shown to be robust in detecting the presence of strong edges, while removing false edges produced by image noise[14].

The ability to adjust the sensitivity of edge detection was necessary due to the presence of coloured fringe patterns (indicating regions of localised thinning) in the adjoining films. These fringes were often well enough defined to be detected as edges (Figure 3.7b), requiring alteration of the intensity thresholds to eliminate them (Figure 3.7c).

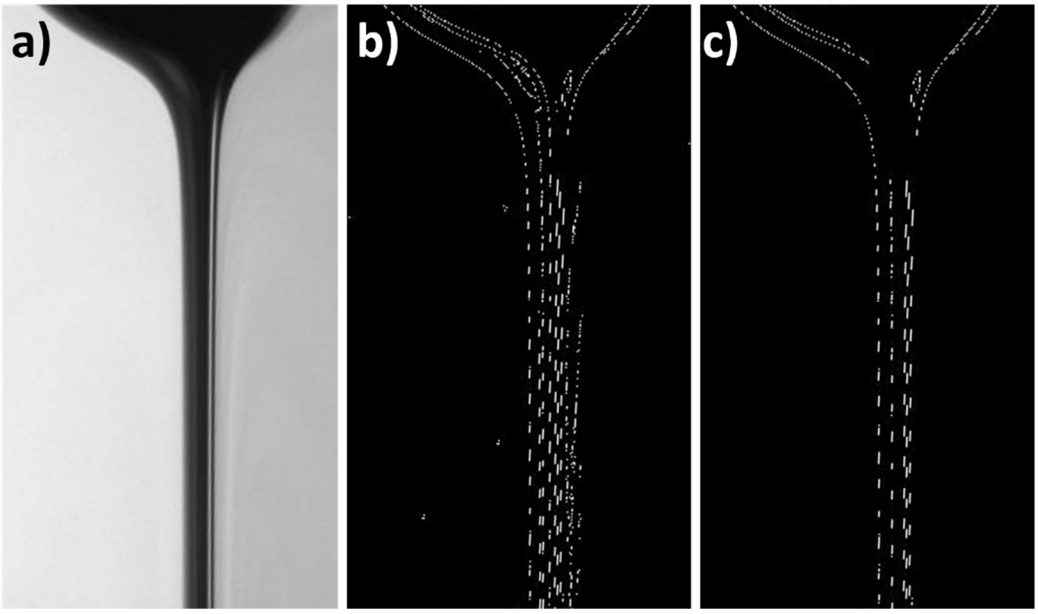

Figure 3.7. Example of upper PB image a) before Canny edge detection applied, b) after Canny edge detection applied without threshold adjustment, and c) with Canny edge detection and appropriate thresholding applied.

Due to the detection of edges within the PB profile, an automated method was required to determine profile widths while neglecting interior edges. This was achieved by scanning the image pixel matrix and recording the coordinates for the first and last white pixel encountered in each row. By subtracting the horizontal coordinate values of these two pixels a profile width, d, was determined. Conversion of PB widths into PB radii, R, was done using the relationship shown in Equation (3.1)[9]. Geometric values of Z and R were converted from units of pixels to micrometres using the appropriate scale calibration factors determined from needle measurements. An example of a raw PB image converted into Z and R coordinates is shown in Figure 3.8.

$$R = {}^{2d}/_{\sqrt{3}} \tag{3.1}$$

For high-resolution profile measurements requiring the combination of multiple images, additional steps were required. Measured geometric values were averaged at each height increment, to produce an average profile coordinate matrix. These matrices were then combined into a single high-resolution coordinate matrix, where any overlaps were averaged.

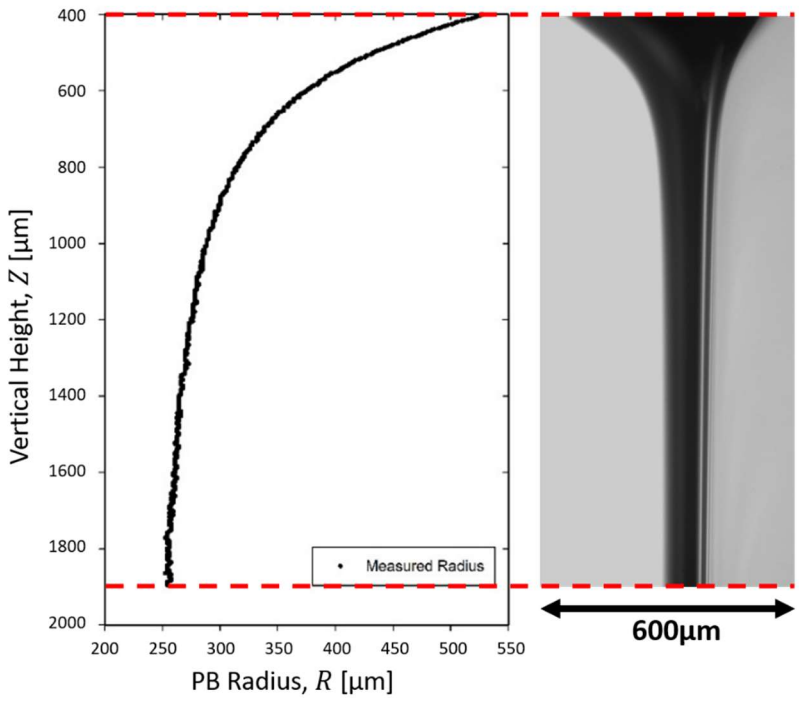

Figure 3.8. Example of a plot of measured PB height vs. PB radius for 0.5wt% solution at $Q = 260$µl/min.

Having successfully measured 'ideal' isolated PB profiles at controlled liquid flow rates, it was possible to develop theory to describe these complex geometries

3.3 Summary of Technique Development

This chapter has outlined the development of a novel experimental setup for the measurement of PB geometries in an 'ideal' isolated PB-node system at controlled liquid flow

rates. The experimental setup has been shown to accurately measure PB-Node profiles making it possible to develop and apply theory describing these geometries to experimental data. Indeed, this will be the primary focus of subsequent chapters.

The proposed setup is unique in its ability to produce high-resolution (1.5µm/pixel) images of PB-node geometries with dimensions that can be tailored by the user. In this regard, the use of transferrable 3D print designs alongside simple commercially available components make the whole setup highly adaptable and reproducible. As such, there is good scope for other researchers to utilise this setup to their own ends and gather further experimental data from these highly complex systems.

3.4 References

1 A. Saint-Jalmes, Physical Chemistry in Foam Drainage and Coarsening, *Soft Matter* **2006**, *2*, 836-849.

2 A. Lazidis; L. Parizotto; F. Spyropoulos; I. Norton, *Microstructural Design of Aerated Food Systems by Soft-Solid Materials*, **2017**; Vol. 73, p 110-119.

3 A. Anazadehsayed; N. Rezaee; J. Naser; A. V. Nguyen, A Review of Aqueous Foam in Microscale, *Advances in Colloid and Interface Science* **2018**, *256*, 203-229.

4 O. Pitois; C. Fritz; M. Vignes-Adler, Liquid Drainage through Aqueous Foam: Study of the Flow on the Bubble Scale, *Journal of Colloid and Interface Science* **2005a**, *282*, 458-465.

5 O. Pitois; C. Fritz; M. Vignes-Adler, Hydrodynamic Resistance of a Single Foam Channel, *Colloids and Surfaces A: Physicochemical and Engineering Aspects* **2005b**, *261*, 109-114.

6 O. Pitois; N. Louvet; E. Lorenceau; F. Rouyer, Node Contribution to the Permeability of Liquid Foams, *Journal of Colloid and Interface Science* **2008**, *322*, 675-677.

7 A. V. Nguyen, Liquid Drainage in Single Plateau Borders of Foam, *Journal of Colloid and Interface Science* **2002**, *249*, 194-199.

8 F. Rouyer; B. Haffner; N. Louvet; Y. Khidas; O. Pitois, Foam Clogging, *Soft Matter* **2014**, *10*, 6990-6998.

9 F. Elias; E. Janiaud; J.-C. Bacri; B. Andreotti, Elasticity of a Soap Film Junction, *Physics of Fluids* **2014**, *26*, 037101.

10 S. A. Koehler; S. Hilgenfeldt; E. R. Weeks; H. A. Stone, Foam Drainage on the Microscale Ii. Imaging Flow through Single Plateau Borders, *Journal of Colloid and Interface Science* **2004b**, *276*, 439-449.

11 J. A. F. Plateau, *Statique Expérimentale Et Théorique Des Liquides Soumis Aux Seules Forces Moléculaires*; Gauthier-Villars: Paris, **1873**.

12 K. Koczó; G. Rácz, Flow in a Plateau Border, *Colloids and Surfaces* **1987**, *22*, 95-96.

13 F. Rouyer; O. Pitois; E. Lorenceau; N. Louvet, Permeability of a Bubble Assembly: From the Very Dry to the Wet Limit, *Physics of Fluids* **2010**, *22*, 043302.

14 M. Sharifi; M. Fathy; M. T. Mahmoudi In *A Classified and Comparative Study of Edge Detection Algorithms*, Proceedings. International Conference on Information Technology: Coding and Computing, 8-10 April 2002; 2002; pp 117-120.

Chapter 4

Measuring the impact of channel length on liquid flow through an ideal Plateau border and node system.

Published as: C. Clarke; A. Lazidis; F. Spyropoulos; I. T. Norton, Measuring the Impact of Channel Length on Liquid Flow through an Ideal Plateau Border and Node System, *Soft Matter* **2019**, *15*, 1879-1889.

4.0 Abstract

The phenomenon of foam drainage is a complex multi-scale process that unites molecular level interactions with bulk foam characteristics. Foam drainage is primarily governed by the flow of liquid in the channels and junctions that form between bubbles, which are known as Plateau borders (PBs) and Nodes respectively. Existing theoretical work predicts the surface rheology of the PB and node air-liquid interface to influence liquid flow rates; however, direct experimental observations of this phenomenon remain scarce. This study recognises the clear need for a reproducible, accurate and standardised approach to directly studying liquid flow at the scale of a theoretically 'ideal' PB-node architecture.

Measurements of PB geometric profiles and their apparent surface shear viscosities, μ_s, describing the mobility of the PB interface tangential to liquid flow, were made for an aqueous solution of Sodium Dodecyl Sulfate (SDS) at varying PB lengths, l_1, and liquid flow rates in the range 10µl/min $\leq Q \leq$ 200µl/min. Geometric profiles displayed previously unobserved transitions between PB relaxation and expansion towards the node, with expansion dominating under conditions approaching conventional foam drainage. Average values of μ_s in the PB relaxation regions showed virtually inviscid behaviour, with magnitudes of 10^{-8}g/s $<$ μ_s $<$ 10^{-4}g/s for l_1 in the range 27.5mm $\gtrsim l_1 \gtrsim$ 8.0mm. Decreasing magnitudes of μ_s and degrees of shear thinning were observed with increasing l_1. This was predicted to be due to decreases in the concentration of SDS at the PB interface with increasing l_1, suggesting variations in surface tension with liquid flow rate. The action of Marangoni forces in the system were not directly measured, however a brief evaluation suggested that these could scale with liquid shear rates adjacent to the PB interface.

4.1 Introduction

4.1.1 Background

In general terms, a foam can be described as a large number of gas bubbles that are closely packed together [1]. Owing to the competing action of capillary and gravitational forces, the liquid fraction gradually decreases over time as liquid travels through the network of channels between bubbles and back into the bulk solution beneath. This phenomenon of drainage is a complex physicochemical process that ultimately leads to the collapse of the foams due to eventual film rupture and subsequent bubble coalescence [2,3].

The complexity of foam systems have necessitated a bottom-up approach from those attempting to model macroscopic drainage. By simplifying the extensive liquid network into its component channels, known as Plateau borders (PBs), and junctions or 'Nodes', the microscale building-blocks of the foam system can be better characterised and subsequently reassembled. A large body of theoretical work exists to describe PB flow[4-6]; however, corresponding experimental verification is limited due to the difficulties in observing and measuring such PB-Node architectures.

Perhaps the most detailed direct observation of liquid flow through an individual PB within a bulk foam comes from Koehler*, et al.*[7], who used confocal microscopy to measure flow profiles in individual channels and a node. Since then, a greater focus has been given to forced drainage experiments through isolated PB systems where experimental and formulation parameters are easier to control and define [8-12].

Much of the current theoretical work on isolated PB systems concerns the measurement and characterisation of interfacial properties, whose molecular origins have significant

macroscopic effects on liquid flow and thus foam drainage [13,14]. Numerous experimental techniques are available to quantify the surface rheology of aqueous solutions[15-18], however none of these account for the complex geometries and stresses of a PB-Node system[19-21]. Development of such *in-situ* techniques is therefore paramount for both the verification and improvement of current microscale drainage theory[10,22-25].

The surface parameter that has seen the most *in-situ* experimental investigation in foam systems to date is an apparent surface shear viscosity, μ_s, that ultimately relates the shear force per unit length of interface to an applied shear rate, $\dot{\gamma}_s$[26]. While the true surface shear viscosity is a material function of the surfactant solution, separation of this value from dilational viscous effects and Marangoni stresses has been shown to be highly troublesome even for analysis of simple planar interfaces. The combination of these effects into an apparent surface viscosity is however, sufficient for analysing the combined effects of the interface on liquid flow tangential to the PB vertical axis. Other publications have featured this parameter in its dimensionless form, the Boussinesq Number, B_0, which is scaled by the bulk liquid viscosity, μ, and the PB's radius of curvature, R, according to Equation (4.1):

$$B_0 = \frac{\mu_s}{\mu R} \tag{4.1}$$

PB systems with a low μ_s impart minimal shear on liquid flow, producing a more uniform flow profile resembling 'plug flow'. A high μ_s would produce profiles closer to that of the Poiseuille flow observed in rigid pipes [27]. The contrast between low and high μ_s is thought to be responsible for the two macroscopic regimes of *node-dominated* and *channel-dominated* drainage respectively, which describe whether the bulk of flow dissipation is thought to occur at the nodes or within the PBs themselves[10,13].

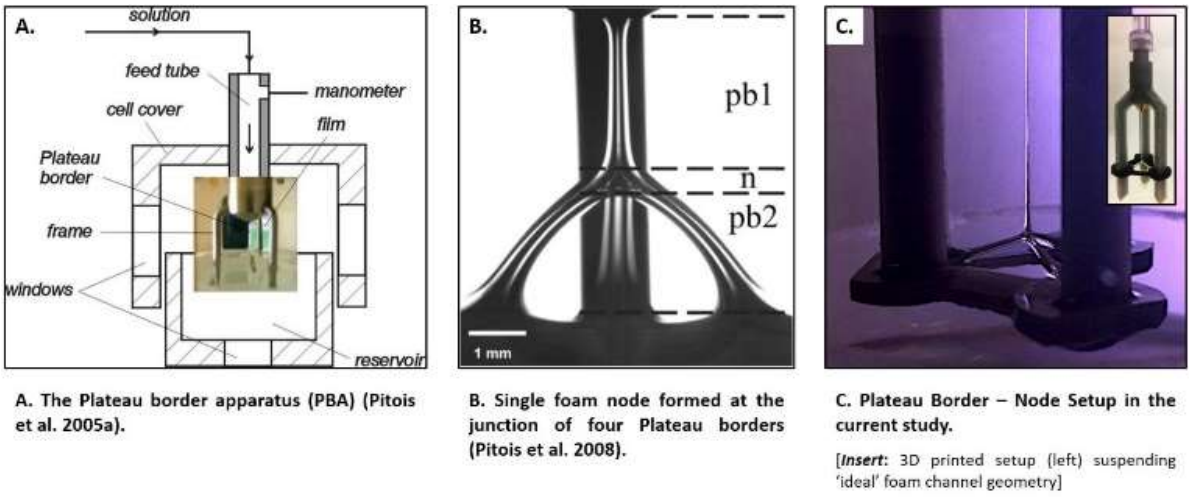

A. The Plateau border apparatus (PBA) (Pitois et al. 2005a).

B. Single foam node formed at the junction of four Plateau borders (Pitois et al. 2008).

C. Plateau Border – Node Setup in the current study.

[*Insert*: 3D printed setup (left) suspending 'ideal' foam channel geometry]

Figure 4.1. Comparison of experimental setups from A. the Plateau Border Apparatus of Pitois*, et al.*[9],[10], B. the node adapted Plateau Border Apparatus of Pitois*, et al.*[11], to C. the current PB-Node setup.

The 'Plateau Border Apparatus' of Pitois*, et al.*[10] (Figure 4.1a) has provided a wealth of information on this topic, with identification of 'mobile' and 'rigid' interfacial behaviour depending on the choice of surfactant. By measuring pressure variations within the PB, the authors were subsequently able to determine the apparent PB surface viscosities and resultant hydrodynamic resistances that inform models describing macroscopic foam permeability [5,9]. However, despite average values of these resistances being in agreement with theory, the observed variation with liquid flow rate differed significantly [5,9,28,29].

Despite its successes, there are still shortfalls of the Plateau Border Apparatus that need to be addressed. Firstly, for channels laden with high mobility surfactants, the node is known to dominate flow dissipation, and therefore must be included in investigations. Pitois*, et al.*[11] made one such study in which the Plateau Border Apparatus was adapted to include a bubble at the base of the PB (Figure 4.1b); however, the limited amount of data published was insufficient to account for large discrepancies in the current theory predicting hydrodynamic

resistance of the node [27,30-32]. In addition, the adaptation of the setup meant that the apparent surface viscosity needed to calculate hydrodynamic resistance was taken from measurements of the original PB-only system. This neglected both the potential impact of PB length variation and of variations in PB surface rheology that may have been introduced by the very presence of a node. These factors cannot be assumed and must therefore be experimentally verified.

Further challenges of such a system include the complex process of pressure measurement, where the significant timescales to achieve equilibrium [10] and induced pressure fluctuations often compromise PB and node stability. Overall, this can make the measurement procedure extremely labour intensive and therefore severely limit the amount of data that can be collected.

In order to begin to address the challenges above, the development of a purpose-built experimental setup is proposed, that can measure the apparent surface viscosity of 'ideal' PB-Node systems for a wide range of flow rates and PB lengths. This reproducible and accurate technique will add to the limited body of experimental data that exists to describe such systems, while helping to standardise the approach to studying them. Overall, it is hoped that this will improve the comparability of findings between both previous and future studies, thus enabling further progress to be made in understanding these systems.

4.1.2 Theory

The bulk of existing theory relating PB surface viscosity to PB geometry, pertains to idealised 'infinite' PBs. Owing to the complexity of PB geometries, these simplified systems help to

identify cross-sectional areas, S, such as that shown in Figure 4.2, where S is a simple function of film thickness, w, and PB Radius, R, described by Equation (4.2)[6]:

$$S(w;R) = \left(\sqrt{3}(R+w)^2 - \pi R^2/2\right) \tag{4.2}$$

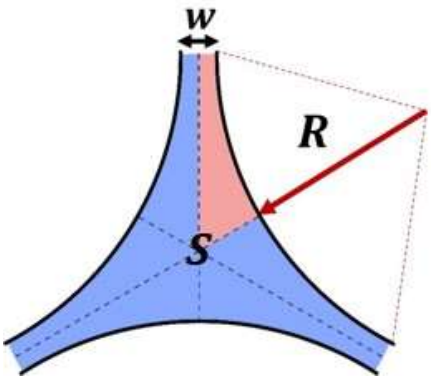

Figure 4.2. Cross-section of an infinite PB with Film Width, w, Radius of Curvature, R, and Cross-Sectional Area, S. Dashed lines indicate PB symmetry lines and the shaded region highlights one of six symmetry units.

A common approximation is applied to cases where films are thin ($w \ll R$). In these cases, S can be approximated as a function of R only (Equation (4.3)) using the geometric factor $c \approx 0.161$ [6].

$$S \approx cR^2 \tag{4.3}$$

Liquid flow through a PB is defined within the regimes of viscous and inertial flow, with viscous flow generally dominating at low flow velocities and high liquid viscosity, and inertial flow becoming more prominent with increasing flow velocity and decreasing liquid viscosity. This can be described in terms of the Reynolds number, R_{eH}, which describes the ratio of inertial to viscous forces, such that decreasing R_{eH} describes an increasing dominance of viscous flow. For an ideal, thin-filmed, PB this can be calculated from $R_{eH} = 4\rho u_r cR/\pi\mu$, where ρ is the

liquid density, μ is the liquid's dynamic viscosity and u_r is the flow velocity relative to the interface. As the viscous regime is known to dominate for liquid foam systems, this has seen the majority of theoretical and experimental study [1,6,12,13]. Therefore, in order to maximise the applicability of the current study, this work will focus only on the viscous component of the liquid flow.

The role of viscous flow in determining PB velocity profiles is described by the dimensionless parameter, D, which can vary between the limits of 'plug-flow' (i.e. flat profiles) where $D = 0$ and 'Poiseuille-flow' where $D = 312$. A derivation of this can be found from Elias*, et al.*[12]. This is dependent upon the shear imparted by the PB interface on liquid flow, which ultimately depends on the mobility of the interface, M, often referred to in its inverted form, the Boussinesq number, $B_0 = 1/M$.[12] The current benchmark relationship between D and B_0 is the numerical solution of Nguyen[5], which describes the data given by solving the Navier-Stokes Equation for flow in an ideal 'infinite' PB (Equation (4.4)). This has been shown to agree well with subsequent model extensions and experimental analysis in macroscopic foam systems by Koehler*, et al.*[6],[7] .

$$D^{-1} = c\left[0.02 + \left\{0.0655{B_0}^{-0.5}/\left(0.209 + {B_0}^{0.628}\right)\right\}\right] \quad (4.4)$$

In order to relate Equation (4.4) to measureable variables, further considerations of PB geometry are required. Elias*, et al.*[12] describe the ideal relaxation profile of a vertical PB with thin films according to an approximated solution to Equation (4.5), which is commonly referred to as 'the standard drainage theory'. This itself is a steady state solution to the Navier Stokes Equation for fluid momentum, in the specific case of a PB tangential to the vertical axis, Z, with liquid flow rate, Q, surface tension, γ, and kinematic viscosity, $\nu = \mu/\rho$ describing the

ratio of dynamic viscosity and fluid density respectively. The dimensionless parameter, I, is an inertial flow parameter whose role will become apparent in subsequent chapters.

$$\frac{dR}{dZ} = \frac{cD\nu Q - {}^{2}R^{4}}{\left(\frac{2IQ^{2}}{R}\right) - \left(\frac{c^{2}R^{2}\gamma}{\rho}\right)} \tag{4.5}$$

$$R = R_e + (R_0 - R_e)e^{-z/L} \tag{4.6}$$

The approximated geometric solution (4.6) describes the transition of the PB profile from some initial radius, R_0, to an equilibrium radius, R_e, along the vertical axis, Z, according to a relaxation length, L. The equilibrium radius is analogous to the constant radius of the theoretical 'infinite' PB, where gravitational forces and viscous dissipation are balanced. This can be derived from Equation (4.5), where $dR/dZ = 0$ (i.e. constant radius), leading to the ratio of viscous dissipative and gravitational terms shown in Equation (4.7)[12].

$$R_e = (D\mu Q/c\rho g)^{1/4} \tag{4.7}$$

As such, combining Equations (4.4) and (4.7) into Equation (4.8) yields a relationship between PB geometry, bulk liquid variables and surface mobility of the equilibrium (or 'infinite') PB with a thin film approximation.

$$\frac{\mu Q}{\rho g c^{2} {R_e}^{4}} = 0.02 + \left\{0.0655 {B_0}^{-0.5} / \left(0.029 + {B_0}^{0.628}\right)\right\} \tag{4.8}$$

In order to maximise the comparability of the results presented here to existing work, values obtained for B_0 are converted into surface shear viscosities, μ_s, using Equation (4.1) (with $R = R_e$).

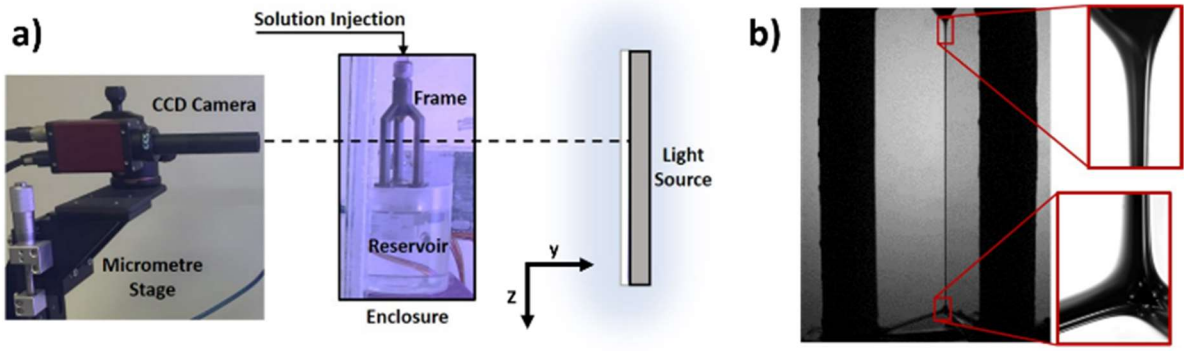

Figure 4.3. Imaging for analysis of PB-Node profiles. a) Optical Setup - A CCD camera images the enclosed frame using a rear diffuse panel light to create shadow profile images. b) Low and high magnification images of a PB node profile, where highest magnification (red highlighted images) represents 1.5µm per image pixel.

4.2 Experimental

4.2.1 The PB – Node Setup

The current setup formed an ideal PB and node by submerging and withdrawing a closed 3-legged frame geometry into surfactant solution (Figure 4.1c). Flow rates, Q, were accurately controlled via a Cole-Palmer Dual Syringe Pump, which could directly inject surfactant solution into the upper PB through brass 3D print nozzles with outlet diameters of 0.4mm. Larger diameter nozzles were found to cause pinning of the PBs to one side of the nozzle at low flow rates, thereby distorting the ideal profiles.

The frame was designed using Tinkercad software (Autodesk inc., USA) and 3D printed using stereolithography on a FormLabs Form® 2 printer, as this approach offered fast and simple production of precision tailored geometries. The distance between the legs and central tripod axis was set at $\boldsymbol{x}$ =6.40mm and heights were varied to produce PB lengths of 27.5mm,

15.0mm and 8.0mm with absolute errors of approximately 0.5mm. These heights were both above and within the ranges used in existing setups [9-12]. The error in PB length resulted from the uncertainty in the exact end of the PB and beginning of the node.

The frame was mounted and enclosed within an acrylic and glass fronted box to allow imaging, minimise liquid evaporation and to remove air current disturbances. Access from a rear panel allowed investigators to lift and withdraw containers of surfactant solution from the frame. The whole system was then mounted on an optical rail to aid in PB profile imaging.

PB profiles were obtained by illumination from the rear of the setup with a diffuse LED panel light and imaging via CCD camera from the front. A micrometre translation stage with translation in both the Z and Y directions, allowed precision movement of the CCD camera relative to the PB and node (Figure 4.3a).

The resolution of images varied based on the choice of lens. Image resolution was calculated based on calibration images of a syringe needle with measured diameter 1.250 ± 0.006 mm. The maximum resolution of 1.5µm per image pixel was used for curve fitting. Due to the high magnification at this resolution, it was necessary to combine multiple images along the Z-axis in order to visualise the full length of the PB profile (Figure 4.3b). Images were obtained in triplicate at 1000 ± 5 µm increments along the Z-axis, then processed and combined in Matlab (MathWorks, USA).

PB profile widths, d, were measured on a pixel row-by-row basis, using a Canny edge detection algorithm to determine PB boundaries. This method has been shown to be robust in detecting the presence of strong edges, while removing false edges produced by image noise [33]. The sensitivity of the edge detection could be varied by adjusting the upper and lower intensity

thresholds used by the algorithm to determine edge strength. As such, it was possible to identify only PB profile edges, neglecting any fringe patterns in the adjoining films due to localised thinning.

Profile widths, d, were converted into PB radii, R, using the geometric correction factor $2/\sqrt{3}$[12] such that:

$$R = 2d/\sqrt{3} \tag{4.9}$$

Values for the PB Radii were averaged for each of the 1mm incremental images along the Z-axis and subsequently combined into a single matrix of Z values and corresponding R values in the range $0 \leq Z \leq l_1$.

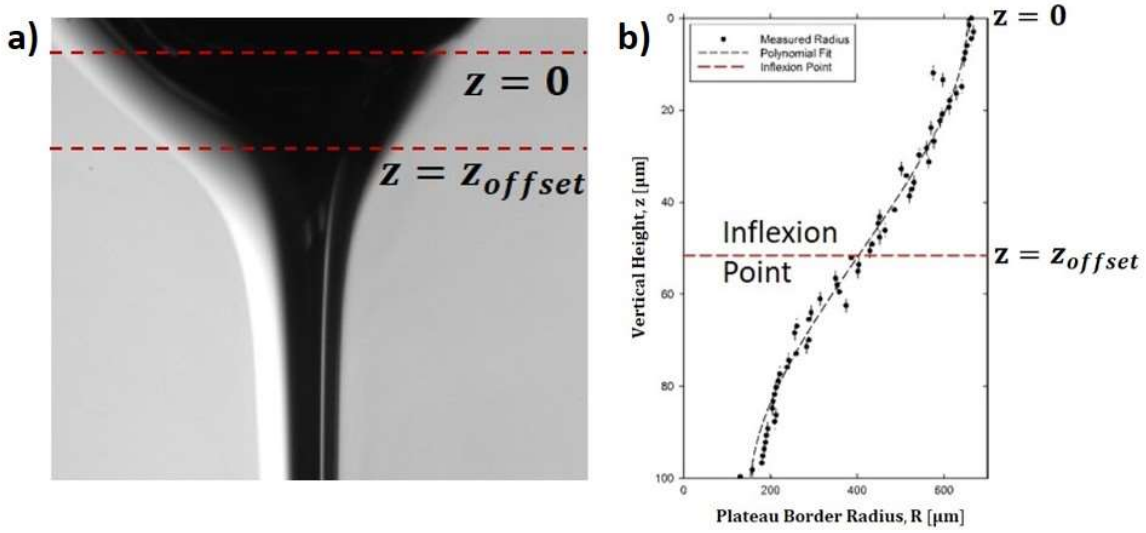

Figure 4.4. a) Example of PB profile at Q = 20µl/min, with nozzle height (Z = 0) and vertical offset ($Z = Z_{offset}$) indicated by red dashed lines. b) Corresponding Z vs. PB Radius, R, plot for the region of the distortion with outliers removed. A third order polynomial is used to illustrate the shape of the distortion and the second order derivative set to zero determines the vertical height of the inflexion point, Z_{offset} (red line).

As was observed by Elias*, et al.*[12], around $Z = 0$mm the PB exhibited a significant distortion due to its attachment to the liquid injection nozzle. This distortion was thought to mark a transition from a circular PB cross-section to an ideal cross-section (Figure 4.2) just below the point of injection. A vertical offset, Z_{offset}, was therefore defined at the inflexion point of the distortion (see Figure 4.4), below which the ideal PB cross-section could be assumed and curve fitting undertaken.

The PB equilibrium radius was determined by fitting Equation (4.6) to values of R and Z using a non-linear least square fit method. R_e values were then combined with measurements of μ and ρ to calculate the left hand side of Equation (4.8). A least squares method was used to solve Equation (4.8) for B_0, with these values subsequently converted to μ_s using Equation (4.1) with $R = R_e$.

A solution of 0.50wt% SDS was selected for analysis owing to its extensive use in previous work and its ability to easily produce stable films. This concentration was approximately double the Critical Micelle Concentration (CMC) of $\sim$ 0.235wt% [34], ensuring that observations would be of a fully populated interface, where little variation in surface tension could be assumed.

SDS solution was loaded into the PB-Node setup and PB profiles measured for flow rates in the range 10µl/min$\leq Q \leq$200µl/min, therefore extending beyond the range of conventional foam drainage experiments[10]. This was in order to maximise the available data with which to investigate flow dependent trends.

4.2.2 Preparation of SDS Solutions

SDS (>99.9%) from Fisher Scientific (Loughborough, UK) was weighed using a digital balance to an accuracy of three decimal places. Purified water (15.0 MΩ·cm) was weighed into

borosilicate glass beakers and magnetically stirred at room temperature while SDS was added. Beakers were covered with cling-film to reduce evaporative water loss or contamination. Stirring continued for a minimum of 30 minutes prior to use of the solution. Great care was taken to ensure that glassware and stirring bars were thoroughly cleaned and rinsed with purified water, then air dried prior to use. Nitrile gloves were worn throughout handling to avoid sample contamination.

Bulk properties ρ and μ were measured in triplicate using a Krüss Processor® Tensiometer K100 (Krüss GmbH, Germany) with density hook attachment and silicon density standard, and a Malvern Kinexus® Pro rheometer (Malvern Panalytical, UK) with Double-Gap geometry respectively. The averaged results with accompanying measurement errors were then used in the calculation of μ_s.

4.3 Results and Discussion

4.3.1 SDS Solution Properties

Values for specific bulk properties of the 0.50wt% SDS solution, that are subsequently used for the calculation of μ_s (according to equations 4.1 and 4.7), are presented in Table 4.1.

Concentration [wt%]	Fraction of CMC	Density [mg/ml]	Viscosity (10^{-4}) [Pa·s]
0.50	~ 2.13	998.7 ± 0.9	9.84 ± 0.05

Table 4.1. Averaged bulk properties of 0.50wt% SDS solution with associated errors[34].

4.3.2 PB Relaxation and Expansion

Images of PB profiles revealed a previously unreported phenomenon, where sudden rapid increases in PB radius could be seen at discrete distances, Z_{swell}, along the PB (see Figure 4.5),

that changed with liquid flow rate and PB length (see Figure 4.6b). This appeared to mark a transition from the 'relaxation' (i.e. $dR/dZ < 0$) of the PB described by Equation (4.6) to a state of 'expansion' (i.e. $dR/dZ > 0$), where the PB eventually transitioned into the adjoining node at $Z = l_1$.

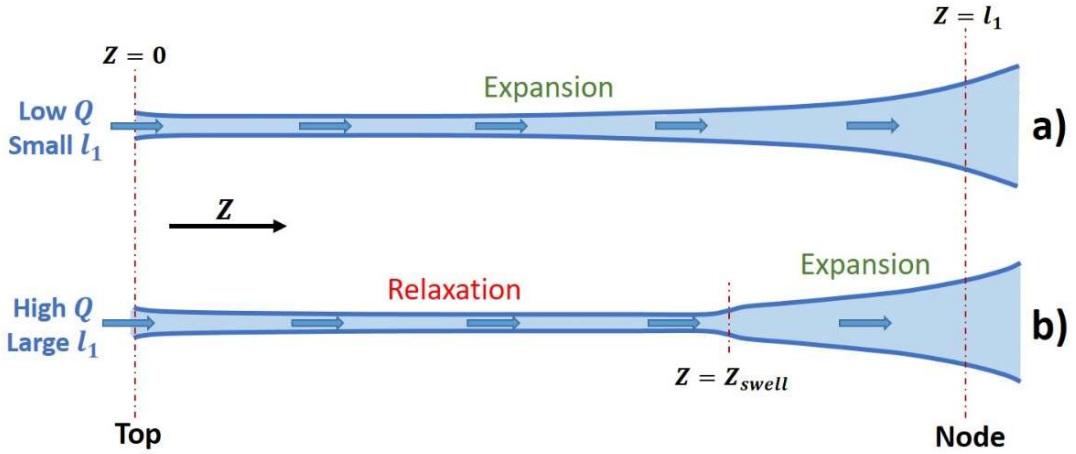

Figure 4.5. Visualisation of PB profiles of length, l_1, and liquid flow rate, Q. a) Low Q, small l_1 resulted in almost complete expansion profiles. b) Increasing Q and l_1 exhibited both relaxation and expansion with increasingly prominent transition distortions at height $Z = Z_{swell}$.

Measurements of the PB profiles clearly highlighted the Q dependence of Z_{swell}, which determined the extent to which the PB profile was dominated by relaxation or expansion. The Expansion Fraction, Φ_e, of the total PB length was described by $\Phi_e = 1 - Z_{swell}/l_1$, and can be seen to vary accordingly with Q in Figure 4.6b. At lower flow rates, expansion was seen to almost completely dominate the PB profile until a critical flow rate, Q_{crit}, after which Φ_e decreased. Q_{crit} increased with decreasing l_1 as shown in the inset of Figure 4.6b, resulting in the increasing dominance of expansion for shorter PBs. Values of Q_{crit} were 50µl/min, 100µl/min and 160µl/min for $l_1 \approx$ 27.5mm, 15.0mm and 8.0mm respectively.

These findings are highly significant in the context of microscale foam drainage and therefore potentially in macroscopic foam systems. As flow rates and PB lengths approached those more typically observed in foam drainage experiments[10] (i.e. Q <100µl/min and l_1 <10mm), PB relaxation all but disappeared in favour of an expansion limited by the spatial geometry of the adjoining node. This therefore represents an important consideration to be made when choosing suitable theory to describe PB profiles.

The differing nature of all existing experimental work in this area meant that this phenomenon was not observed[9-11,35]. Firstly, the few isolated PB and PB-Node experiments mainly focused on shorter PB lengths, $l_1 < 15$mm and the range of Q was smaller, 0µl/min $\leq Q \leq$ 100µl/min in the case of Pitois*, et al.*[9],[10,11]. In the only case where PB length was longer ($l_1 \approx 40$mm), flow rates were in significantly higher increments of 5ml/min in the range 0ml/min $\leq Q \leq$ 40ml/min, with considerably poorer image resolution[12]. This indicates that previous experiments would either have observed only expansion-dominated PB profiles (e.g. Pitois et al.[9-11]), or relaxation-dominated PB profiles (e.g. Elias*, et al.*[12]), where the swelling region may have been obscured by a combination of distortion at the node or the point of liquid injection and insufficient image resolution. The range of flow rates and PB lengths studied by the current experimental setup therefore make it unique in its ability to observe both expansion and relaxation states simultaneously.

As the current theory does not describe the swelling phenomenon observed here, both this and the PB expansion regions should not be considered in the subsequent analysis of PB profiles. Instead, curve fitting of Equation (4.6) to experimental data is limited to the relaxation region only (see Figure 4.7).

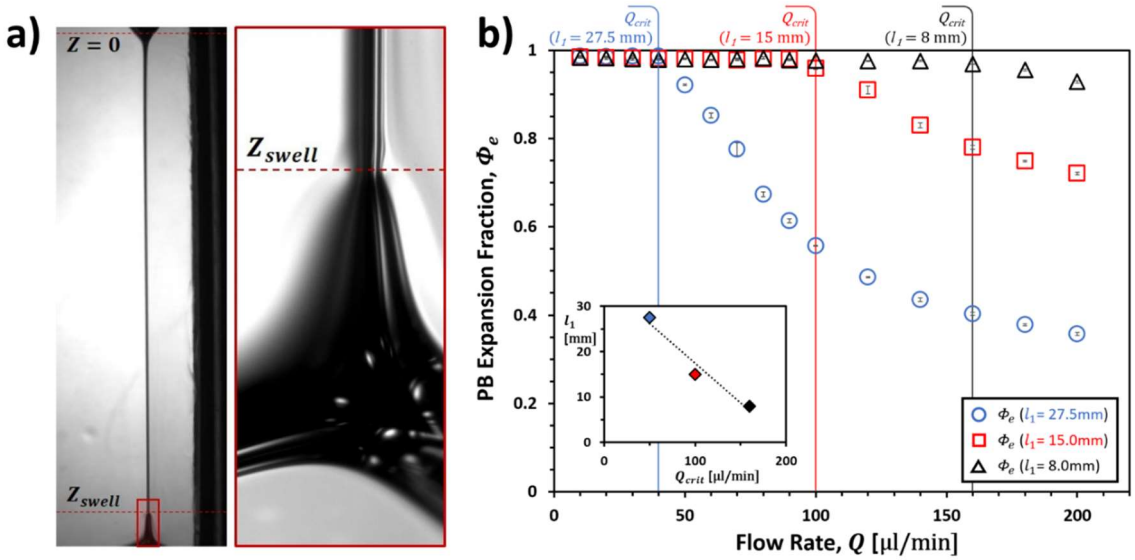

Figure 4.6. a) Raw PB-Node profile images for low (left) and high (right) magnifications at $l_1 \approx$ 27.5mm and Q = 200µl/min. Z_{swell} indicates the distance of the swell below the injection nozzle. b) Expansion Fraction, Φ_e, vs. Flow Rate, Q, for PB lengths 27.5mm, 15.0mm and 8.0mm. Critical flow rates, Q_{crit}, are seen at 50µl/min, 100µl/min and 160µl/min for PB lengths 27.5mm, 15.0mm and 8.0mm respectively, with the relationship between l_1 and Q_{crit} shown inset. Colours correspond to PB lengths as shown.

4.3.3 Length and Flow Dependence of PB Geometry

Due to the fundamental differences noted between the present experimental setup and others (primarily the range of liquid flow rates and PB length), only limited comparisons could be made to existing experimental data. Neither the influence of a node on the upper PB nor the specific impacts of height variations are well documented in the literature; however, the differences in data obtained here serve to highlight the potential significance of these factors. Experimental data were fitted to Equation (4.6) in order to extract values for the equilibrium radius, R_e, which describes the theoretically ideal infinite PB, therefore validating the use of

the theory described in section 4.1.2. The fit quality was high in all cases, with a minimum r-Squared value of 0.87 due to fluctuations in the PB around Q_{crit}, but the majority over 0.95. The values of R_e were converted to Equilibrium Cross-Sectional Areas, S_e, using Equation (4.3) with $R = R_e$. These were compared to the minimum cross-sectional areas, S_{min}, measured by Pitois*, et al.*[10] for a 3g/l SDS solution with $l_1 < 15$mm (Figure 4.8). It is important to note here that values of S_{min} may not have corresponded to equilibrium cross-sectional areas, which were the basis for the theory used in their subsequent calculations. For PBs of insufficient length, it is likely that values for S_{min} would have been higher than S_e, with a potentially significant impact on the observed flow dependent trends and magnitudes of calculated values.

As it was predicted above that Pitois*, et al.*[10] may only have observed an expansion-dominated PB, measurements were also made of the minimum cross-sectional area in the PB expansion region, S_{Exp}, for $Q > Q_{crit}$ (Figure 4.8). This would serve to highlight any changes in PB geometry that were characteristic of expansion rather than relaxation, where S_{Exp} would better represent Pitois' S_{min} than S_e. The measurement of S_{Exp} was taken from the PB profiles at the approximate point where the swelling region had transitioned into a continuous expansion towards the node (see Figure 4.7). The difficulty in precisely defining these points is reflected in the error margins.

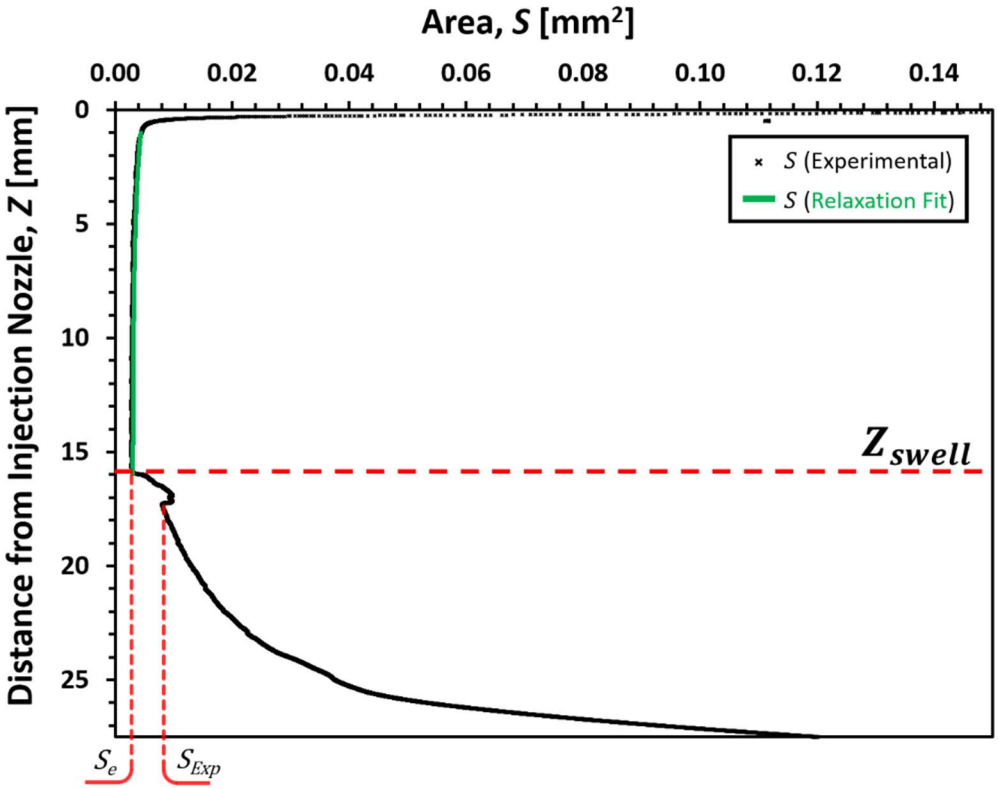

Figure 4.7. PB Cross-Sectional Area, S, vs. Vertical Height, Z, for $Q = 100\mu l/min$ with $l_1 \approx 27.5mm$. The green line shows the fit of Equation (4.6) to the relaxation region of the profile. Red dashed lines indicate the end of the relaxation region (red), defined as Z_{swell}, as well as the Equilibrium Cross-Sectional Area, S_e, and the Minimum Expansion Cross-Sectional Area, S_{Exp}, all labelled accordingly.

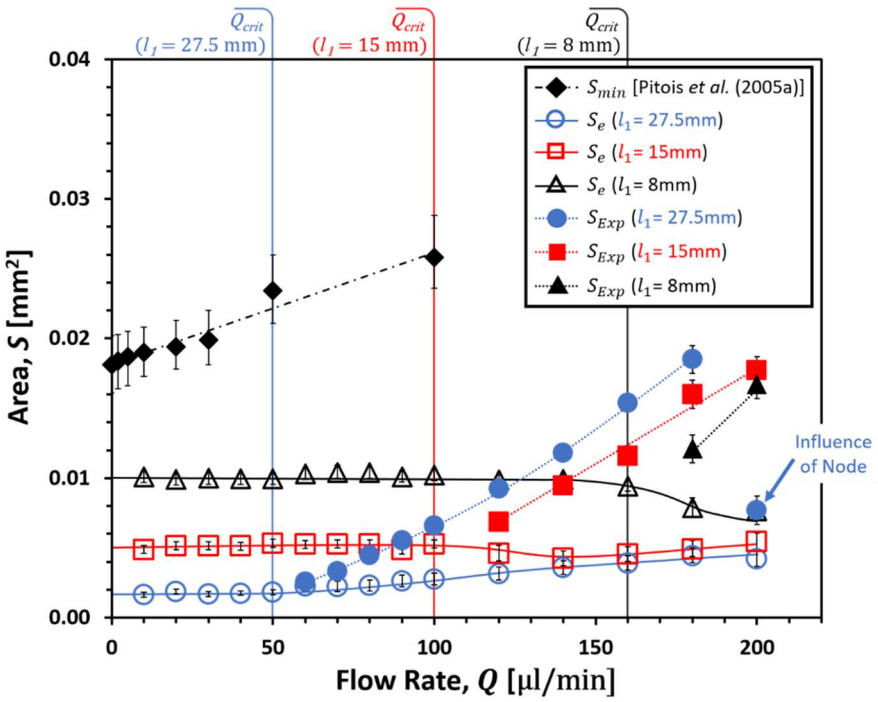

Figure 4.8. Flow Rate, Q, vs. PB Cross-Sectional Area, S. Data presented here is for 0.50wt% SDS solution with PB lengths $l_1 \approx$ 27.5mm, $l_1 \approx$ 15.0mm and $l_1 \approx$ 8.0mm. Unfilled data-points represent minimum PB relaxation cross-sectional areas, S_e, while filled points represent minimum PB expansion cross-sectional areas, S_{Exp}, for $Q > Q_{crit}$. Data is compared to the Minimum PB Cross-Sectional Area, S_{min}, measured by Pitois, *et al.*[10] for 3g/l SDS solution with $l_1 <$ 15mm. Lines are included to guide the eye. S_{Exp} for $l_1 \approx$ 27.5mm at 200µl/min shows a significant deviation from other data resulting from its close proximity to the node.

From Figure 4.8 it can be seen that PB length had a significant impact on the magnitude of S_e before Q_{crit} was reached. In this region, S_e was invariant to Q and increased in magnitude with decreasing l_1. At flow rates above Q_{crit}, values of S_e from the different PB lengths began to converge. This suggested that the impact of PB length on the equilibrium PB cross-section could become insignificant for flow rates at the top end of those measured here and above.

The projected trend of increasing S_e with decreasing l_1 could have conceivably produced magnitudes of S_e comparable to the S_{min} values reported by Pitois*, et al.*[10], with a PB length of approximately 4mm. This would fall within their range of $l_1 <$ 15mm, however it does not account for the positive correlation between S_{min} and Q. It was only from the values of S_{Exp} for $Q > Q_{crit}$ that a significant increase in area with flow rate was observed. This suggested that the increase in S_{min} with flow rate observed by Pitois*, et al.*[10] could be a characteristic of the PB expansion region, albeit without the delay imposed by Q_{crit}. It is hypothesised that the PB-only nature of Pitois' setup may have been responsible for the lack of a Q_{crit} in their data. By terminating in the bulk liquid instead of the strict geometry of a node, the expansion profile of the PB would have been far less restricted, potentially explaining the immediate increase in S_{min} from Q = 0µl/min.

Based on the observations made here, it seems unlikely that S_{min} accurately represented an equilibrium PB cross-section in Pitois *et al.*'s measurements. This would have introduced a degree of error in values subsequently calculated using idealised PB theory, the consequences of which are discussed further in section 4.3.4. It is emphasised here that the proposed method for extracting the true values of S_e from experimental PB profiles is vital for the accuracy of subsequent calculations using ideal infinite PB theory.

4.3.4 Length and Flow Dependence of Apparent PB Surface Viscosity

The flow rate dependence of the apparent surface shear viscosity, μ_s, was calculated as described in section 4.1.2, the results of which can be found in Figure 4.9.

It was seen that that decreasing l_1 produced values of μ_s that approached those of Pitois*, et al.*[10]. Their average μ_s in the range 10µl/min$\leq Q \leq$100µl/min was 1.57 × 10^{-5} g/s for $l_1 <$

15mm, in comparison to a value of 2.16 × 10^{-5} g/s for $l_1 \approx$ 8.0mm determined here. It should be stressed that values published by Pitois, *et al.*[10] were for a slightly lower concentration (3g/l) of TTAB solution rather than SDS, however the authors reported their SDS data to have been similar. Equations 6 and 7 highlight the importance of accurate measurements of the equilibrium PB cross-section when using idealised 'infinite' PB theory to calculate μ_s. Here it can be seen that overestimations of S_e would have resulted in overestimations of μ_s. For the case of $S_{min} > S_e$ therefore, as described in section 4.3.3, it can be seen how this may have obscured flow dependent behaviour and increased the magnitude of μ_s measured by Pitois, *et al.*[10].

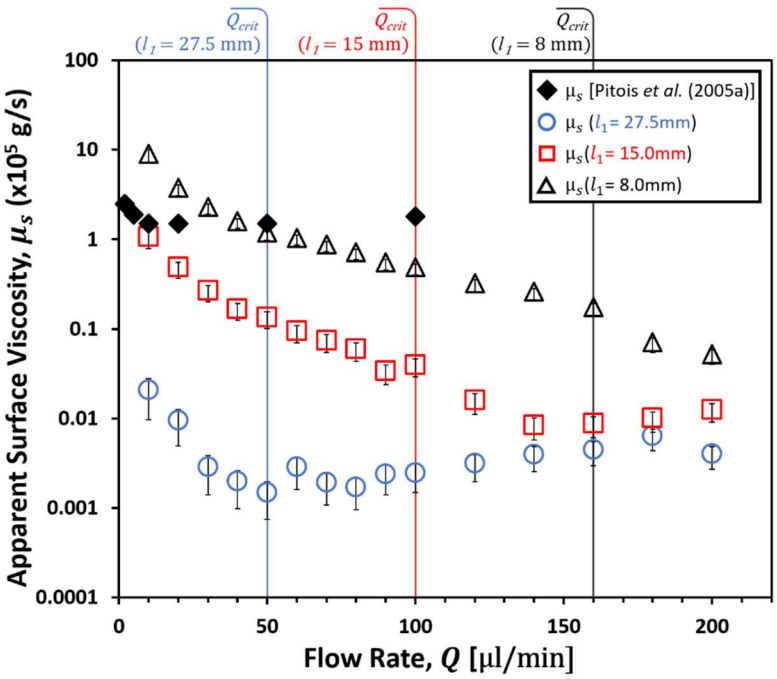

Figure 4.9. Apparent Surface Viscosity, μ_s (x10^5 g/s), vs. Flow Rate, Q, for 0.50wt% SDS solution with PB lengths $l_1 \approx$ 27.5mm, $l_1 \approx$ 15.0mm and $l_1 \approx$ 8.0mm. Critical flow rates, Q_{crit}, before PB expansion are indicated for each. Data is compared to that of Pitois *et al.*[10] for 3g/l Tetradecyltrimethylammonium Bromide (TTAB) solution with $l_1 <$ 15mm, which was said to have exhibited similar results to SDS solutions.

The range of values shown here for μ_s with varying l_1, showed a good agreement with those measured in the high precision setup of Zell*, et al.*[17] who reported $\mu_s \lesssim 10^{-5}$ g/s for the true surface shear viscosity, in comparison to values of $10^{-8} < \mu_s < 10^{-4}$ g/s for the apparent surface viscosity presented here. Zell's results are argued to be the most accurate measurements of SDS surface shear viscosity to date, where 10^{-5} g/s represented virtually inviscid behaviour at the limit of their technique's sensitivity. The ability of the new technique to extract values as low as 10^{-8} g/s therefore represents a significant step forward in measurement sensitivity. Furthermore, the ability to measure the flow dependent variations in μ_s at this scale could provide a wealth of information regarding the dynamics of the interface.

In order to interpret the origin of the flow and length dependent trends in μ_s, it was most useful to consider the shear imparted by the bulk liquid on the interface, which takes into account the variations in the PB cross-sectional area. The average liquid shear rate within the equilibrium PB, $\dot{\gamma}_s$, for a given geometry and flow rate was approximated from Equation (4.10) (Elias*, et al.*[12]), with the results shown in Figure 4.10a.

$$\dot{\gamma}_s \approx Q/cR_e{}^3 \tag{4.10}$$

Due to the flow rate independence of S_e prior to Q_{crit}, the resulting shear rates in these regions approximately scaled with Q. Here the apparent surface viscosity increased with decreasing $\dot{\gamma}_s$, initially being well described by power laws, but beginning to deviate towards finite values of μ_s for the lower values of $\dot{\gamma}_s$.

For flow rates larger than Q_{crit} a distinctive change in the behaviour of μ_s with $\dot{\gamma}_s$ was observed, reflecting the transition to a Q dependent S_e (Figure 4.10a). From this point, the data for all PB lengths began to converge abruptly, following what appeared to be a single

trend of decreasing μ_s with $\dot{\gamma}_s$. While additional PB length data is required to confirm this, it would imply that this flow region marked a response of the PB interface that was similar for all PB lengths. Indeed, the appearance of maximum shear rates for $l_1 \approx$ 27.5mm (blue points) and $l_1 \approx$ 15.0mm (red points), where μ_s appeared to increase, implied a resistance of the interface to further apparent shear thinning. These maximum shear rates also corresponded to the beginning of expansions of the PB cross-sections (see Figure 4.8) implying a causal link between interfacial resistance and expansion.

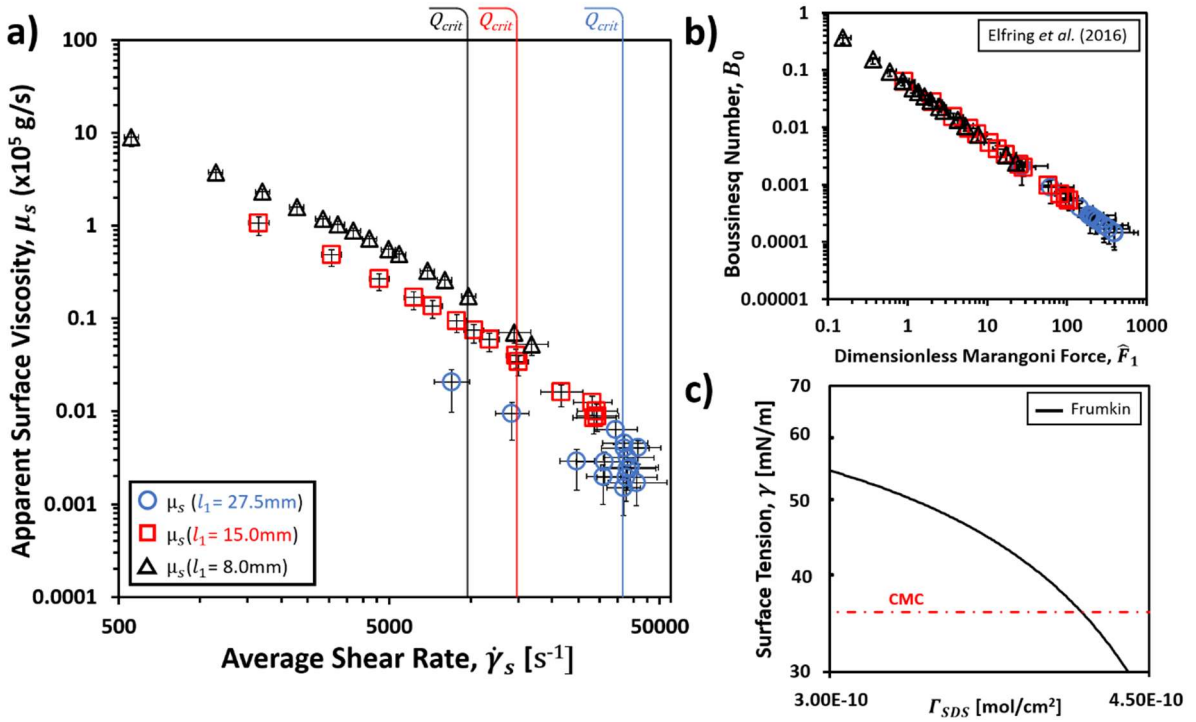

Figure 4.10. a) Apparent Surface Viscosity, μ_s (x10^5 g/s), vs. Average Shear Rate, $\dot{\gamma}_s$, for 0.50wt% SDS solution with PB lengths $l_1 \approx$ 27.5mm, $l_1 \approx$ 15.0mm and $l_1 \approx$ 8.0mm. Critical flow rates, Q_{crit}, before PB expansion are indicated for each. b) Calculated Dimensionless Marangoni Force, $\hat{F}_1$, vs. Boussinesq Number, B_0, from different l_1 PBs for virtually inviscid surface viscosity[36]. c) Frumkin Isotherm for SDS at surface concentrations, Γ_{SDS}, approaching the CMC using model parameters of Kinoshita *et al.*[37].

The apparent shear thinning of the PB interfaces could have resulted from two primary effects: changes in surfactant concentration at the PB interface, and/or the non-trivial combination of surface dilational viscosity and Marangoni forces with the surface shear viscosity[36,38], which describe surfactant transport across the interface due to dilation, distortion and shear of the interface respectively. Both of these are influenced by rates of adsorption/desorption, which are not taken into account during the present study. A full numerical analysis of these effects represents a complex task that is beyond the scope of this study; however, initial comparisons to theory and experimental observations by other authors were able to suggest a physical basis for the observed trends.

In a recent study by Elfring *et al*.[36] it was shown that very low surface viscosity interfaces, such as those described here, are expected to experience increasing Marangoni forces, $\hat{F}_1$, upon applied forces to the interface according to:

$$\hat{F}_1 \sim 2/25 B_0 \sqrt{1+\alpha} \tag{4.11}$$

Where $\alpha = O(1)$ and represents the ratio of surface dilational to shear viscosities, and $B_0 \ll 1$. The divergence of this term as $B_0 \to 0$ was justified as a result of the limits of their problem, where instead it would be expected that $\hat{F}_1 \to$ constant, as $B_0 \to 0$. The results of Equation (4.11) when applied to the values of B_0 obtained here are shown in Figure 4.10b, to demonstrate the scaling of $\hat{F}_1$ with B_0. Figure 4.11 shows how the contribution of Marangoni forces to the apparent surface viscosity would have been expected to scale with increasing shear rates and could therefore have been responsible for the apparent shear thinning behaviour. Furthermore, the apparent tendency of μ_s towards a constant value with

decreasing $\dot{\gamma}_s$ noted previously, reflected the behaviour that would be expected from Figure 4.10b were it not for the limitations of Equation (4.11) discussed above.

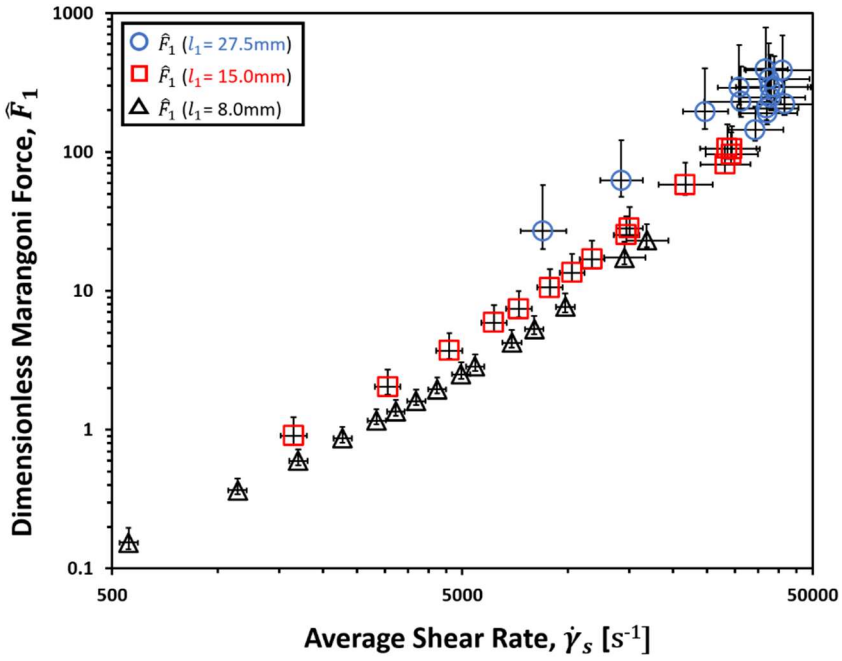

Figure 4.11. Average Liquid Shear Rate, $\dot{\gamma}_s$, vs. predicted Dimensionless Marangoni Force, $\hat{F}_1$, for surface shear viscosity data measured at PB lengths l_1 ≈27.5mm, 15.0mm and 8.0mm.

The theory of Elfring *et al.*[36] relies upon a limited degree of compressibility of the interface in order to form the concentration gradients necessary to produce Marangoni forces. The increase in surfactant concentration, Γ, at the interface results in a decrease in the surface tension that is well described by theory and experiment alike[37,39-43]. Figure 4.10c shows the theoretical relationship using the Frumkin isotherm adsorption model with model parameters for pure SDS solution as described by Kinoshita *et al.*[37]. At the CMC, the formation of micelles in the bulk liquid and the subsequent reduction in the energy barrier limiting surfactant desorption tends to reduce further compression of the interface[44]. This would imply that around this point, any differences in the interfacial structures caused by PB length

dependence should have become less pronounced. The convergence of the μ_s data in Figure 4.10a at flow rates above Q_{crit} could therefore represent the tendency towards a common limit of interfacial compressibility for the different PB lengths.

Based on the analysis so far, a logical prediction for the strong PB length dependence of μ_s observed below Q_{crit} was that it was likely to have been the result of differences in bulk and/or surface concentrations of SDS. Such differences would have affected the rates of adsorption/desorption of SDS as well as the compressibility of the interface at given liquid shear rates. Indeed, the effect of varying bulk concentrations on the compressibility of SDS interfaces has been directly observed in experimental work by Vogel[45]. In order to obtain an approximation of how SDS concentrations may have varied for different PB lengths, the average moles of surfactant contained in the liquid volume of each full-length PB profile was compared to the average PB interfacial area over the same length. This was done using Equation (4.12), producing a value for the maximum average available moles of SDS to populate an average unit area of interface, Γ_{max}. Here the initial bulk concentration of SDS, $C_{wt\%}$, was 0.5 for all solutions, and the molar mass of SDS was[46] M = 288.38gmol^{-1}. It is important to note that interfacial area and volume calculations were based on ideal PB cross-sections with negligible film thickness[12].

$$\Gamma_{max} \approx \frac{cR^2 l_1}{\pi R l_1} \frac{C_{wt\%}\rho}{100M} \tag{4.12}$$

The results of Equation (4.12) are plotted in Figure 4.12, and show a marked difference between values of Γ_{max} for the different PB lengths. This difference was approximately independent of the liquid shear rates, giving average values of 3.56mol/cm^2, 2.90mol/cm^2 and 2.37mol/cm^2, for $l_1 \approx$ 8.0mm, 15.0mm and 27.5mm respectively.

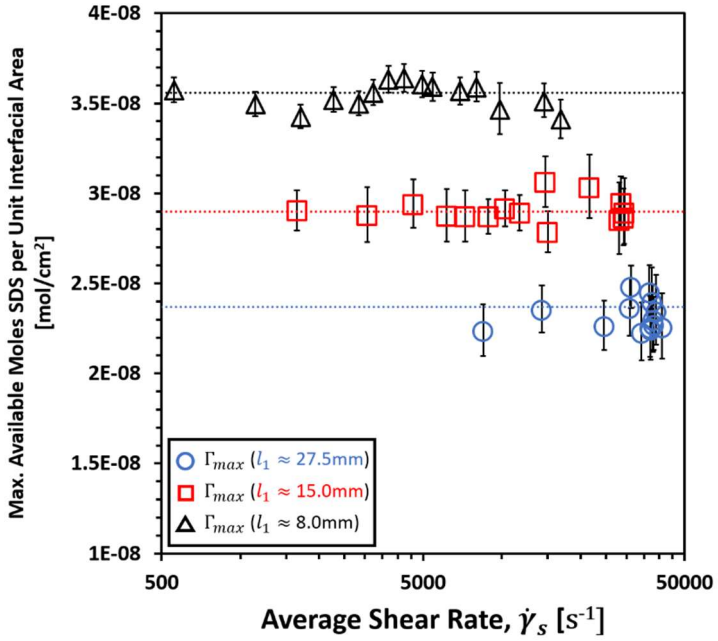

Figure 4.12. Average Maximum Available moles of SDS per Unit Interfacial Area, Γ_{max}, vs. Average Shear Rate, $\dot{\gamma}_s$, for 0.50wt% SDS solution with PB lengths $l_1 \approx$ 27.5mm, $l_1 \approx$ 15.0mm and $l_1 \approx$ 8.0mm. Dotted lines indicate average values of Γ_{max} for corresponding coloured data points.

The results of Figure 4.12 clearly show that an average variation in either the bulk or surface concentration of SDS could have occurred as a result of varying PB length. The reduction in concentration with increasing l_1 fits well with the observed trends in μ_s and the equilibrium cross sectional area. A lower initial surfactant population at the interface would have reduced the interfacial area due to the increase in the surface free energy, therefore increasing the liquid shear rates at given liquid flow rates according to Equation (4.10). Furthermore, one would expect a reduced μ_s for a lower surfactant population at the interface, due to the increased freedom of individual surfactant molecules. During compression experiments of SDS interfaces, Vogel[45] observed that the reduction in bulk concentration of SDS solutions resulted in a reduction in the compressibility of the interface. This would have served to

reduce the variation in μ_s at lower SDS concentrations, in agreement with the results shown here. It is important to note that these findings serve as an indication of possible factors that could lead to variations in surface viscosity with liquid shear rate, rather than a comprehensive answer. In order to probe this further, more detailed studies will be required that investigate variations in PB surface tension with liquid flow rates and the role played by rates of surfactant adsorption/desorption.

4.4 Conclusions

In this study, a novel technique is proposed for studying liquid flow through an isolated Plateau border of foam terminating in a geometrically 'ideal' node. The high resolution of the imaging achieved, combined with the flexibility of the setup to vary both liquid flow rate and the length of the PB, have proven capable of exploring a broad range of experimental conditions not seen in previous work.

An unexpected outcome of this study was the appearance of a clear distortion in the PB profiles that marked a sudden transition from the anticipated PB relaxation to a gradual PB expansion that transitioned smoothly into the node. These 'swelling regions' were found to be both PB length dependent and flow rate dependent after a critical flow rate, Q_{crit}. After Q_{crit}, swelling regions propagated discrete distances, Z_{swell}, along the PB, thus determining whether the PB profiles were dominated by relaxation or expansion. While previous work was found to have observed profiles dominated by either expansion or relaxation, this marks the first instance where this dominance could be precisely controlled. As conditions approached those of conventional foam drainage (i.e. PB lengths less than 10mm and flow rates less than 100µl/min), PB profiles were increasingly dominated by expansion into the node. The variable

of PB length is therefore deemed an important consideration when selecting relevant theory to describe the evolution of PB profiles. A further study of this region is proposed, wherein theory describing both PB relaxation and PB expansion is applied to the profiles studied here. A successful theoretical description of both regions should be able to describe the geometric evolution of their profiles, while predicting the appearance of the swelling regions at varying PB lengths and liquid flow rates. As the theory discussed here was relevant only to cases of PB relaxation, the subsequent analysis of measured PB profiles was therefore limited to the relaxation regions of these profiles.

Theory describing ideal PB relaxation agreed well with measured PB profiles, producing equilibrium cross-sectional areas, S_e, that could then be accurately interpreted using idealised 'infinite' PB theory. The values of S_e obtained here were shown to be consistently lower than the minimum cross-sectional areas for similar systems in previous studies[9,10], suggesting that direct measurement of minimum PB cross-sectional areas provides a poor indication of the equilibrium PB geometry. In turn, it was shown that inaccurate measurements of the equilibrium PB geometry would have resulted in artificially high measurements of the surface shear viscosity when applying idealised PB theory. It is also thought that the PB-only nature of previous setups may have influenced measurements, requiring a more direct investigation of the limits imposed on the PB by the node geometry.

The magnitudes of the apparent surface shear viscosity, μ_s, and its dimensionless equivalent, the apparent Boussinesq number, B_0, agreed well with values from the most precise existing measurements of true surface shear viscosities of SDS interfaces in the literature[17], exceeding the measurement sensitivity by approximately three orders of magnitude. Values of μ_s were

in the range 10^{-8} g/s $< \mu_s <$ 10^{-4} g/s corresponding to PB lengths within the range 27.5mm$\gtrsim l_1 \gtrsim$8.0mm respectively, while corresponding values of B_0 were in the range $10^{-4} < B_0 <$ 10^{-3}. The high sensitivity of the measurements here were able to detect a PB length dependence and flow rate dependence of μ_s has not been measured in previous studies. While a full numerical analysis of these effects was beyond the scope of the present study, a partial numerical and qualitative analysis is provided that indicates likely causes for the observed dependencies.

The apparent shear thinning behaviour of the PB interface is likely to have been the effect of variations in the surface concentration of SDS, which could have resulted in an increasing role played by Marangoni forces, which were predicted numerically[36] for virtually inviscid interfaces such as those described here. Marangoni forces were predicted to have increased with the liquid shear rate.

PB length dependence of μ_s has been attributed to differences in the bulk and interfacial concentrations of SDS that occurred at the different PB lengths. The average available moles of SDS in the bulk liquid per unit area of interface for the different PB lengths was measured to have decreased with increasing l_1. This decrease was roughly independent of liquid shear rate, scaling with factors of 1.00, 0.82 and 0.67 for l_1 = 8.0mm, 15.0mm and 27.5mm respectively. The variations in the bulk and surface concentrations of SDS are hypothesised to have resulted in changes to the compressibility of the PB interface, as observed in previous SDS compression experiments[45]. These observations indicated a lesser degree of interfacial compressibility for lower surfactant concentrations, which at the same time would be expected to lower initial values of μ_s, as was seen from the length dependence of μ_s here. The convergence of the length dependent μ_s data with increasing shear rates above Q_{crit},

suggested a limit in the compressibility of the interfaces, wherein a common interfacial structure was approached for all PB lengths.

The complex interactions of the forces and geometries described here represent a significant challenge for the application of a full numerical analysis. Indeed, further work is still required in order to untangle these effects at the level of simple planar interfaces[36]. In order to better understand the contributions of the factors discussed, it is proposed that further studies of soluble surfactant systems, with known variations in chemical and physical characteristics, be undertaken. Variations in bulk concentrations and viscosities, for example, would be expected to elicit changes in the measured μ_s that could then be used to better understand the effects proposed above.

Overall, this study has shown that the present technique represents a potential milestone in measurement sensitivity for the interfacial responses of soluble surfactants to applied shear. Furthermore, it directly relates these values to flows through ideal foam channels, a key aspect of macroscopic foam drainage models where the significance of μ_s is often contested for soluble surfactants[17]. It is hoped that the further exploration of soluble surfactants in this manner will yield insights into the dynamic nature of these foam interfaces, ultimately improving the current understanding of these complex systems.

4.5 References

1 I. Cantat; S. Cohen-Addad; F. Elias; F. Graner; R. Höhler; O. Pitois; F. Rouyer; A. Saint-Jalmes; S. Cox, *Foams: Structure and Dynamics*; Oxford University Press: New York, **2013**.

2 J. Wang; A. V. Nguyen; S. Farrokhpay, A Critical Review of the Growth, Drainage and Collapse of Foams, *Advances in Colloid and Interface Science* **2016**, *228*, 55-70.

3 R. J. Pugh, *Bubble and Foam Chemistry*; Cambridge University Press: Cambridge, United Kingdom, **2016**.

4 R. A. Leonard; R. Lemlich, A Study of Interstitial Liquid Flow in Foam. Part I. Theoretical Model and Application to Foam Fractionation, *AIChE Journal* **1965**, *11*, 18-25.

5 A. V. Nguyen, Liquid Drainage in Single Plateau Borders of Foam, *Journal of Colloid and Interface Science* **2002**, *249*, 194-199.

6 S. A. Koehler; S. Hilgenfeldt; H. A. Stone, Foam Drainage on the Microscale: I. modeling Flow through Single Plateau Borders, *Journal of Colloid and Interface Science* **2004a**, *276*, 420-438.

7 S. A. Koehler; S. Hilgenfeldt; E. R. Weeks; H. A. Stone, Foam Drainage on the Microscale Ii. Imaging Flow through Single Plateau Borders, *Journal of Colloid and Interface Science* **2004b**, *276*, 439-449.

8 M. In Het Panhuis; S. Hutzler; D. Weaire; R. Phelan, New Variations on the Soap Film Experiments of Plateau I. Experiments under Forced Drainage, *Philosophical Magazine Part B* **1998**, *78*, 1-12.

9 O. Pitois; C. Fritz; M. Vignes-Adler, Hydrodynamic Resistance of a Single Foam Channel, *Colloids and Surfaces A: Physicochemical and Engineering Aspects* **2005b**, *261*, 109-114.

10 O. Pitois; C. Fritz; M. Vignes-Adler, Liquid Drainage through Aqueous Foam: Study of the Flow on the Bubble Scale, *Journal of Colloid and Interface Science* **2005a**, *282*, 458-465.

11 O. Pitois; N. Louvet; E. Lorenceau; F. Rouyer, Node Contribution to the Permeability of Liquid Foams, *Journal of Colloid and Interface Science* **2008**, *322*, 675-677.

12 F. Elias; E. Janiaud; J.-C. Bacri; B. Andreotti, Elasticity of a Soap Film Junction, *Physics of Fluids* **2014**, *26*, 037101.

13 A. Saint-Jalmes, Physical Chemistry in Foam Drainage and Coarsening, *Soft Matter* **2006**, *2*, 836-849.

14 M. A. Bos; T. van Vliet, Interfacial Rheological Properties of Adsorbed Protein Layers and Surfactants: A Review, *Advances in Colloid and Interface Science* **2001**, *91*, 437-471.

15 F. C. Goodrich; L. H. Allen; A. Poskanzer, A New Surface Viscometer of High Sensitivity. I. Theory, *Journal of Colloid and Interface Science* **1975**, *52*, 201-212.

16 M. Sacchetti; H. Yu; G. Zografi, *A Canal Surface Viscometer for the in-Plane Steady Shear Viscosity of Monolayers at the Air/Water Interface*, **1993**; Vol. 64, p 1941-1946.

17 Z. A. Zell; A. Nowbahar; V. Mansard; L. G. Leal; S. S. Deshmukh; J. M. Mecca; C. J. Tucker; T. M. Squires, Surface Shear Inviscidity of Soluble Surfactants, *Proceedings of the National Academy of Sciences* **2014**, *111*, 3677-3682.

18 G. G. Fuller; J. Vermant, Complex Fluid-Fluid Interfaces: Rheology and Structure, *Annual Review of Chemical and Biomolecular Engineering* **2012**, *3*, 519-543.

19 F. Rouyer; E. Lorenceau; O. Pitois, Film Junction Effect on Foam Drainage, *Colloids and Surfaces A: Physicochemical and Engineering Aspects* **2008**, *324*, 234-236.

20 B. Scheid; J. Delacotte; B. Dollet; E. Rio; F. Restagno; E. A. v. Nierop; I. Cantat; D. Langevin; H. A. Stone, The Role of Surface Rheology in Liquid Film Formation, *EPL (Europhysics Letters)* **2010**, *90*, 24002.

21 S. I. Karakashev; E. D. Manev, Hydrodynamics of Thin Liquid Films: Retrospective and Perspectives, *Adv Colloid Interface Sci* **2015**, *222*, 398-412.

22 A. Cohen; N. Fraysse; C. Raufaste, Drop Coalescence and Liquid Flow in a Single Plateau Border, *Physical Review E - Statistical, Nonlinear, and Soft Matter Physics* **2015**, *91*.

23 M. Kostoglou; E. Georgiou; T. D. Karapantsios, A New Device for Assessing Film Stability in Foams: Experiment and Theory, *Colloids and Surfaces A: Physicochemical and Engineering Aspects* **2011**, *382*, 64-73.

24 Y. Wang; J. Ge; G. Zhang; P. Jiang; K. Song; W. Zhang, Effect of Surface Dilatational Modulus on Foam Flow in a Porous Medium, *Tenside, Surfactants, Detergents* **2017**, *54*, 327-333.

25 A. Lazidis; L. Parizotto; F. Spyropoulos; I. Norton, *Microstructural Design of Aerated Food Systems by Soft-Solid Materials*, **2017**; Vol. 73, p 110-119.

26 D. Weaire; S. Hutzler, *The Physics of Foams*; Oxford University Press: New York, **1999**.

27 A. Saint-Jalmes; Y. Zhang; D. Langevin, Quantitative Description of Foam Drainage: Transitions with Surface Mobility, *Eur. Phys. J. E* **2004**, *15*, 53-60.

28 A. Anazadehsayed; N. Rezaee; J. Naser, Numerical Modelling of Flow through Foam's Node, *Journal of Colloid and Interface Science* **2017**, *504*, 485-491.

29 R. A. Leonard; R. Lemlich, A Study of Interstitial Liquid Flow in Foam. Part Ii. Experimental Verification and Observations, *AIChE Journal* **1965**, *11*, 25-29.

30 S. J. Neethling; H. T. Lee; J. J. Cilliers, A Foam Drainage Equation Generalized for All Liquid Contents, *Journal of Physics: Condensed Matter* **2002**, *14*, 331.

31 S. A. Koehler; S. Hilgenfeldt; H. A. Stone, A Generalized View of Foam Drainage: Experiment and Theory, *Langmuir* **2000**, *16*, 6327-6341.

32 V. Carrier; S. Destouesse; A. Colin, Foam Drainage: A Film Contribution?, *Physical Review E* **2002**, *65*, 061404.

33 M. Sharifi; M. Fathy; M. T. Mahmoudi In *A Classified and Comparative Study of Edge Detection Algorithms*, Proceedings. International Conference on Information Technology: Coding and Computing, 8-10 April 2002; 2002; pp 117-120.

34 A. Cifuentes; J. L. Bernal; J. C. Diez-Masa, Determination of Critical Micelle Concentration Values Using Capillary Electrophoresis Instrumentation, *Analytical Chemistry* **1997**, *69*, 4271-4274.

35 K. Koczó; G. Rácz, Flow in a Plateau Border, *Colloids and Surfaces* **1987**, *22*, 95-96.

36 G. J. Elfring; L. G. Leal; T. M. Squires, Surface Viscosity and Marangoni Stresses at Surfactant Laden Interfaces, *Journal of Fluid Mechanics* **2016**, *792*, 712-739.

37 K. Kinoshita; E. Parra; D. Needham, Adsorption of Ionic Surfactants at Microscopic Air-Water Interfaces Using the Micropipette Interfacial Area-Expansion Method: Measurement of the Diffusion Coefficient and Renormalization of the Mean Ionic Activity for Sds, *Journal of Colloid and Interface Science* **2017**, *504*, 765-779.

38 S. A. K. Jeelani; S. Hartland, Effect of Interfacial Mobility on Thin Film Drainage, *Journal of Colloid and Interface Science* **1994**, *164*, 296-308.

39 V. B. Fainerman; R. Miller, Surface Tension Isotherms for Surfactant Adsorption Layers Including Surface Aggregation, *Langmuir* **1996**, *12*, 6011-6014.

40 P. Yazhgur. Flows in Foams : The Role of Particles, Interfaces and Slowing Down in Microgravity. Université Paris-Saclay, 2015.

41 H. Vatanparast; F. Shahabi; A. Bahramian; A. Javadi; R. Miller, The Role of Electrostatic Repulsion on Increasing Surface Activity of Anionic Surfactants in the Presence of Hydrophilic Silica Nanoparticles, *Scientific Reports* **2018**, *8*, 7251.

42 J.-C. Gimel; W. Brown, *A Light Scattering Investigation of the Sodium Dodecyl Sulfate-Lysozyme System*, **1996**; Vol. 104, p 8112-8117.

43 F. M. Menger; S. A. A. Rizvi, Relationship between Surface Tension and Surface Coverage, *Langmuir* **2011**, *27*, 13975-13977.

44 A. Casandra; M.-C. Chung; B. A. Noskov; S.-Y. Lin, Adsorption Kinetics of Sodium Dodecyl Sulfate on Perturbed Air-Water Interfaces, *Colloids and Surfaces A: Physicochemical and Engineering Aspects* **2017**, *518*, 241-248.

45 T. J. Vogel. Dynamic Behavior of Self-Assembled Langmuir Films Composed of Soluble Surfactants and Insoluble Amphiphiles. The Ohio State University, 2011.

46 PubChem https://pubchem.ncbi.nlm.nih.gov/compound/3423265. (accessed 20 Dec, 2018).

Chapter 5

Surface Rheological Measurements of Isolated Food Foam Systems.

Published as: C. Clarke; F. Spyropoulos; I. T. Norton, Surface Rheological Measurements of Isolated Food Foam Systems, *Physics of Fluids* **2019**, *31*, 092002.

5.0 Abstract

Liquid foams represent a key component to a vast range of food industry products, from ice creams to the crema on coffee. Longevity of these foams is a highly desireable attribute, however in order for foam stability to be effectively controlled, a better understanding of the interdependence of the bulk liquid and air-liquid interfacial rheologies is required. This study follows an increasing trend in experimental investigations made of isolated foam structures at the microscale, where the bulk and surface dynamics of a single foam liquid channel can be accurately assessed. Isolated foam channels with adjoining nodes were studied for aqueous solutions of four food grade surfactants. Existing observations of distortions to Sodium Dodecyl Sulfate (SDS) channel geometries were confirmed for solutions of Tween 20 (T20) and Tween 80 (T80), and were well described by the theory presented here. Moreover, previously unseen distortions to liquid channels were observed for polymeric surfactant systems (hydroxypropyl methylcellulose (HPMC) and hydrolysed pea protein blend (HPP)), which were proposed to result from their high surface viscosities. The apparent surface viscosities, μ_s, of surfactants tested here ranged from high (10 g/s$< \mu_s <$10^{-3} g/s) for polymeric surfactants, to very low (10^{-10} g/s$< \mu_s <$10^{-8} g/s) for Tweens, clearly demarking the regimes of viscous and inertial dominant flows respectively. It is recommended that further work seeks to investigate the finding of a strong correlation between μ_s and channel surface tension, γ, for soluble surfactant systems, which could explain the apparent non-Newtonian values of μ_s that were consistently measured here.

5.1 Introduction

5.1.1 Background

The phenomenon of foam drainage is a complex multi-scale process that ultimately leads to the collapse of foams due to film rupture and bubble coalescence[1]. Foam longevity is a common problem in the food industry, where the instability of liquid foam products such as whipped toppings, ice cream, mousses and confectionary fillings can dramatically decrease their potential shelf life[2].

As a key mechanism underlying foam collapse, arresting liquid drainage through the network of channels or Plateau borders (PBs) between bubbles is often a key focus in foam formulation. In many food products (and indeed non-food products) this is still largely addressed by increasing the bulk liquid viscosity using a trial and error approach[3]. The ultimate goal in these instances is to create a yield stress of the bulk liquid that cannot be reached by the action of gravitational forces alone, therefore halting liquid flow altogether.

More recently, the drive to improve our understanding on food ingredients has led to an increasing number of innovations in formulation and processing that target drainage via other means. Examples range from the blocking of liquid channels using novel particle systems[4], to creating more robust interfacial structures that increase the channels' hydrodynamic resistance with varying combinations of surface active particles, low molecular weight surfactants (LMWS) and polymeric surfactant systems[2,3].

As the development of novel food microstructures and foam formulations continues, the need to better understand the role played by the air-liquid interface in foam drainage is becoming

increasingly apparent. Different surfactants dramatically alter the physical properties of the interface, whose surface rheology and subsequent impact on liquid flow are still extensively studied in both liquid films and foam channels alike.[5-12]

Theoretical modelling of foam channels has presented a significant challenge to researchers[13]. The already complex geometries within the foam microstructure undergo expansion and distortion, with these phenomena determined, to an extent, by the rheology of the bulk liquid and the gas-liquid interface, which themselves are dependent on the liquid flow rate[14]. In addition, the body of experimental work studying these isolated channels is extremely limited[15], making it difficult to clearly confirm or refute theoretical predictions. When one considers that many studies of macroscopic foam systems are based on such microscale theory, it is clear that more microscale evidence is required[16], in terms of both quantity and accuracy.

The most recent experimental studies of isolated PB and PB-Node geometries have proved to be a step forward with respect to understanding channel surface rheology. By creating spatially 'ideal' arrangements of foam channels within bespoke frames, researchers have been able to probe specific physical and chemical variables thought to influence the nature of the interface[8,9,15,17-21]. Such in-situ measurements of channel surface rheology are critical, as they provide unparalleled control and measurement consistency.

So far, the study of these isolated systems has been limited to simple LMWS systems such as Tetradecyltrimethylammonium Bromide (TTAB)[17-19] and Sodium Dodecyl Sulfate (SDS)[8,18,19]. Variations in interfacial rheology have been introduced by small additions of dodecanol (DOH), which acts to dramatically increase the surface viscosity of the interface, while changes to the

bulk rheology has been undertaken by the addition of glycerol. Most recently, the work by Clarke *et al.*[8] using an isolated PB-Node system with pure SDS solution, has yielded surprising findings regarding previously unobserved changes to fundamental liquid channel geometries during forced liquid flow. In addition, these results appear to confirm what are purported as the most accurate surface viscosity measurements of SDS to date[22], predicting the air-liquid interface of SDS and other soluble LMWS systems to be so low as to be considered virtually inviscid.

The surface shear viscosity, relates the shear force per unit length of interface to an applied shear rate[23], which in PB systems arises from liquid flow adjacent to the interface. Higher values of surface viscosity result in greater dissipation of liquid flow at the PB boundaries, resulting in increasingly Poiseuille-like flow velocity profiles[24]. The contrast between low and high surface viscosity is thought to be responsible for the two macroscopic regimes of *node-dominated* and *channel-dominated* foam drainage respectively, which describe whether the bulk of flow dissipation is thought to occur at the nodes or within the PBs themselves [8,18,25]. The extremely low values of surface viscosity found by Zell *et al.*[22] and Clarke *et al.*[8] for soluble LMWS systems therefore suggests that flow dissipation occurs primarily in the nodes in these cases, with surface viscosity having little impact on macroscopic foam drainage.

As the theory used by Clarke *et al.*[8] was unable to describe the full extent of the unusual PB geometries identified, and based only on results from SDS solutions, the present study aims to further probe this promising measurement technique. In order to do this, the current work assesses a range of surfactant solutions that are anticipated to display a wide range of surface viscosities. In order to maximise the relevance of these results to the food industry,

formulations investigated here reflect the diversity of food grade surfactants ranging from soluble LMWS systems (similar to SDS) to polymeric surfactant systems such as proteins and long chain polysaccharides. The theory used by Clarke *et al.*[8] has been assessed and potentially revised if it is to account for the unusual PB geometries that were previously observed for SDS.

5.1.2 Theory

5.1.2.1 The PB Relaxation Equation

In the previous study by Clarke*, et al.*[8], a simplified solution to the standard drainage theory (Equation (5.1))[16] was fitted to vertical geometric PB profiles measured for 0.5wt% SDS solution at a range of liquid flow rates, Q, and PB lengths, l_1. This solution is shown in Equation (5.2), the derivation of which is laid out by Elias*, et al.*[9] and describes the relaxation of the PB radius between the limits of an initial radius, R_0, at the vertical height $Z = 0$, and an equilibrium radius, R_e, over a vertical distance set by the relaxation length, L.

$$\frac{dR}{dZ} = \frac{cD\nu Q - gc^2R^4}{\left(\frac{2IQ^2}{R}\right) - \left(\frac{c^2R^2\gamma}{\rho}\right)} \tag{5.1}$$

$$R = R_e + (R_0 - R_e)e^{-Z/L} \tag{5.2}$$

The equilibrium radius is defined by Equation (5.3), describing the lower limit of the PB radius, gravitational forces are balanced by viscous dissipation. Here c is a geometric constant (~ 0.161), ν is the kinematic viscosity of the solution, g is the acceleration due to gravity and D is the viscous flow parameter:

$$R_e = \left(\frac{D\nu Q}{cg}\right)^{1/4} \tag{5.3}$$

The relaxation length, L, is described by Equation (5.4) and includes the effects of surface tension, γ, solution density, ρ, and inertial contributions to liquid flow via the inertial flow parameter, I, whose role is described in more detail below.

$$L = \frac{IQ^2}{2c^2 g {R_e}^4} - \frac{\gamma}{4\rho g R_e} \tag{5.4}$$

As a simplified solution to Equation (5.1), Equation (5.2) was easily applied to measured PB geometric profiles using automated fitting methods. The obtained values of the fitting parameters R_e and L were then used to calculate the physical variables D and I from Equation (5.2) and (5.3) respectively, using pre-measured values of ν, ρ, Q and γ. Here it was approximated that the surface tension, γ, was equal to its equilibrium value as measured by Wilhelmy Plate measurements ($\gamma = \gamma_e$) and also independent of liquid flow rate and PB length. However, the results of Clarke's study suggested that this approximation was unlikely to be accurate, and is especially unlikely to be the case where rates of surfactant adsorption are slow.

The dimensionless parameters D and I ultimately describe the shapes of the PB velocity profiles according to Equations (4.6) and (4.7), where individual flow velocity components, u, across a given PB cross section give the average flow velocity, $\bar{u} = U$.[9] Flow velocity profiles lie between the two extremes of Poiseuille flow and Plug flow, which are described by $D \rightarrow 312$, $I > 1$, and $D \rightarrow 0$, $I \rightarrow 1$, respectively[9]. Low molecular weight surfactants such as SDS and Polysorbates/Tweens are generally expected to fall into the latter category, as their extremely high mobility at the air/water interface[22] results in minimal viscous dissipation of liquid flow at the PB boundaries.

$$D = -R^2\overline{\Delta u}/\bar{u} \tag{5.5}$$

$$I = \overline{u^2}/\bar{u}^2 \tag{5.6}$$

A more detailed derivation of Equation (5.1), based on that of Elias*, et al.*[9], is given in Appendix B, where the origins of Equations (5.5) and (5.6) become apparent.

Flow velocity profiles lie between the two extremes of Poiseuille flow and Plug flow, which are described by $D \to 312,\ I > 1$, and $D \to 0,\ I \to 1$, respectively[9]. Low molecular weight surfactants such as SDS and Polysorbates/Tweens are generally expected to fall into the latter category, as their extremely high mobility at the air/water interface[22] results in minimal viscous dissipation of liquid flow at the PB boundaries.

The values for the viscous flow parameter, D, were converted into values for the dimensionless Boussinesq Number, B_0, and its dimensional counterpart, the surface shear viscosity, μ_s, using the phenomenological expression proposed by Nguyen[26] (Equation (5.7) and the definition of the surface shear viscosity given by Equation (5.8). It should be noted that Equation (5.7) is only valid for a straight, vertical PB, and therefore these calculations were applied only to the equilibrium case $R = R_e$.

$$D^{-1} = c\left[0.02 + \frac{0.0655{B_0}^{-0.5}}{0.209 + {}_0{}^{0.628}}\right] \tag{5.7}$$

$$\mu_s = B_0 \mu R \qquad (\text{with } R = R_e) \tag{5.8}$$

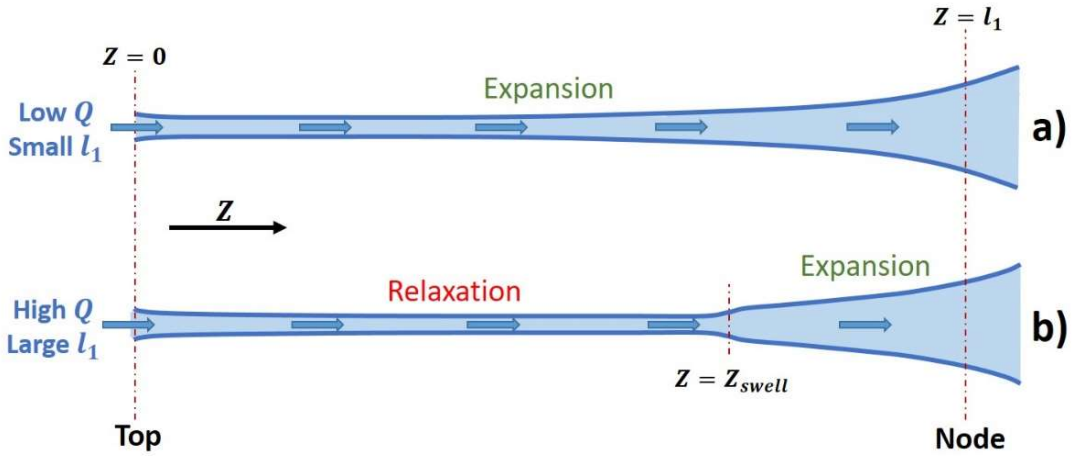

Figure 5.1. Visualisation of PB profiles of length, l_1, and liquid flow rate, Q. a) Low Q, small l_1 resulted in almost complete expansion profiles. b) Increasing Q and l_1 exhibited both relaxation and expansion with increasingly prominent transition distortions at height $Z = Z_{swell}$ [8].

Despite Equation (5.2) being a good description of PB geometric profiles exhibiting relaxation, Clarke *et al.*[8] found that increasing proportions of the profile were replaced with expansion into the adjoining node at decreasing liquid flow rates and PB lengths (see Figure 5.1). As such, these expansion regions were excluded, resulting in an incomplete analysis of the PB profiles. Furthermore, the unusual nature of the transitions between relaxation and expansion at $Z = Z_{swell}$ and their PB length and flow rate dependence requires explanation, as a potential change in the physical parameters of the system might be suggested.

5.1.2.2 The Relaxation-Expansion PB Profile Equation

In order to address the inability of Equation (5.2) to describe PB expansion, a full geometric profile solution was derived from Equation (5.1). The variables: D, ν, Q, g, c, I, γ and ρ in Equation (5.1) were once again substituted for R_e and L using Equation (5.3) and (5.4), with

an additional term, the capillary length, $L_c = \sqrt{\gamma/\rho\, g}$. Equation (5.9) sets up the solution to this revised form of Equation (5.1) as an integral with the limits of the initial radius, R_0, at $Z = 0$ to some radius R at a distance Z from $Z = 0$. Equation (5.9) was solved using the computer algebra system, Maxima (VA Software, USA), yielding Equation (5.10); a complete geometric PB profile solution.

$$\int_0^Z dZ = \int_{R_0}^{R} \left\{ \frac{{L_c}^2}{R(R_e+R)} + \frac{{L_c}^2 R_e}{({R_e}^2+R^2)(R_e+R)} + \frac{4L{R_e}^4}{R({R_e}^4-R^4)} \right\} \cdot dR \tag{5.9}$$

$$Z = L\, ln\left[\frac{R^4({R_0}^4-{R_e}^4)}{{R_0}^4({R^4}-{R_e}^4)}\right] + \frac{{L_c}^2}{4R_e}\left\{ ln\left[\frac{R^4(R_0+R_e)^2({R_0}^2+{R_e}^2)}{{R_0}^4(R+R_e)^2({R^2}+{R_e}^2)}\right] + 2\, tan^{-1}\left[\frac{R-R_0}{R_e(1+RR_0/{R_e}^2)}\right]\right\} \tag{5.10}$$

Figure 5.2 shows the form taken by Equation (5.10) for a set of physical parameters that are representative of the systems in this study. It can be seen that there are two potential solutions for R at any given height, Z, for the same set of physical variables, with the exception of $Z = 0$. These solutions for R either follow a pattern of relaxation, which is closely approximated by the Elias' relaxation Equation (5.2), ***OR*** expansion. These solutions join at a minimum occurring at $Z = 0$, $R = R_0$; resulting in the initial condition given by Equation (5.11):

$$R_0 = \left(\frac{2\rho I Q^2}{c^2\gamma}\right)^{1/3} \tag{5.11}$$

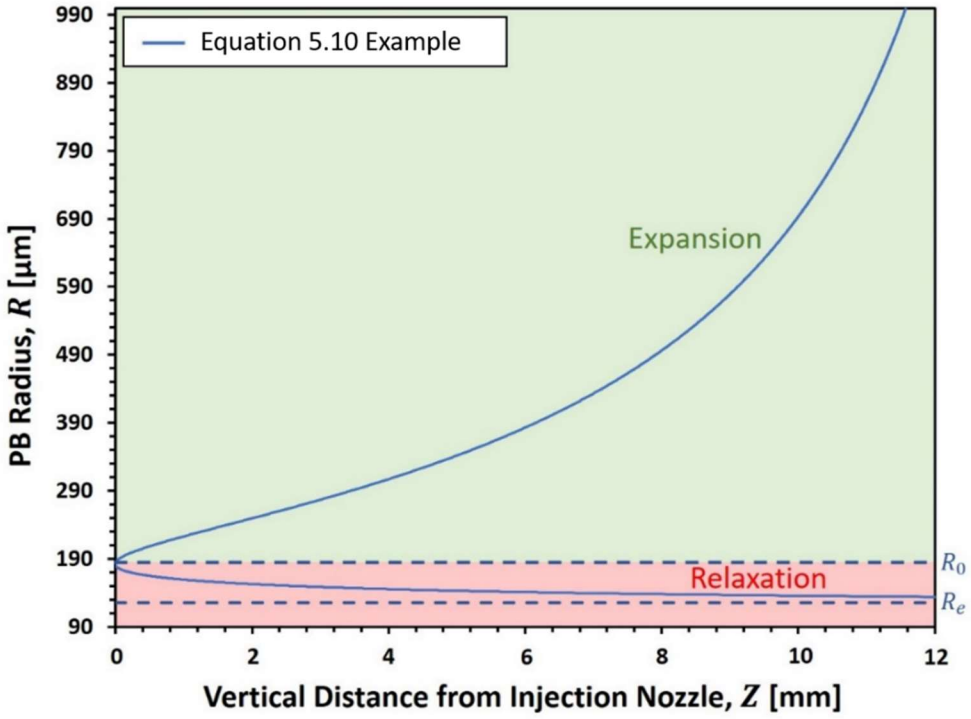

Figure 5.2. Equation (5.10) example, demonstrating simultaneous relaxation and expansion solutions. Solutions meet in the minimum occurring at $R = R_0$, $Z = 0$, while the relaxation solution tends to $R = R_e$ as $Z \to \infty$.

The initial condition set by Equation (5.11) is striking, as it shows a dependence of R_0 on bulk and surface liquid properties, as well as liquid flow rate. When one considers the case of PB expansion into an adjoining node, both the rate of expansion (dR/dZ) and the initial radius from which this expansion can commence are shown to be dependent on the bulk and surface parameters of the liquid (Equation (5.1) and (5.11)). Furthermore, the final radius of this expansion must coincide with the initial radius of the adjoining node, R_{no}, at a height $Z = l_1$ (see Figure 5.3). In a forced flow system where the value of l_1 is primarily set by the length of the frame geometry producing the PB-node system, there are limited ways in which the above conditions can be satisfied. The first would require a significant change in the physical

parameters I, D and γ as the PB transitions from the relaxation to the expansion state. The second would require an offset of the zero height of the expansion solution, Z_T, allowing I, D and γ to remain the same as for the relaxation solution, but providing a smooth transition into the node at R_{no} (see Figure 5.3). The third would require a combination of both these effects, wherein changes to I, D and γ are minimised by the zero offset of the expansion solution.

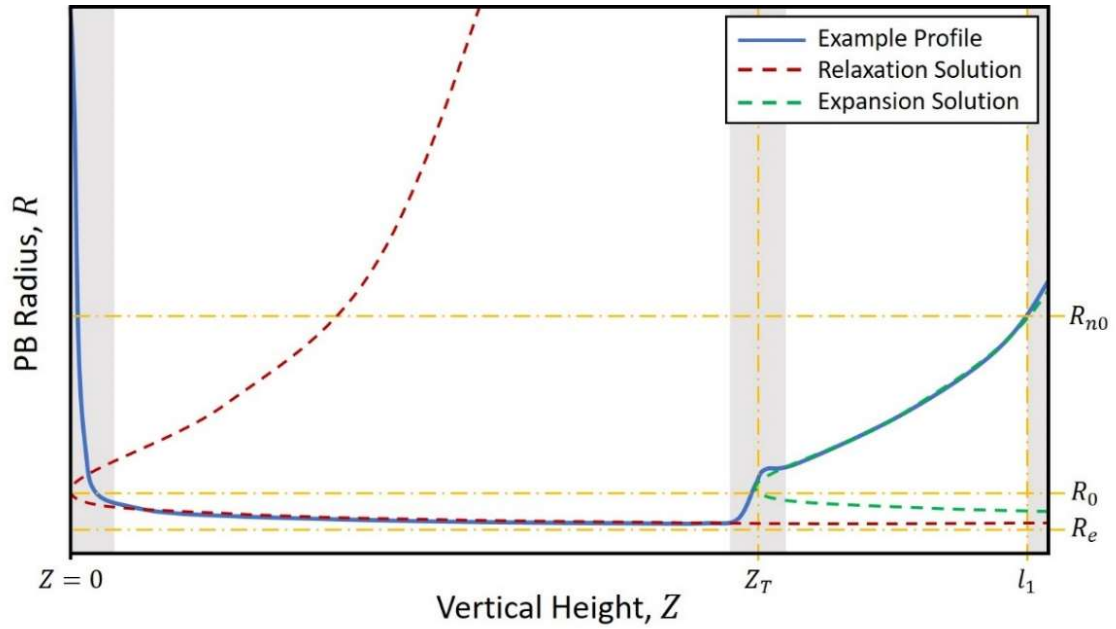

Figure 5.3. Relaxation (red) and expansion (green) solutions against an example PB profile (blue), with key coordinates marked (yellow). Zero or small variations in the physical parameters I, D and γ between relaxation and expansion solutions require a zero offset Z_T. Grey regions represent parts of the profile unaccounted for in the current theory, namely: The distortion of caused by the PB attachment to the frame, the transition from relaxation to expansion solutions, and the node.

A revised form of Equation (5.10) is given by Equation (5.12) wherein the zero offset, Z_T, is incorporated. It is important to note that this amendment is only necessary in the context of a fixed point of reference for $Z = 0$.

$$Z - Z_T = L\,ln\left[\frac{R^4\left({R_0}^4-{R_e}^4\right)}{{R_0}^4\left(R^4-{R_e}^4\right)}\right] + \frac{{L_c}^2}{4R_e}\left\{ln\left[\frac{R^4(R_0+R_e)^2\left({R_0}^2+{R_e}^2\right)}{{R_0}^4(R+R_e)^2\left(R^2+{R_e}^2\right)}\right] + 2\,tan^{-1}\left[\frac{R-R_0}{R_e\left(1+RR_0/{R_e}^2\right)}\right]\right\} \quad (5.12)$$

5.2 Experimental

5.2.1 Preparation of Solutions

Tween® 20 and Tween® 80 from Sigma-Aldrich (UK), Methocel™ F50 from The Dow Chemical Company (USA), and Hyfoama™ (pea) from Kerry (Ireland) were selected for investigation, due to their ability to quickly form stable films while representing stabilisation mechanisms dependent upon surface viscosities at opposite ends of the spectrum.

Tween 20 and Tween 80 represent two commonly used soluble surfactants in the food industry, where Tween 20 in particular is regularly used in foaming applications. The Gibbs-Marangoni stabilisation mechanism of these LMWS systems is reliant upon the high mobility of surfactant molecules at the interface, therefore yielding extremely low surface viscosities[22].

In contrast, the stabilisation mechanism of most polymeric surfactants is to form a more robust network through the cohesive interaction of adsorbed polymers at the interface, resulting in significantly higher values of surface viscosity[3]. Methocel™ F50 consists of the long chain polysaccharide Hydroxypropyl methylcellulose (HPMC), with controlled degrees of methoxyl and hydroxypropyl substitution improving its film forming ability. It is claimed to exhibit surface gelation at the air-liquid interface, with higher bulk concentrations leading to increased gel strength[27]. As such, this represents a potentially extreme case of a virtually immobile air-liquid interface, which would therefore be expected to yield very high values of surface shear viscosities. The surface active component of the Hyfoama™ used in this study

were pea protein hydrolysates (HPP), these having been found to exhibit far greater functionality than their native pea protein isolates[28]. Hyfoama™ has not been reported to exhibit surface gelation, and was therefore expected to yield lower values of surface shear viscosity than for Methocel™ F50.

Surfactants were weighed using a digital balance to an accuracy of three decimal places. Purified water (15.0 MΩ·cm) was weighed into borosilicate glass beakers and magnetically stirred at room temperature while surfactants were added. Stirring continued for a minimum of 30 minutes after all surfactant was visibly in solution in order to ensure full incorporation of surfactant and solution homogeneity. A minimum of 60 minutes stirring was used for HPMC preparation, as this was required to ensure its complete hydration.

5.2.2 Characterisation of Surfactant Solutions

Two solution concentrations of each surfactant were chosen for analysis, details of which can be found in Table 5.1. In the case of polymeric surfactants, initial concentrations were chosen based on the solutions' ability to reliably form stable films within the PB-Node Setup. These concentrations were subsequently doubled and trialled again for comparison. Concentrations of Tween 20 and Tween 80 were selected to be ∼10× and ∼20× the literature CMC values[29,30], as these would serve to test the assumption that constant equilibrium surface tension values can be assumed in PBs for surfactants well above their CMC concentrations (i.e. $\gamma \equiv \gamma_e$). To the knowledge of these authors, there is no instance of this assumption ever having been tested, most likely due to the difficulties in doing so. It is highly possible however that the variations in channel geometries and shears associated with different liquid flow rates could affect these values.

Bulk properties ρ and μ were measured in triplicate using a Krüss Processor® Tensiometer K100 (Krüss GmbH, Germany) with density hook attachment and silicon density standard, and a Malvern Kinexus® Pro rheometer (Malvern Panalytical, UK) with Double-Gap geometry respectively. Reference values for the solution surface tensions, γ, were measured in triplicate using a Krüss Processor® Tensiometer K100 (Krüss GmbH, Germany) with Wilhelmy Plate attachment. All property values were averaged with absolute errors of one standard deviation.

5.2.3 The PB-Node Setup

The isolated PB-Node setup used to create and observe the desired PB-Node geometries is well described in Chapter 3. This forced flow setup consisted of a closed 3-legged frame that could be submerged and withdrawn from surfactant solution to produce an ideal PB and node configuration (Figure 5.4). The selected frame geometry produced PB lengths of $l_1 \approx 25.5$ mm, as this maximised the amount of experimental data to fit to while still producing stable PB-Node systems. Backlit profiles of the PB-Node geometries were imaged and processed to allow fitting of Equation (5.12).

Controlled liquid flow rates, Q, were achieved by injecting surfactant solution directly into the upper PB at increments of 20 µl/min in the range 20 µl/min $\leq Q \leq$ 180 µl/min, therefore describing conventional drainage flow rates (0 µl/min $\leq Q \leq$ 100 µl/min) and beyond. By using this broad range of liquid flow rates, any flow rate dependent trends of fitting variables were expected to become more apparent. Once equilibrium was achieved at each flow rate, PB profile widths were acquired from images taken at increments along the full PB length, using an image processing technique developed in chapter 3. Image resolutions varied

between 1.5µm/Pixel to 10µm/Pixel depending upon the necessary magnification for given PB widths. These were used to calculate PB radii, R, for the full PB profiles, starting from $Z = 0$ at the injection nozzle to $Z \approx l_1$.

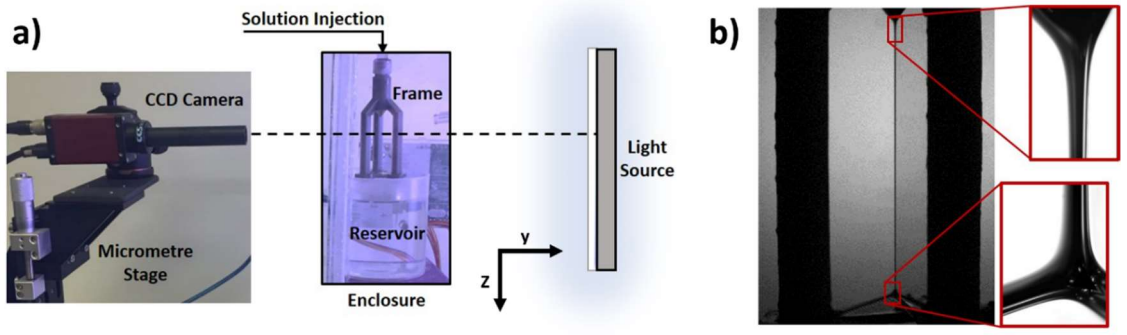

Figure 5.4. Imaging for analysis of PB-Node profiles. a) Optical Setup - A camera images the enclosed frame using a rear diffuse panel light to create shadow profile images. b) Low and high magnification images of a PB node profile, where highest magnification (red highlighted images) represents 1.5 µm per image pixel.

5.2.4 Model Fitting

The fitting parameters, R_e, I, γ and Z_T were used to fit Equation (5.12) to measured PB profiles, where Q was controlled and ν, ρ were directly measured from the liquid solutions (see below). While Chapter 4 previously assumed that constant γ, where $\gamma = \gamma_e$, could be applied for SDS solutions, these resulted in some values of I below their physical limit of 1 when fitting Equation (5.2). In this study, I was restricted to its physical lower limit of 1. As a result, the only means by which quality fits could be achieved was by allowing for variations in γ. The physical limits of γ were also put in place, such that $\gamma_e \leq \gamma \leq \gamma_0$ where γ_0 describes the surface tension of a pure water interface.

Utilising automated fitting methods in this study represented a significant technical challenge. This was due in part to the complexity of Equation (5.12), but also to a number of poorly characterised distortions and transitions in the PB profiles (see Figure 5.3). Ultimately, it was shown that manual fitting was consistently able to produce better quality fits to experimental data than automated methods at this stage.

The initial attempts to fit Equation (5.12) to PB profiles exhibiting simultaneous relaxation and expansion without the inclusion of a zero offset (i.e. $Z_T = 0$), were found to be completely unsuitable. In these instances, even vaguely appropriate fits required values for the surface tension to be higher than that of pure water, making them unfeasible as solutions. As such, it was assumed that in these cases $Z_T > 0$ for expansion solutions and that this would have served to minimise or remove variations in D, I and γ over the length of the PB at constant liquid flow rates. In order to assess whether this was the case, potential solutions were further limited such that the fitting variables R_e, I and γ were the same for both relaxation and expansion solutions at any given liquid flow rate.

5.2.5 Measurement of Relaxation-Expansion Transition Points

The distinctive transition regions between profile relaxation and expansion observed in section 4.3.2 became increasingly evident with increasing values of $l_1$and liquid flow rates, Q. These regions were estimated based on measured PB profiles, where the transition spanned the end of consistent PB relaxation behaviour to the beginning of consistent expansion behaviour (see Figure 5.5). No visible transition regions were recorded for PB profiles showing expansion only (i.e. $Z_T < 0$).

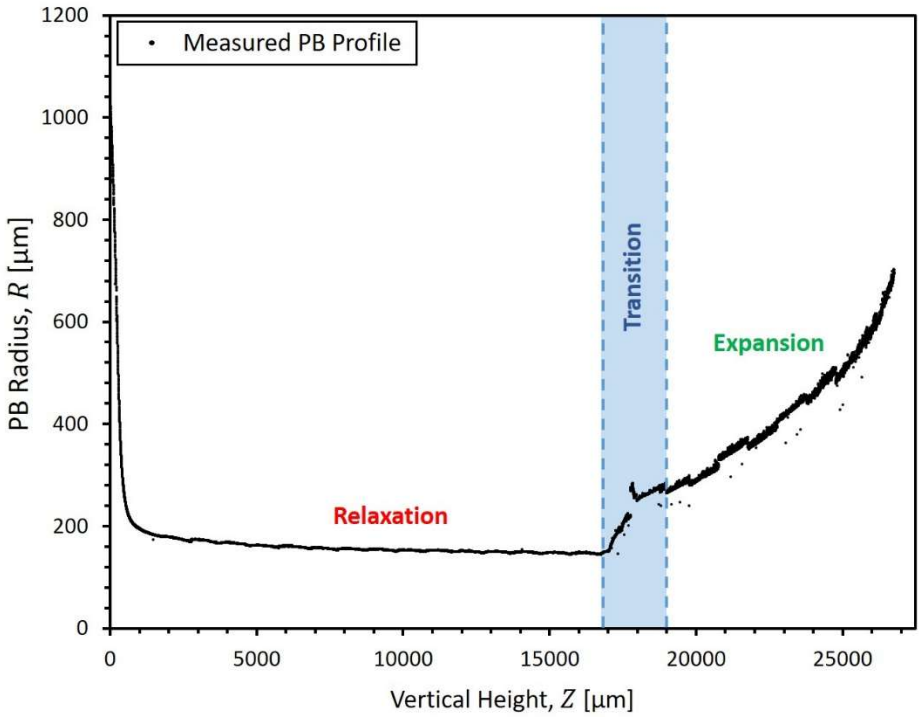

Figure 5.5. Example of the relaxation-expansion transition region visually determined from a measured PB profile.

5.3 Results

5.3.1 Solution Properties

Values for specific bulk and surface properties of surfactant solutions are presented in Table 5.1, where measured density, ρ, and dynamic viscosity, μ, were used in subsequent calculations of the surface shear viscosity, μ_s, according to Equation (5.2) and (5.7), where $\nu = \mu/\rho$. Dynamic viscosity of the Tween solutions showed the anticipated minor increase in Newtonian viscosity from pure water ($\mu \approx 8.9\times10^{-4}$ Pa·s at 25°C)[31] with increasing concentration. The viscosity of polymeric surfactants showed shear thinning behaviour, requiring the ability to determine appropriate viscosities for given liquid flow rates through their PBs. In order to do this, Equation (5.13)[9] was used to calculate the average shear rate,

$\bar{\dot{\gamma}}_S$, of a PB cross section with radius, R. While this provides an excellent representation of shear rates adjacent to the PB interface for plug flow-like velocity profiles ($D \to 0$, $I \to 1$), it was duly noted that gradually Poiseuille-like flow profiles ($D \to 312$, $I > 1$) would increasingly overestimate shear rates adjacent to the interface. As such, it was anticipated that small underestimations of dynamic viscosity in shear thinning samples would be made, causing an artificial increase in the calculated values of D according to Equation (5.3). This was taken into account in the subsequent analysis of HPMC and HPP results (see Figure 5.6).

$$\bar{\dot{\gamma}}_S \approx \frac{Q}{cR^3} \tag{5.13}$$

Surfactant & Concentration [wt%]	Density [mg/ml]	Viscosity [Pa·s] ($\times 10^4$)	Average Surface Tension [mN/m]
0.075wt% Tween 20	997.7 ± 0.3	9.56 ± 0.07	36.3 ± 0.2
0.150wt% Tween 20	997.9 ± 0.1	10.23 ± 0.48	35.9 ± 0.5
0.020wt% Tween 80	997.9 ± 0.1	8.84 ± 0.03	40.0 ± 0.5
0.039wt% Tween 80	997.6 ± 0.4	9.69 ± 0.23	39.2 ± 0.5
3.700wt% HPP	1011.0 ± 0.4	13.20 ± 0.20	43.2 ± 0.5
7.400wt% HPP	1025.8 ± 0.4	15.23 ± 0.65	41.6 ± 0.4
1.000wt% HPMC	1000.0 ± 0.1	90.20 ± 6.43	46.9 ± 0.4
2.000wt% HPMC	1002.6 ± 0.5	412.94 ± 1.43	48.1 ± 0.7

Table 5.1. Averaged results of triplicate measurements of physical properties of surfactant solutions with associated errors of one standard deviation.

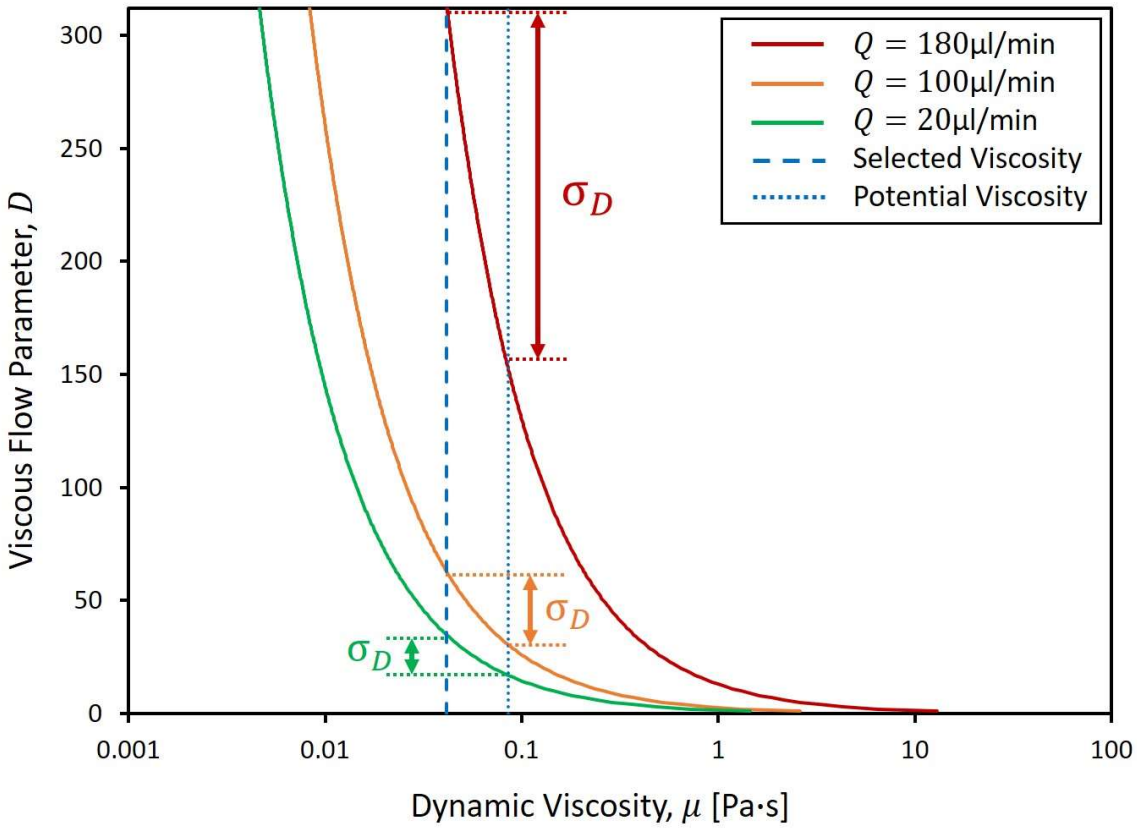

Figure 5.6. Example of errors in the calculated viscous flow parameter, D, introduced by underestimating values of the bulk viscosity μ. The red curve represents the potential values of D for 2.0wt% HPMC at 180µl/min, where a range of values of μ are used in its calculation. The dashed blue line indicates the viscosity chosen for the calculation based on the average liquid shear rate, $\dot{\gamma}_s$. As this shear rate is expected to be an overestimation of that adjacent to the PB interface, the dotted blue line represents the maximum potential viscosity at this region based on measured flow curves of 2.0wt% HPMC. The resulting potential decrease in D is indicated by the red σ_D. The same calculations are applied for liquid flow rates of 100µl/min (orange) and 20µl/min (green), demonstrating the scaling of this error with liquid flow rate.

5.3.2 Model Fitting

Measured profiles of Tween 20 and Tween 80 were found to be similar to those described by Clarke *et al.*[8], producing the anticipated flow rate dependent transitions from relaxation to expansion with increasing liquid flow rates (see Figure 5.1). A typical profile example of this is shown in Figure 5.7 for 0.075wt% Tween 20 at Q=140 µl/min, alongside the corresponding flow rate profile measured for 2wt% HPMC. Equation (5.12) was consistently able to describe both relaxation and expansion profiles for both Tween systems with a single set of values for R_e, I and γ. R-squared values confirmed this with an overall range of 0.70≤ R-Squared<1.00, and an average of 0.96. The poorest fits (e.g. R-Squared = 0.70) consistently occurred at flow rates closest to the transition from $Z_T < 0$ (Figure 5.1a) to $Z_T > 0$ (Figure 5.1b), where separate relaxation and expansion regions began to appear. This was hypothesised to be the result of rapid fluctuations between these two profile states, which were observed during image acquisition and resulted in a superposition of these states in the final PB profiles.

The measured profiles of HPMC and HPP had substantially higher radii than those for the Tween systems, yielding a previously unseen profile geometry. Figure 5.7 shows a typical example, where a solution of 2.0wt% HPMC quickly approached its equilibrium radius, R_e, before suddenly decreasing in radius as the PB transitioned into the node at $Z \approx l_1$. It is proposed that this node transition represents the case where R_e exceeds the initial node radius, R_{n0}, ($R_e > R_{n0}$) in contrast to the LMWS PB distortions that ultimately resulted from $R_e < R_{n0}$.

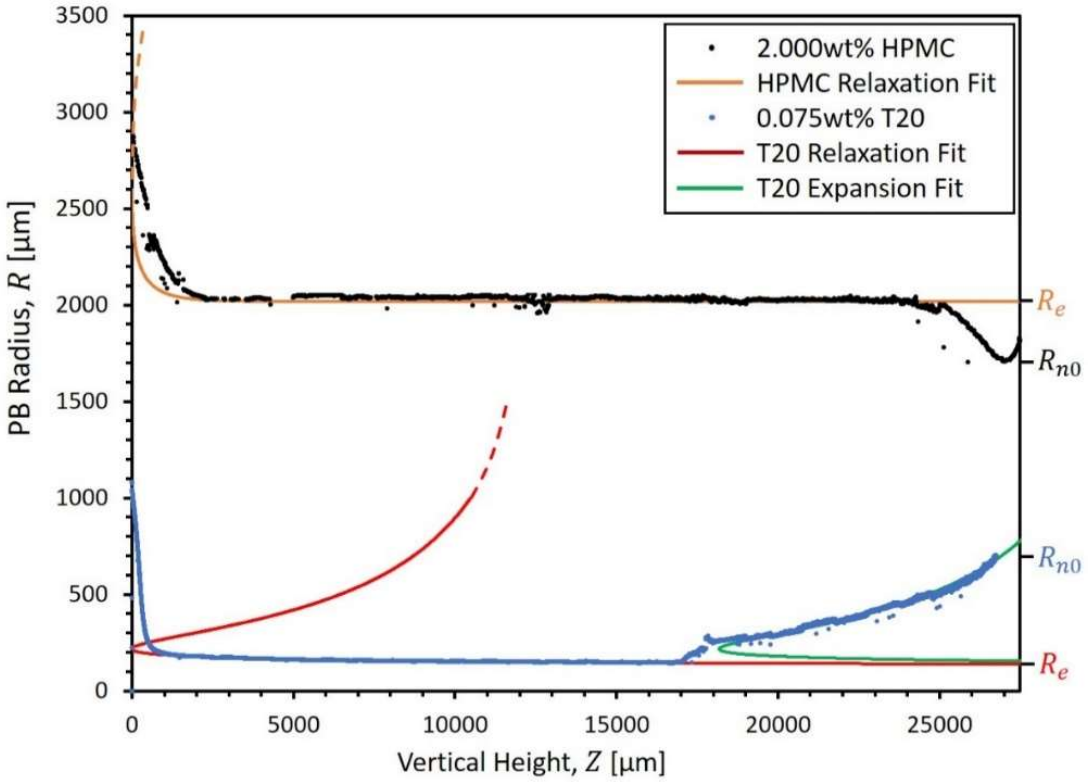

Figure 5.7. Measured profiles of 0.075wt% Tween 20 and 2wt% HPMC at Q=140µl/min, with corresponding fits of Equation (5.12). Two distinctive profile distortions emerge based on whether $R_e > R_{n0}$ (HPMC) or $R_e < R_{n0}$ (Tween 20).

A lower magnification was required to obtain images of the polymeric surfactant PBs due to its higher values of R, which increased the error margins in measured values of R_e. This made it difficult to assess whether or not any relaxation of the PB profile was due to measurement error, meaning that fitted values of γ and I could vary substantially without a marked effect of fit quality. As such, values of γ and I were neglected for further analysis for HPMC and HPP.

5.3.3 Relaxation-Expansion Transitions

The transitions between PB relaxation and expansion (see Figures 5.1, 5.3 and 5.5) were well described by Equation (5.12), as shown in Figure 5.8. Values of $Z_T > 0$ (shown by data points)

matched well with visible transition regions (see Figure 5.5) between relaxation and expansion solutions (green and red coloured regions). $Z_T < 0$ occurred where no transition regions were visible and the full profile being dominated by expansion into the node (Figure 5.1a). Once again, profiles closest to the transition between $Z_T > 0$ and $Z_T < 0$ were shown to produce the poorest match between Z_T and visible transitions, owing to the suspected superposition of these two states distorting the measured PB profiles. Overall, it was shown that Equation (5.12) was able to produce a very accurate description of the measured PB profiles, including the flow rate dependent variations in relaxation-expansion transitions.

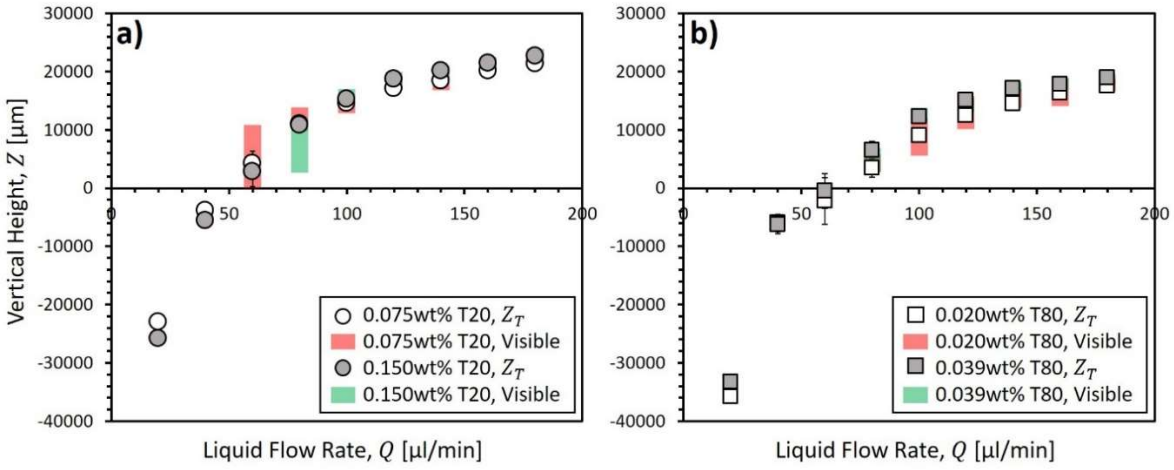

Figure 5.8. Comparison of the fitted profile offset, Z_T, for a) Tween 20 and b) Tween 80 solutions to the visible relaxation-expansion transitions observed around Z_{swell}. The full range of Z covered by the visible transition regions (see Figure 5.5) are highlighted by red and green bars.

5.3.4 Fitting Parameters

The fitted surface tension, γ, for solutions of Tween 20 and Tween 80 at discrete liquid flow rates are shown in Figure 5.9. Surface tension increased with liquid flow rate until the critical point at which relaxation and expansion solutions separated (i.e. $Z_T > 0$), after which it began to decline once more (Figure 5.9a and 7b). Minimum values of γ approach the measured equilibrium surface tensions, γ_e, of each solution. While an in-depth study of surface tension variability is beyond the scope of the current study, it was clearly observed that surface tension increased with calculated values of the apparent surface viscosity, μ_s (Figure 5.9c and 7d). As surface tension varies inversely with the surfactant concentration at the air-liquid interface[32], this would suggest that less surfactant at the interface caused an increase in the apparent surface viscosity. This counterintuitive result is explained when one considers that the range of apparent surface viscosity values calculated here was in the range 10^{-10} g/s$< \mu_s <10^{-8}$ g/s, while the surface shear viscosity of pure water is approximately 1.2×10^{-5} g/s[33]. Therefore, it follows that a decreased population of surfactant species must increase the surface viscosity as a pure air-water interface is approached.

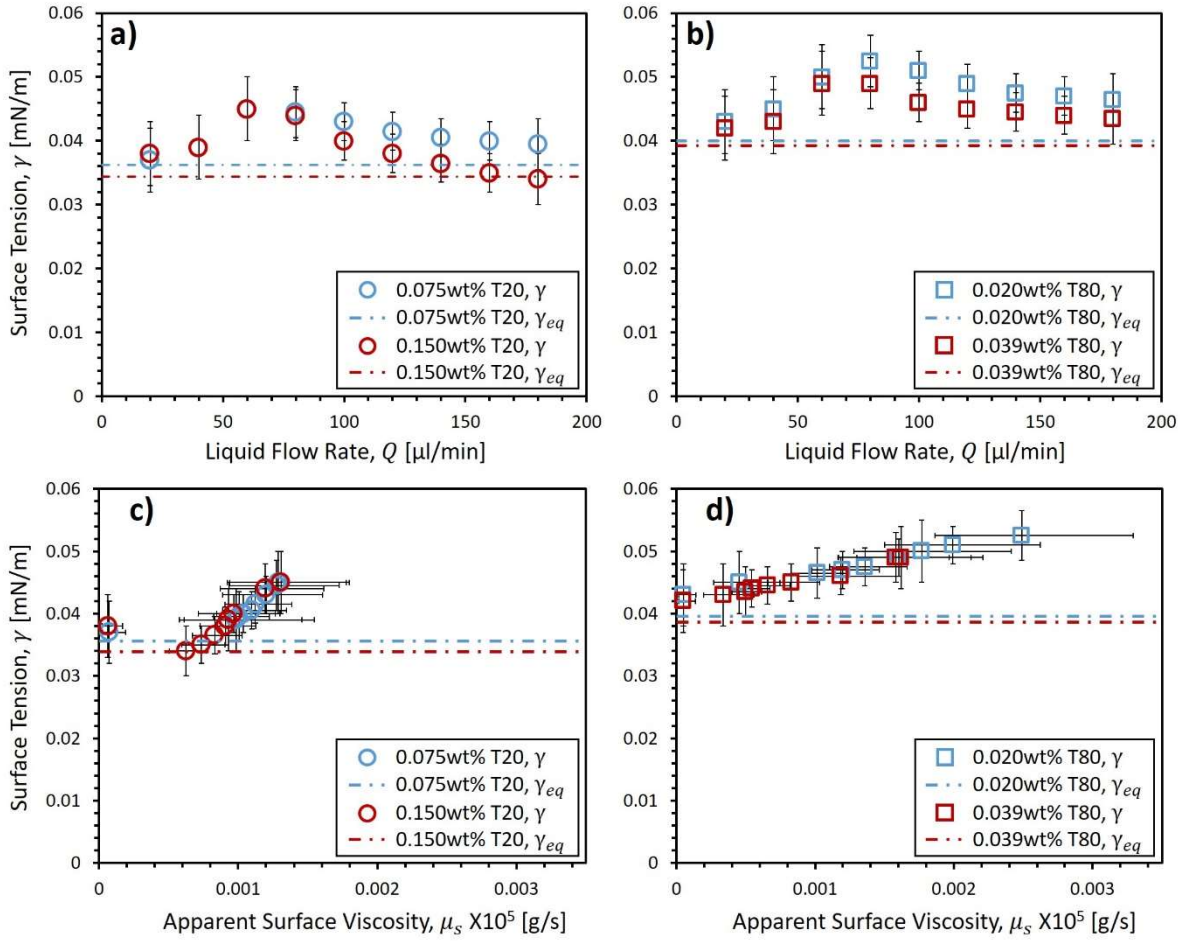

Figure 5.9. Surface Tensions, γ, from fits of Equation (5.12) to a) & c)Tween 20 and b) & d) Tween 80 PB profiles. a) & b) show the relationship between γ and Liquid Flow Rate, Q, while c) & d) show the relationship between γ and the Apparent Surface Viscosity, μ_s, calculated from Equation (5.3), (5.7) and (5.8).

Values for the inertial flow parameter, I, of Tween solutions can be found in Figure 5.10, where they are plotted alongside the calculated values of the viscous flow parameter, D, for the equilibrium PBs ($R = R_e$). As discussed in Section 1.2.1 (Equation (5.5) & (5.6)), the values of I and D describe the flow velocity profiles, where $I \to 1$ as $D \to 0$ as perfect plug flow is approached. This relationship was well described by Figure 5.10, and matches well with the finding of a virtually inviscid interface for the PBs calculated here. The size of the error margins

in I made it difficult to draw any firm conclusions on the impact of the different surfactants on the I-D relationship, however combining all solutions indicated the same fundamental trend.

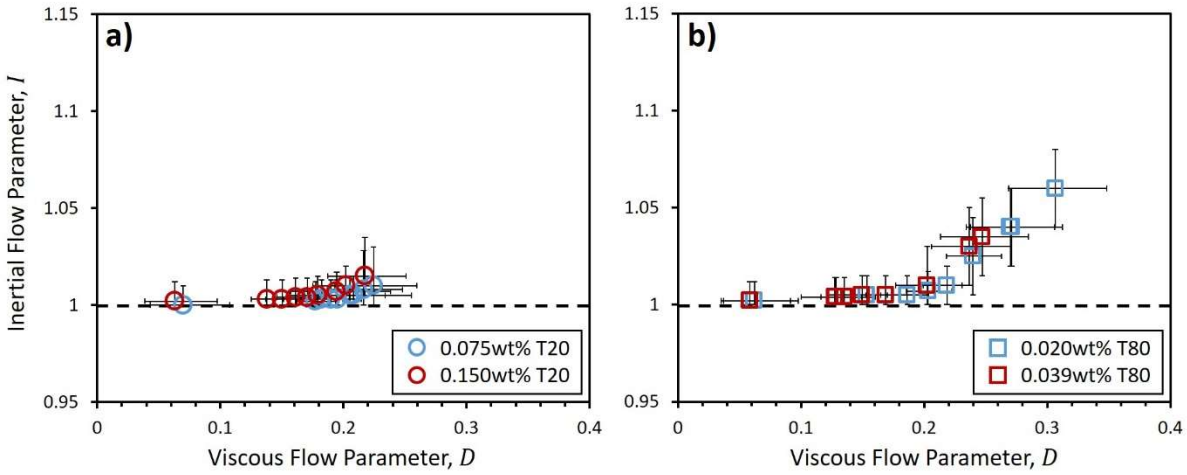

Figure 5.10. Inertial Flow Parameters, I, vs. Calculated Viscous Flow Parameters, D, from fits of Equation (5.12) to a) Tween 20 and b) Tween 80 PB profiles. Black dashed line represents a value of 1 and the physical lower limit of I.

Despite it not being possible to establish meaningful values of I and γ for polymeric surfactant solutions, the calculated values of D from the fitted equilibrium radii, R_e (Equation (5.3)), could still be compared to LMWS solutions. Figure 5.11 shows that values of D for solutions of HPMC and HPP lay at the opposite end of the spectrum from the Tween solutions, approaching the limits of an immobile interface as $D \to 312$. As a general trend, it was noted that the average D value (and consequently μ_s) for a given surfactant solution strongly related to its average liquid shear rate, with high D producing lower liquid shear rates and *vice versa*. Visualisations of the kind of flow velocity profiles expected between these low mobility and high mobility regimes are shown in the relevant regions of Figure 5.11.

Values of μ_s for HPMC were calculated to range from 10^{-1}g/s< μ_s <10^{1}g/s for 2.0wt% and to be consistently of the order 10^{-2}g/s for 1.0wt% concentration. This was a strong indication that these concentrations produced the gelled PB interfaces described in Section 2.1, where the higher concentration would be expected to have increased gel strength[27] and therefore an interface of enhanced resistance to liquid shear.

Values of μ_s for HPP solutions were in the range 10^{-3} g/s< μ_s <10^{-2} g/s for both concentrations, indicating a higher mobility of the hydrolysed protein chains at the interface than HPMC. This suggested that the HPP viscoelastic network at the interface was weaker than that of HPMC.

The values of μ_s for the Tween systems were in the extremely low range of 10^{-10} g/s< μ_s <10^{-8} g/s, where μ_s decreased with increasing liquid shear rate $\bar{\dot{\gamma}}_s$ in a manner similar to that observed by Clarke *et al.*[8] for a solution of SDS. At this stage, it is anticipated that the apparent surface shear thinning effect is related to the variation in surfactant population at the interface that was seen from the variation in PB surface tension (Figure 5.9). A more complete analysis of the surface tension variability will be required in order to better understand this effect however.

It is important to remember that the values for D and subsequently μ_s were calculated for equilibrium PB systems ($R = R_e$), representing the maximum shear rates at any given liquid flow rates. In the Tween systems, values of R for a given PB profile could be over 3.5 times higher than the corresponding R_e value, decreasing shear rates by up to 2 orders of magnitude. By estimating values of D and μ_s based on the equilibrium PB trends in Figure 5.11, this could yield values of D with magnitudes as high as 10^0 for the Tween systems, with

subsequent values of μ_s in the order of 10^{-7}g/s. As the average D in a given region of PB profile is expected to scale with its inertial flow parameter, I (Figure 5.10), this suggests the need to address the small variations in physical parameters that are likely to occur between the expansion and relaxation regions of the PB profile. Indeed, future work should seek to fit Equation (5.12) separately to these regions, where it is expected that fit quality will further increase.

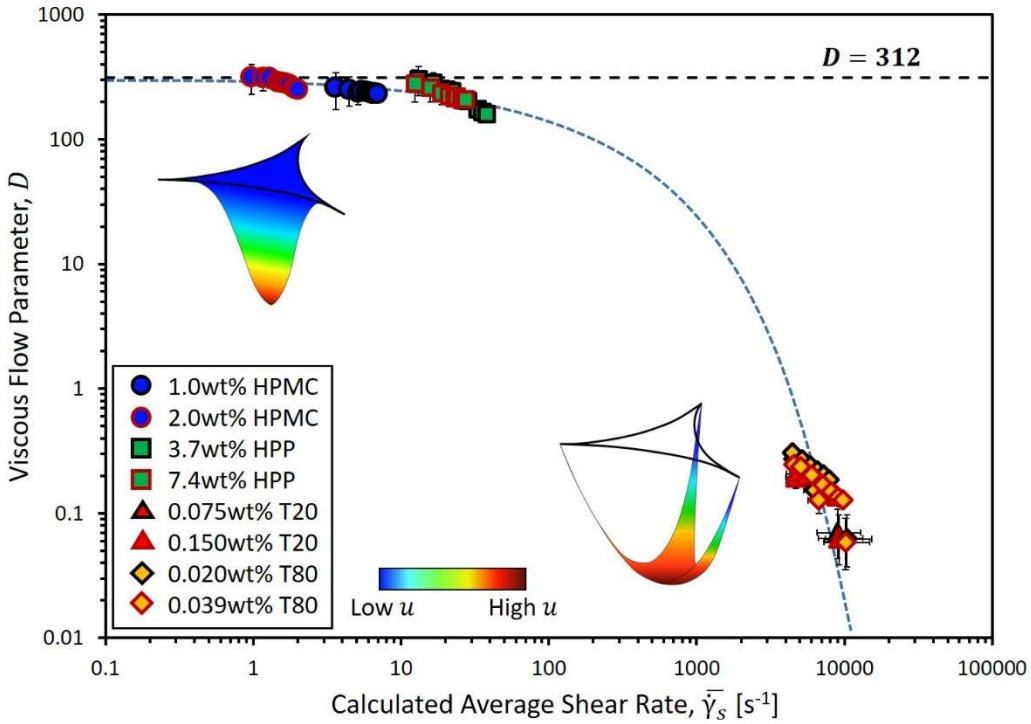

Figure 5.11. Viscous Flow Parameter, D, vs. Calculated Average Shear Rate, $\overline{\dot{\gamma}_s}$, for HPMC, HPP, Tween 20 and Tween 80 solutions. The dashed blue line is to guide the eye. The physical limit of D = 312 is indicated. Visualisations of liquid flow velocity profiles are given alongside relevant data regions, where colours indicate liquid flow velocities, u, from low velocities (blue) to high velocities (dark red). Velocity profiles of HPMC and HPP show near ideal Poiseuille flow, while Tween systems were closer to ideal plug flow.

5.4 Conclusions

The novel experimental setup of Clarke*, et al.*[8] was further investigated using updated theory derived from the standard drainage theory[16] to model both PB relaxation and PB expansion in food grade surfactant systems. The updated theory was able to accurately describe the full length of measured PB profiles, including previously unexplained transitions between profile expansion and relaxation. The shapes and vertical heights of these transitions along the PB, Z_T, were shown to result from the difference between the equilibrium PB Radius, R_e, and the initial radius of the adjoining node, R_{n0}, where the change in PB radius with height was limited by the bulk and surface properties of the surfactant solutions. These transitions have so far been seen exclusively for the low molecular weight surfactant systems SDS[8], Tween 20 and Tween 80 where $R_e < R_{n0}$. However, the polymeric surfactant systems of HPP and HPMC also investigated here, demonstrated the inverted case of this distortion, where $R_e > R_{n0}$. To this author's knowledge, this is the first such case to be described in literature.

The fitting parameters R_e, surface tension, γ, and inertial flow parameter, I, were used to match theory to PB profiles at controlled liquid flow rates, Q. A single set of fitting parameters was used for each liquid flow rate, representing averaged values for the full PB profile. Despite this producing a good representation of these systems, it was shown that the increase in average PB radius of the PB expansion regions would have been expected to result in minor increases to the inertial flow parameter, I. As such, it is recommended that further investigation of LMWS solutions with this technique use separate fitting variables for PB relaxation and expansion regions.

While meaningful values for I and γ could not be obtained from fits to HPMC and HPP, the calculated values of the dissipative flow parameter, D, from R_e allowed a clear comparison between polymeric surfactants and LMWS to be made. Values for HPMC and HPP both tended towards the upper limit of D=312, with average values of D=263 for HPMC solutions and D=225 for HPP solutions. Values for Tween 20 and Tween 80 both tended towards the lower limit of D=0, with average values of D=0.17 for Tween 20 solutions and D=0.19 for Tween 80 solutions. These findings showed that the current technique was clearly able to differentiate between the viscous dominated and inertial dominated flow regimes.

Despite the expected clear separation of low and high mobility interfaces, it was noted that the accuracy with which the HPMC and HPP interfaces were characterised was relatively poor. This was primarily due to the need for highly accurate values of the bulk viscosity, μ, when calculating D, which was non-trivial for these non-Newtonian solutions. These errors were reduced at lower liquid flow rates however, where variations in μ produced less significant variations in calculated values of D.

Values of equilibrium PB μ_s for Tween 20 and Tween 80 solutions were within the range of 10^{-10} g/s$< \mu_s <$$10^{-8}$ g/s representing a virtually inviscid interface in both cases. A degree of surface shear thinning was observed in a similar manner to that of Clarke *et al.*[8] for SDS solution, which is proposed to be related to variations in surfactant population at the PB interface. This hypothesis was based on the observation of a single trend of increasing μ_s with increasing surface tension for regardless of surfactant concentration. A more in depth numerical analysis of these findings will be essential in establishing whether the occurrence

of such surface shear thinning for LMWS systems is a real effect or an artefact of the measurement technique.

Overall, the results presented here show that the PB-Node setup was able to describe highly complex PB profiles using bulk and interfacial physical variables that consistently fell within expected limits. Despite the lower accuracy in measuring the surface viscosities of polymeric surfactant systems, it was clear that the technique could clearly distinguish them from the extreme low surface viscosity LMWS systems of Tween 20 and Tween 80. Values calculated for LMWS surface viscosity clearly show them to be below the measurement sensitivity of conventional techniques as predicted in existing literature[22]. Therefore, it is believed by this author that further analysis of such systems in this manner present a great opportunity to probe the fundamental mechanisms underlying LMWS surface viscosity in PB systems.

5.5 References

1 J. Wang; A. V. Nguyen; S. Farrokhpay, A Critical Review of the Growth, Drainage and Collapse of Foams, *Advances in Colloid and Interface Science* **2016**, *228*, 55-70.

2 A. J. Green; K. A. Littlejohn; P. Hooley; P. W. Cox, Formation and Stability of Food Foams and Aerated Emulsions: Hydrophobins as Novel Functional Ingredients, *Current Opinion in Colloid & Interface Science* **2013**, *18*, 292-301.

3 R. J. Pugh, *Bubble and Foam Chemistry*; Cambridge University Press: Cambridge, United Kingdom, **2016**.

4 A. L. Ellis; A. B. Norton; T. B. Mills; I. T. Norton, Stabilisation of Foams by Agar Gel Particles, *Food Hydrocolloids* **2017**, *73*, 222-228.

5 ChunxiLi; MinglanLi; ZhixianShi; XueminYe, Effect of Soluble Surfactants on Vertical Liquid Film Drainage, *Physics of Fluids* **2019**, *31*, 032105.

6 F. Rouyer; O. Pitois; E. Lorenceau; N. Louvet, Permeability of a Bubble Assembly: From the Very Dry to the Wet Limit, *Physics of Fluids* **2010**, *22*, 043302.

7 S. Naire; R. J. Braun; S. A. Snow, An Insoluble Surfactant Model for a Vertical Draining Free Film with Variable Surface Viscosity, *Physics of Fluids* **2001**, *13*, 2492-2502.

8 C. Clarke; A. Lazidis; F. Spyropoulos; I. T. Norton, Measuring the Impact of Channel Length on Liquid Flow through an Ideal Plateau Border and Node System, *Soft Matter* **2019**, *15*, 1879-1889.

9 F. Elias; E. Janiaud; J.-C. Bacri; B. Andreotti, Elasticity of a Soap Film Junction, *Physics of Fluids* **2014**, *26*, 037101.

10 P. M. Kruglyakov; S. I. Karakashev; A. V. Nguyen; N. G. Vilkova, Foam Drainage, *Current Opinion in Colloid & Interface Science* **2008**, *13*, 163-170.

11 Q. SUN; L. TAN; G. WANG, Liquid Foam Drainage: An Overview, *International Journal of Modern Physics B* **2008**, *22*, 2333-2354.

12 S. S. Thete; C. Anthony; P. Doshi; M. T. Harris; O. A. Basaran, Self-Similarity and Scaling Transitions During Rupture of Thin Free Films of Newtonian Fluids, *Physics of Fluids* **2016**, *28*, 092101.

13 A. Anazadehsayed; N. Rezaee; J. Naser, Numerical Modelling of Flow through Foam's Node, *Journal of Colloid and Interface Science* **2017**, *504*, 485-491.

14 I. Cantat; S. Cohen-Addad; F. Elias; F. Graner; R. Höhler; O. Pitois; F. Rouyer; A. Saint-Jalmes; S. Cox, *Foams: Structure and Dynamics*; Oxford University Press: New York, **2013**.

15 A. Anazadehsayed; N. Rezaee; J. Naser; A. V. Nguyen, A Review of Aqueous Foam in Microscale, *Advances in Colloid and Interface Science* **2018**, *256*, 203-229.

16 D. Weaire; S. Hutzler; G. Verbist; E. Peters; I. Prigogine; S. A. Rice, A Review of Foam Drainage, *Advances in Chemical Physics* **1997**, *102*.

17 O. Pitois; N. Louvet; E. Lorenceau; F. Rouyer, Node Contribution to the Permeability of Liquid Foams, *Journal of Colloid and Interface Science* **2008**, *322*, 675-677.

18 O. Pitois; C. Fritz; M. Vignes-Adler, Liquid Drainage through Aqueous Foam: Study of the Flow on the Bubble Scale, *Journal of Colloid and Interface Science* **2005a**, *282*, 458-465.

19 O. Pitois; C. Fritz; M. Vignes-Adler, Hydrodynamic Resistance of a Single Foam Channel, *Colloids and Surfaces A: Physicochemical and Engineering Aspects* **2005b**, *261*, 109-114.

20 M. Kostoglou; E. Georgiou; T. D. Karapantsios, A New Device for Assessing Film Stability in Foams: Experiment and Theory, *Colloids and Surfaces A: Physicochemical and Engineering Aspects* **2011**, *382*, 64-73.

21 K. Koczó; G. Rácz, Flow in a Plateau Border, *Colloids and Surfaces* **1987**, *22*, 95-96.

22 Z. A. Zell; A. Nowbahar; V. Mansard; L. G. Leal; S. S. Deshmukh; J. M. Mecca; C. J. Tucker; T. M. Squires, Surface Shear Inviscidity of Soluble Surfactants, *Proceedings of the National Academy of Sciences* **2014**, *111*, 3677-3682.

23 D. Weaire; S. Hutzler, *The Physics of Foams*; Oxford University Press: New York, **1999**.

24 A. Saint-Jalmes; Y. Zhang; D. Langevin, Quantitative Description of Foam Drainage: Transitions with Surface Mobility, *Eur. Phys. J. E* **2004**, *15*, 53-60.

25 A. Saint-Jalmes, Physical Chemistry in Foam Drainage and Coarsening, *Soft Matter* **2006**, *2*, 836-849.

26 A. V. Nguyen, Liquid Drainage in Single Plateau Borders of Foam, *Journal of Colloid and Interface Science* **2002**, *249*, 194-199.

27 Dow, Methocel Cellulose Ethers Technical Handbook. The Dow Chemical Company: USA, 2002; p. 29. http://msdssearch.dow.com/PublishedLiteratureDOWCOM/dh_096d/0901b8038096d9ff.pdf?filepath=methocel/pdfs/noreg/192-01062.pdf&fromPage=GetDoc (accessed 24/07/2019).

28 M. C. Tulbek; R. S. H. Lam; Y. Wang; P. Asavajaru; A. Lam, Chapter 9 - Pea: A Sustainable Vegetable Protein Crop. In *Sustainable Protein Sources*, Nadathur, S. R.; Wanasundara, J. P. D.; Scanlin, L., Eds. Academic Press: San Diego, **2017**; pp 145-164.

29 K. L. Mittal, Determination of Cmc of Polysorbate 20 in Aqueous Solution by Surface Tension Method, *Journal of Pharmaceutical Sciences* **1972**, *61*, 1334-1335.

30 A. Patist; S. S. Bhagwat; K. W. Penfield; P. Aikens; D. O. Shah, On the Measurement of Critical Micelle Concentrations of Pure and Technical-Grade Nonionic Surfactants, *Journal of Surfactants and Detergents* **2000**, *3*, 53-58.

31 Anton-Paar Viscosity of Water. https://wiki.anton-paar.com/en/water/ **2008**. (accessed 18/04/2019).

32 K. Kinoshita; E. Parra; D. Needham, Adsorption of Ionic Surfactants at Microscopic Air-Water Interfaces Using the Micropipette Interfacial Area-Expansion Method: Measurement of the Diffusion Coefficient and Renormalization of the Mean Ionic Activity for Sds, *Journal of Colloid and Interface Science* **2017**, *504*, 765-779.

33 J. C. Earnshaw, Surface Viscosity of Water, *Nature* **1981**, *292*, 138-139.

Chapter 6

A Flow Velocity Dependence of Dynamic Surface Tension in Plateau Borders of Foam

Published as: C. Clarke; F. Spyropoulos; I. T. Norton, A Flow Velocity Dependence of Dynamic Surface Tension in Plateau Borders of Foam, *Journal of Colloid and Interface Science,* **2020**, *573*, 348-359.

6.0 Abstract

Liquid drainage through foams is a multiscale process, that primarily occurs through channels known as Plateau borders (PBs). Recent experimental studies of isolated PBs have observed variations in channel surface tension, γ, with liquid flow rate, Q, for systems containing soluble low molecular weight surfactant (LMWS). The current study proposes that the dynamic surface tension (DST) could be responsible for this effect, where the residence time of surfactant molecules in the PB is similar to the time required for their adsorption to the channel interface.

Profile geometries of isolated 'ideal' PB's were created in a bespoke experimental setup at controlled forced liquid flow rates. Average surfactant residence times, τ_{Res}, were calculated for solutions of Sodium Dodecyl Sulfate (SDS), Tween 20 (T20) and Tween 80 (T80), and used to calculate corresponding average DST values in discrete regions of measured PB profiles. DST values were combined with microscale drainage theory to assess the potential physical implications on liquid flow.

Significant variations in the magnitude of γ were calculated based on surfactant characteristics, where only the rapid adsorption of SDS was sufficient to produce DST values approaching equilibrium. These findings seriously question assumptions of near equilibrium surface tension in LMWS foam systems above their critical micelle concentration (CMC). Furthermore, the presence of surface tension gradients identified using this discrete approach, highlights the need to further refine the current theory to a continuous approach incorporating Marangoni effects.

6.1 Introduction

6.1.1 Background

Foam drainage is a highly complex phenomenon that is the combined result of dynamic processes occurring over a range of different length-scales[1]. Because of its essential role in destabilising foams, those seeking foam longevity often aim to retard this process, typically employing basic assumptions regarding liquid flow to inform a trial and error approach to formulation development[2]. While this tactic has been met with measured success, the increasing demand for foams with specific functionality, using a limited range of ingredients, has necessitated a much more rigorous approach to understanding foam microstructure and its impact on microscale liquid flow[3]; which in turn drives macroscopic behaviour.

At the microscale, liquid transport through foams primarily occurs through the interconnected network of channels between bubbles, known as Plateau Borders (PBs), and their junctions, or Nodes[4,5]. As these structures ultimately form the 'building blocks' of macroscopic foams, their microscale behaviour is scaled accordingly, thereby describing the overall functionality[6]. One common approach is to 'build' a picture of macroscopic foam drainage by 'adding' the hydrodynamic resistance of isolated channels and nodes in series[7]. It can be seen therefore, that any inaccuracies in the properties of these isolated systems propagate to a substantial degree of error when scaled to describe macroscopic systems.

Modelling foam channels using a theoretical framework represents the substantial majority of research undertaken in the area of foam channel drainage. However, even using simplified models to represent real systems has proved challenging, with results often conflicting[7,8].

This is largely due to the wide range of co-dependent variables involved in the process, which dramatically increases the complexity of the systems studied. For example, the surface rheology of foam channels is dependent on the shear imparted on it by flow of bulk liquid[9]; however, liquid flow rates vary with bulk liquid rheology and channel widths, which are themselves dependent upon the surface rheology and surface tension[10,11]. As such, one cannot treat any of these variables in isolation without directly measuring or resorting to assumptions regarding the others.

In addition to the difficulties faced by theoretical modelling, there are very few studies dedicated to the experimental measurement of microscale foam channels[12]. This means that any predictions that are made from microscale drainage models are difficult to assess for accuracy in real systems. This is largely due to the difficulties in effectively measuring such systems, which can be extremely difficult to isolate and effectively control in macroscopic foams[13].

More recently, studies of isolated PB and PB-Node geometries in bespoke experimental setups have provided an alternative to microscale measurements made from macroscopic foams. The superior control and repeatability provided by these systems has allowed for more detailed experimental studies into the co-dependence of PB bulk and surface parameters during microscale drainage. To date, isolated foam systems have been used to study a range of surfactants, including ionic and non-ionic low molecular weight (LMWS) systems[6,7,14-17], as well as more limited investigations of protein and polysaccharide solutions[10]. While these studies have been able to identify fundamental differences in key parameters such as surface

shear viscosity for different surfactant systems, the practical difficulties in measuring such systems still necessitate certain assumptions to be made.

A major assumption that features heavily in both microscale and macroscale foam drainage concerns the PB surface tension, which is an important parameter for determining bubble and channel dimensions, but is not measured *in-situ*. Instead, foam surface tensions are generally approximated based on the results of more conventional measurement techniques such as Wilhelmy Plate, Pendant Drop, Expanding Bubble, etc.[5]. It is generally considered, for example, that soluble LMWS solutions above their critical micelle concentration (CMC) produce foams with surface tensions approaching equilibrium, γ_e[18]. Recently however, measurements of isolated Tween 20 and Tween 80 PB geometries at constant liquid flow rates, have suggested this may not be the case, with the appearance of an apparent flow rate dependent surface tension[10].

The idea of time-dependent surface tension is certainly not new, and has been studied extensively for a wide range of surface-active species and concentrations[19-24], with adsorption dynamics for solutions above the CMC being further influenced by the presence of micelles[25,26]. This dynamic surface tension (DST), γ, is primarily governed by the rate of adsorption of surface active molecules/particles to the air-liquid interface, where transport of surfactant molecules to the interface is either dominated by convection or diffusion, followed by a characteristic adsorption time. The dominant effect can generally be identified by solving the convective diffusion equation and using the Péclet's criterion to assess the relative magnitude of the terms[27,28]. In the case of soluble LMWS systems with static boundaries for example, adsorption is generally dominated by diffusion[20]. The rate of diffusion is highly

dependent on the diffusivity of the LMWS species and the dimensions of the liquid channel, which therefore dictates how quickly surfactants are able to reduce surface tension when adsorbing at an interface.

The application of DST models to Plateau borders with liquid flow becomes far more complex, partially because of the geometry of the PB cross-section, but also because of the surface velocity of the PB interface. While a detailed physicochemical approach to the problem of PB drainage has been put forward by Durand*, et al.*[11], a means of experimentally validating these findings at the scale of individual Plateau borders remains elusive. In the more simplistic case of flow in horizontal liquid films, more experimental data is available, where the Marangoni effect describes the influence of surfactants on the hydrodynamics of the system, preventing localised thinning and therefore improving film stability[27-31]. More recently, the experimental examination of vertical films draining under the force of gravity have yielded interesting findings relating to the stability of thin films due to forced liquid flow[32] that may have parallels with forced flow in Plateau borders.

In the study of de Gennes[32], the impact of soap film drainage rates on surface tension and film stability is described. As the liquid flow increased, it was found that slower diffusing surfactants did not have time to adsorb at the air-water interface before exiting the film. These films, with reduced surfactant concentration at the interfaces, were termed 'Young' films due to liquid flows being faster during the early stages of film drainage. It follows therefore, that such a mechanism is also likely to play a role in the stabilisation of PBs, where the inherently higher liquid flow rates would be expected to accentuate the effects seen by de Gennes[32]. If the majority of surfactant molecules were transported through the PB before being able to

adsorb at the interface, then values of PB surface tension higher than γ_e could be expected, potentially lowering PB stability.

This study aims to provide a method that can assess the degree to which liquid flow rate could affect PB surface tension for high mobility surfactant species based on their characteristic adsorption behaviour. The ability to control liquid flow rates through well-defined PB geometries using the experimental setup of Clarke*, et al.*[10] means that the 'ageing' of PBs should be effectively halted. As was shown for de Gennes[32] 'young' films, adjoining 'young' PBs could also suffer from reduced stability during the early stages of macroscopic foam drainage. As such, it is hoped that the current study will help to produce a more complete picture of the fundamental mechanisms underlying drainage and stability of LMWS macroscopic foams. Ultimately, this may prove valuable for researchers hoping to identify suitable surfactant species and concentrations for specific formulation applications.

6.1.2 Theory

6.1.2.1 Model Fitting to Geometric PB Profiles

In chapters 5 and 6, the geometries of vertical, isolated PB's were measured at different forced liquid flow rates, Q, and fitted with solutions to the standard drainage theory[13,17] (Equation (6.1)). This dynamic equation accounts for the liquid flow through a PB tangential to the vertical axis, Z, with a radius, R, and the physical parameters I, D, ν, g, γ, and ρ denoting inertial and viscous flow parameters, kinematic viscosity, acceleration due to gravity, surface tension and bulk liquid density, respectively. The constant, c, is a geometric factor (~ 0.161) which can be used to describe the thin-film PB cross-section with area, $S = cR^2$ (See Figure 6.1c). The parameters D and I are dimensionless variables that describe the shape of the

velocity flow field through the PB and ultimately depend on the surface rheology of the PB interface. Further information on these is given below and can also be found in Appendix B. Appendix B also gives a more complete description of Equation (6.1) and its derivation, in order to provide additional physical context.

$$\frac{dR}{dZ} = \frac{cDvQ - {}^{2}R^{4}}{\left(\frac{2IQ^{2}}{R}\right) - \left(\frac{c^{2}R^{2}\gamma}{\rho}\right)} \qquad \text{The standard drainage theory} \qquad (6.1)$$

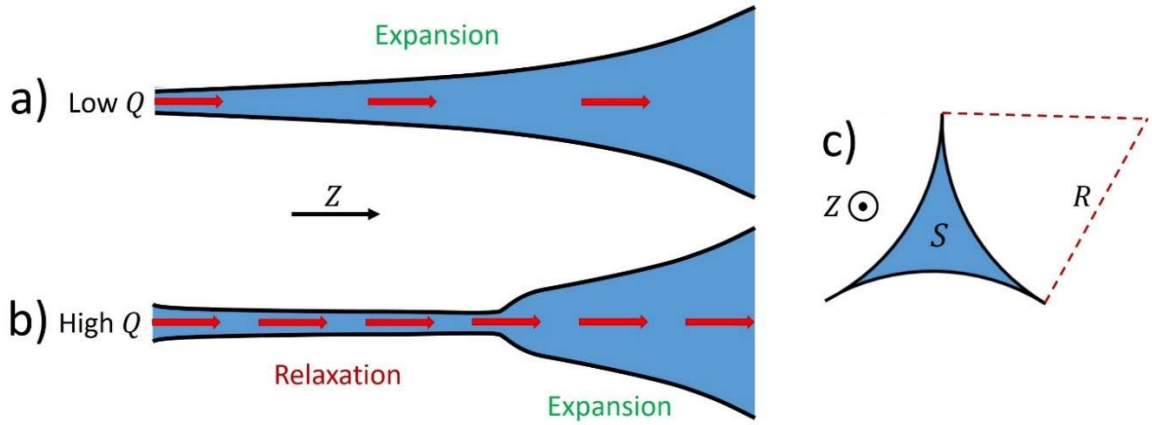

Figure 6.1. a) Typical low flow rate, Q, PB vertical cross-section for LMWS systems. b) Typical high flow rate PB vertical cross-section for LMWS systems. c) Thin-film PB horizontal cross-section with radius, R, and area, S.

As can be seen from Figures 6.1a) & 6.1b), measured PB profiles for LMWS systems have been shown to exhibit complex flow rate dependent geometries comprised of regions of relaxation and expansion. The geometric solution to Equation (6.1) for constant I and γ, as proposed in chapter 5, was shown to account for both relaxation and expansion of the PB profile (see Figure 6.2) and is given by Equation (6.2), which was derived in section 5.1.2.2.

$$Z - Z_T = L\, ln\left[\frac{R^4\left({R_0}^4 - {R_e}^4\right)}{{R_0}^4\left(R^4 - {R_e}^4\right)}\right] + \frac{{L_c}^2}{4R_e}\left\{ln\left[\frac{R^4(R_0+R_e)^2\left({R_0}^2+{R_e}^2\right)}{{R_0}^4(R+R_e)^2\left(R^2+{R_e}^2\right)}\right] + 2\,tan^{-1}\left[\frac{R-R_0}{R_e\left(1+RR_0/{R_e}^2\right)}\right]\right\} \qquad (6.2)$$

In this solution, the constant values of the inertial flow parameter, I, and surface tension, γ, result in values for an initial PB radius, R_0, according to Equation (6.3), that is located at a vertical offset, Z_T, from the top of the PB at $Z = 0$ (Figure 6.2). The PB equilibrium radius, R_e, is defined by Equation (6.4), describing the lower limit of the PB radius, at which gravity and viscous dissipation are balanced[17]. The vertical distance over which R_0 transitions to R_e is determined by the PB relaxation length, L, which is given by Equation (6.5). Finally, the variable L_c, refers to the capillary length defined as $L_c = \sqrt{\gamma/\rho\, g}$.

$$R_0 = \left(\frac{2\rho I Q^2}{c^2 \gamma}\right)^{1/3} \tag{6.3}$$

$$R_e = \left(\frac{D\nu Q}{cg}\right)^{1/4} \tag{6.4}$$

$$L = \frac{IQ^2}{2c^2 g {R_e}^4} - \frac{\gamma}{4\rho g R_e} \tag{6.5}$$

Figure 6.2 shows that Equation (6.2) takes the form of a curve with two solutions for R for a given value of Z, and demonstrates the application to PB profiles exhibiting regions of relaxation and expansion similar to that in Figure 6.1b.

Section 5.1.2.2 showed that a single set of physical variables for Equation (6.2) could be used to describe both expansion and relaxation regions of the PB, where it was assumed that the effect of variations in R would be small within a single PB. However, it was found that the agreement between theory and data decreased sharply for PBs at flow rates close to the transition point between profiles of the type shown in Figure 6.1a to those in Figure 6.1b (i.e. relaxation only to combined relaxation AND expansion). Furthermore, analysis of the fitting parameters indicated the counterintuitive result that an *increase* in surface concentration of

surfactant at the PB interface acted to *lower* its surface shear viscosity, μ_s. As such, it was deemed necessary to account for the impact of variations in R within a single PB in future studies.

When one considers, the physical interpretation of the viscous and inertial flow parameters as describing the shape of flow velocity profiles through a horizontal PB cross-section, the need to account for R dependence in a single PB becomes clear. Equations (6.6) and (6.7) show the relationship between the velocity field of liquid flow through the PB[17], $\vec{u}(x, y)$, and the viscous and inertial flow parameters obtained by averaging across the horizontal PB cross-section (see Elias*, et al.*[17] for details). At a constant liquid flow rate, the average flow velocity, $\bar{u}$, through an ideal horizontal PB cross-section can be calculated from Equation (6.8), such that the dependence of both D and I on PB radius is taken into account[17]. Note that in Equation (6.6), $\overline{\Delta u}$ describes the Laplacian of the velocity flow field averaged over the horizontal PB cross-section.

$$D = -R^2\overline{\Delta u}/\bar{u} \tag{6.6}$$

$$I = \overline{u^2}/_{\bar{u}^2} \tag{6.7}$$

$$\bar{u} = Q/cR^2 \tag{6.8}$$

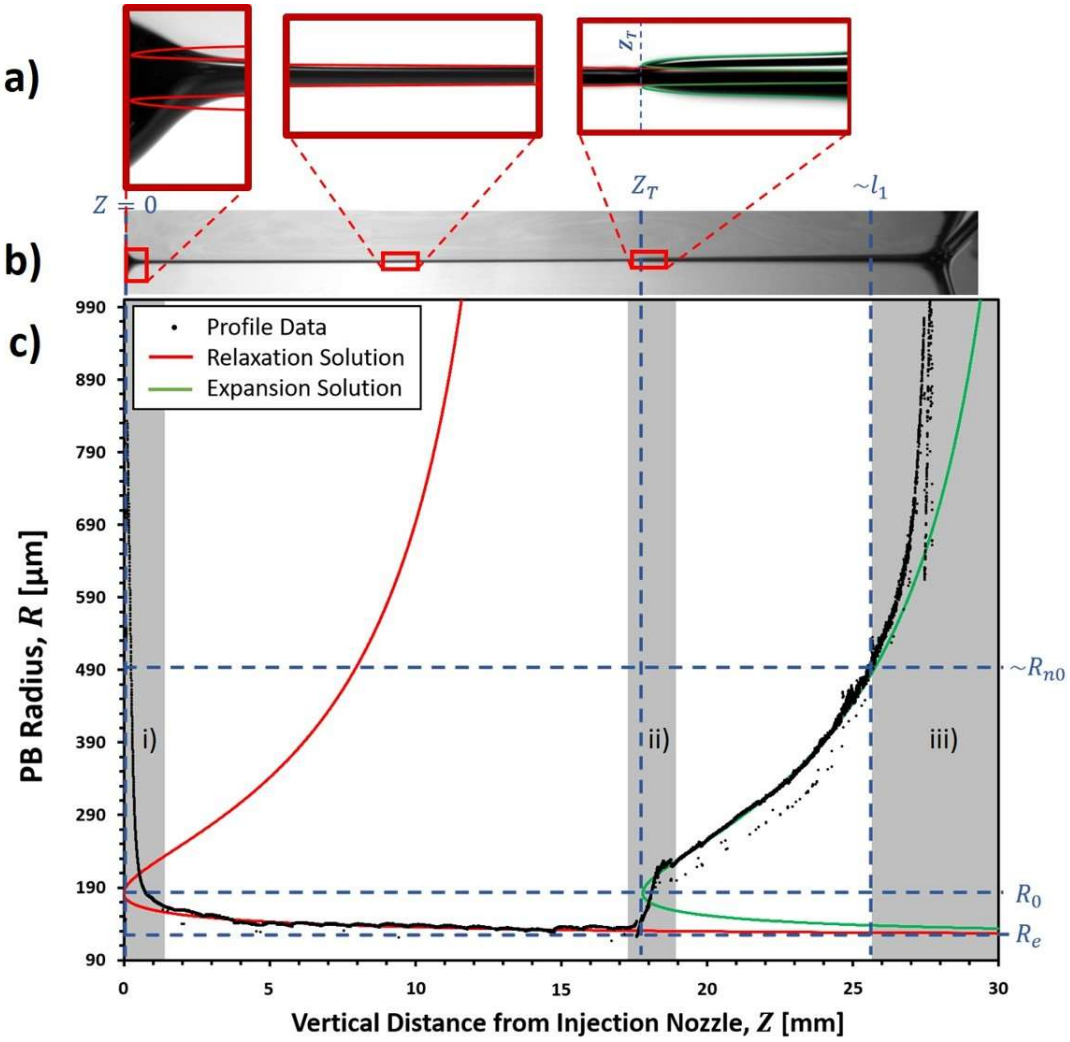

Figure 6.2. a) High magnification view of highlighted profile regions with visualisation of fitted curved overlaid. b) Low magnification PB profile image. c) Example of Equation (6.2) fit to profile data for a 182mM SDS solution at a flow rate of 100µl/min. Dashed blue lines indicate the position of key geometric variables. Grey shaded regions indicate poorly defined transitions/distortions, namely: i) the injection nozzle distortion around $Z = 0$, ii) the relaxation-expansion transition around Z_T, and iii) the PB to Node transition at l_1.

In order to address R dependence during fitting, it was necessary to apply multiple fits of Equation (6.2) to PBs with regions varying significantly in average PB radius. This is a consequence of the discrete nature of Equation (6.2), which assumes constant values for all

of the variables contained within the fitting region. In reality, a perfect fit to any real PB system would require the division of the PB into an infinite number of sections with an infinite number of solutions, however; this would obviously be impractical for experimental purposes. Instead, the criteria of an R-Squared value greater than 0.9 was used to designate a 'good' fit of a solution to a region of the PB geometry. This criterion meant that a maximum of four solutions to Equation (6.2) could provide a 'good' fit to the full length of any observed PB geometry. Note that these solutions neglected the distortion regions (i) and (ii) shown in Figure 6.2.

The approximation of constant variables within each discrete fitting region of the PB has some important physical implications, particularly with regard to the assumption of constant surface tension. Using this method, it is possible to determine magnitudes and changes in surface tension over the length of the vertical PB based discrete changes in γ for each fitting region. However, as the overall gradient in surface tension, $\nabla\gamma$, is neglected, this model also neglects contributions due to Marangoni stresses that would arise from these gradients. While the variations in γ are expected to be small for the systems that will be studied here, this is an important point for future studies, wherein a dynamic version of Equation (6.2) will be required in order to account for these effects.

6.1.2.2 Dynamic Surface Tension as a Model Parameter

In order to identify the potential impact of liquid flow rates, Q, on the DST in these isolated PB systems, it is necessary to determine whether surfactant transport to the interface is dominated by convection or diffusion. Only then can an appropriate model describing surfactant adsorption rates be selected.

In the case of immobile PB interfaces, the geometry of the channel cross-section is such that the Péclet number would be expected to vary between diffusion dominated and convection dominated surfactant transport depending on position (i.e. Péclet numbers varying between $P_e \ll 1$ and $P_e \gg 1$ respectively)[33]. This can be simply approximated based on the standard equation $P_e = U_0 H/D_s$ where U_0 describes the fluid velocity relative to the immobile interface, H describes the channel width, and D_s is the diffusion coefficient of the surfactant[33]. The channel width inside an ideal Plateau border with thin films varies between $0 < H \leq \left(\sqrt{3}-1\right)R$ giving a maximum range of $0 < P_e < u\left(\sqrt{3}-1\right)R/D_s$. Approximating u based on the cross-sectional average shown in Equation (6.8), and with maximum flow rates $Q = (\vartheta)10^{-12}$, minimum radii, $R = (\vartheta)10^{-5}$, and minimum surfactant diffusivity, $D_s = (\vartheta)10^{-12}$, yields a maximum range of $0 < P_e < (\vartheta)10^{5}$.

Despite the significant potential variation between convective and diffusive surfactant transport shown, the case of an immobile interface is far from that expected for highly mobile, soluble LMWS species such as Tween and Sodium Dodecyl Sulfate (SDS) [10,14,20,34]. In these cases, the dominant flow profile is expected to be plug-flow, where $U_0 \to 0$ (i.e. a stationary mode) as perfect plug-flow is approached. In this limiting case therefore, diffusion would be expected to be the dominant mode of surfactant transport. Indeed, in the majority of literature describing adsorption of LMWS systems, diffusion is found to be the dominant mode[20], with diffusion coefficients measured based on this finding[22].

While a far more in depth treatment of this problem is possible by solving the convective diffusion equation for the PB system, the treatment above was deemed sufficient for the purpose of this study using highly mobile LMWS systems exhibiting Plug-like flow[10,14]. As

such, the Ward-Tordai (W-T) model for diffusion-controlled adsorption was adopted, which has been previously applied to successfully describe the kinetics of ionic surfactants with high surface concentrations[19].

The expressions describing the W-T model used here are given by Equations (6.9) and (6.10), expressing the short-time and the long-time approximation regions with ideal ionic activity (IIA) correction, respectively[19,35].

$$\gamma_{ST}(t) = \gamma_0 - 2C_0R_gT\sqrt{D_st/\pi} \qquad \text{Short Time Approximation} \qquad (6.9)$$

$$\gamma_{LT}(t) = \gamma_e + nR_gT\left(\frac{{\Gamma_e}^2}{C_0}\right)\sqrt{\frac{\pi}{4D_st}} \qquad \text{Long Time Approximation with IIA Correction} \qquad (6.10)$$

The surface tensions, γ_0 and γ_e, describe the pure solvent surface tension (in this case water) and the equilibrium surface tension of the surfactant solution with concentration, C_0, respectively. The molar gas constant is denoted by R_g, while the temperature is given by T. The equilibrium surface excess, Γ_e, describes the equilibrium concentration of surfactant at the air-water interface, and can be influenced by the electrostatic interactions of charged species. The correction factor, n, was introduced to the W-T long time approximation by Kinoshita*, et al.*[19] in order to account for the action of ionic surfactants. For non-ionic surfactants (e.g. Polysorbates) $n = 1$, whereas for a univalent ionic surfactant in the absence of supporting electrolyte (e.g. SDS in aqueous solution) $n = 2$. No IIA corrected form of the W-T short time approximation is currently available in the literature; however, such a derivation would only be required for the analysis of charged species in their short time region. As the only charged species analysed in this study was SDS, it will be shown that its very small

short time approximation region ($t \ll 10\text{ms}$)[19] meant that only the IIA corrected long time approximation was required in this case.

Having identified a suitable models of surfactant diffusion, it was necessary to identify a means of measuring values for t that could be used in conjunction with the fitting of Equation (6.2) to measured PB profiles. Given that the fitting of Equation (6.2) required PB profiles to be broken down into discrete regions with constant surface tension, it was therefore necessary to measure an average value for t over each discrete profile section.

When surfactant solution is injected at constant Q directly into the PB at $Z = 0$, the resulting average velocity in a given PB section is dependent upon that region's average radius, i.e. $V = \bar{u}(R = \bar{R})$. Therefore, for a surfactant molecule travelling with the bulk liquid, its average residence time in that PB region, τ_{Res}, can be approximated by the distance over velocity relationship shown in Equation (6.11).

$$\tau_{Res} \approx {c\bar{R}^2 Z}/{Q} \tag{6.11}$$

While Equation (6.11) is a suitable approximation for a PB with an ideal cross-section (see Figure 6.1c), this is not the case for the systems studied here. Instead, the PB cross-section becomes ill-defined as it approaches the liquid injection nozzle at $Z = 0$, transitioning from an ideal geometry to an approximately cylindrical one[14,17] over a distance, Z_D (See Figure 6.3).

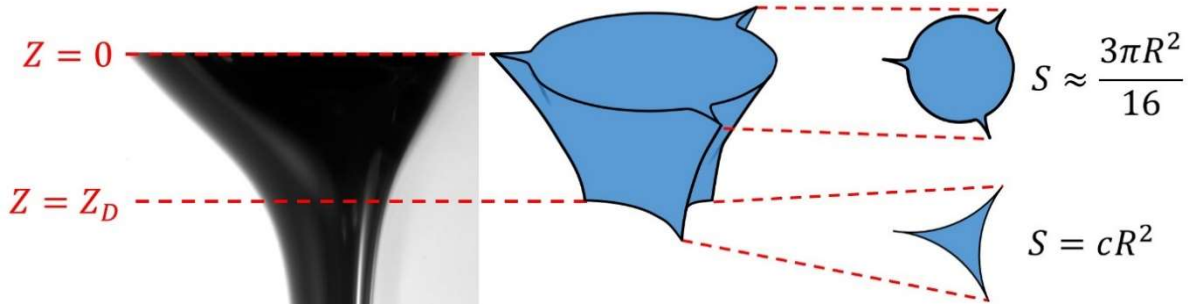

Figure 6.3. Characterisation of PB distortion between $Z = 0$ and $Z = Z_D$, where PB geometry transitions from an approximately circular to an ideal PB cross-section. Left – Image of PB distortion. Right – Schematics of the corresponding 2D and 3D cross-section geometries.

In order to account for this effect, Equation (6.11) was amended to Equation (6.12), giving equal weight to the ideal and cylindrical geometries in the distortion region. PB radii in the distortion region were given the notation R_D.

$$\tau_{Res} \approx \frac{c\bar{R}^2}{Q}(Z - Z_D) + \left(\frac{\overline{R_D}^2(16c+3\ )}{32Q}\right)Z_D \qquad (6.12)$$

Using the approximation that $t = \tau_{Res}$, values for $\gamma_{ST}(\tau_{Res})$ and $\gamma_{LT}(\tau_{Res})$ can be calculated using literature values of D_s and Γ_e from Equations (6.9) and (6.10). The best approximation for $\gamma(\tau_{Res})$ was then based on the minimum of the two values, such that $\gamma(\tau_{Res}) = \min[\gamma_{ST}(\tau_{Res}), \gamma_{LT}(\tau_{Res})]$. As can be seen in the example for an aqueous solution of Tween 20 in Figure 6.4, this produced a natural transition between short and long time approximations at the crossover of Equations (6.9) and (6.10). At times below the crossover, DST was described by γ_{ST}, while above the crossover DST was described by γ_{LT}.

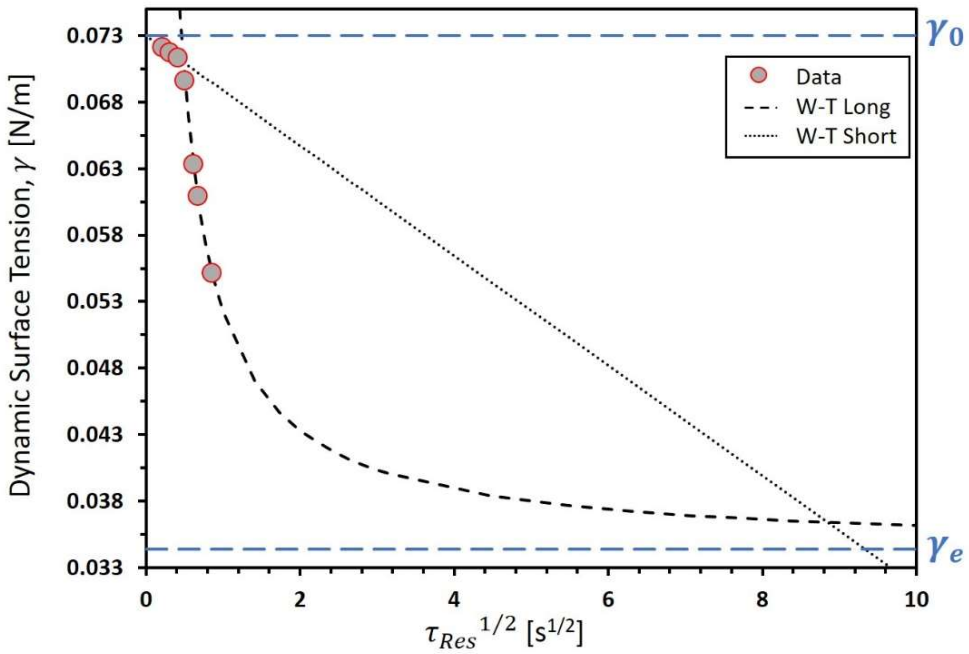

Figure 6.4. Example of short time and long-time with IIA W-T approximations of DST for an uncharged surfactant species (Tween 20). Examples of estimated values were taken based on $\gamma(\tau_{Res}) = \min[\gamma_{ST}(\tau_{Res}), \gamma_{LT}(\tau_{Res})]$. Maximum and minimum values of surface tension are given by the surface tension of water, γ_0, and the equilibrium surface tension, γ_e, respectively.

6.1.2.3 PB Surface Viscosity

Chapters 4 and 5 have consistently indicated that PB surface viscosity for LMWS systems exhibits a significant degree of surface shear thinning. Indeed, such a result has also been suggested by Gauchet*, et al.*[18] to account for their findings in addition to potentially be responsible for the large variation in literature values for SDS surface viscosity. Chapter 5 proposed this to be a consequence of variations in the PB surface tension, however; results counterintuitively indicated that surface shear viscosity *decreased* with *increasing* interfacial surfactant concentration[10]. In order to address whether the theory proposed here was able

to account for this behaviour, it was necessary to calculate the surface viscosity, μ_s, and average liquid shear rate, $\bar{\dot{\gamma}}_s$.

PB surface viscosity can be calculated for an equilibrium PB by combining Equations (6.4), (6.13) and (6.14)[10,14].

$$D^{-1} = c\left[0.02 + \frac{0.0655\ {}_0{}^{-0.5}}{0.209 + B_0{}^{0.628}}\right] \tag{6.13}$$

$$\mu_s = B_0 \mu R \qquad \text{(with } R = R_e\text{)} \tag{6.14}$$

Equation (6.13) is the phenomenological expression proposed by Nguyen[36] to calculate the dimensionless Boussinesq Number, B_0, from the viscous flow parameter, D. Subsequently, B_0 can be converted into its dimensional counterpart, the surface viscosity, using the dynamic bulk viscosity, μ, via Equation (6.14). In previous studies, Equation (6.14) is presented in an alternative form, $M = \mu R/\mu_s$, where the dimensionless parameter, M, was one of four dimensionless groups first derived by Leonard*, et al.*[37] as a solution to the velocity profile through a Plateau border. This parameter was later described as the relative surface mobility by Kraynik[38] who noted that: 'the use of surface viscosity to describe interfacial mobility should not be viewed as exact because the Boussinesq surface fluid is a relatively simple model of the interfacial region'. Subsequently, B_0 has been used to describe the inverse of the relative surface mobility[17,36] thereby yielding the form of Equation (6.14) presented here.

In order to better understand the relationship between PB surface tension and μ_s, the dependence of surface tension on PB radius first had to be taken into account. As Equations (6.13) and (6.14) are only valid under equilibrium PB conditions (i.e. $\mu_s(R = R_e)$), it follows that a direct link to surface tension can only be made for the case $\gamma(R = R_e)$. However, as the

'infinite' PB geometry, $R = R_e$, is a theoretical ideal case, only approximations of the relationship between surface tension and surface viscosity could be made here. Therefore, only fitted surface tensions extracted from PB regions where the minimum radius, R_{min}, approached the corresponding fitted R_e (i.e. $\gamma(R_{min} \rightarrow R_e)$), were deemed suitable for analysis in this instance.

Calculation of the average shear rates through equilibrium PB were undertaken using the approximation[17] shown below:

$$\bar{\dot{\gamma}_S} \approx \frac{Q}{cR_e{}^3} \tag{6.15}$$

6.2 Experimental

6.2.1 Preparation of Surfactant Solutions

SDS (>99.9%) from Fisher Scientific (Loughborough, UK), Tween® 20 and Tween® 80 from Sigma-Aldrich (UK), were weighed and magnetically stirred at room temperature with 15.0MΩ·cm purified water. Stirring continued for a minimum of 30 minutes prior to use of the solution to ensure the complete dissolution of surfactant.

These surfactants represent both charged (SDS) and non-ionic (T20/T80) species that are commercially significant and have therefore been well studied in literature[19,20,22,34,39-42]. Despite some variation in reported values of D_s and Γ_e due to variations in the composition of Tween systems and the presence of impurities in SDS, these surfactants were still deemed the most suitable for the present study. This was partially due to the bulk of available literature examining their adsorption dynamics, but also in order to directly compare the findings of the

revised analysis presented here with those in previous studies using this experimental setup[10,14]. Furthermore, the substantial difference in critical micelle concentration (CMC)[42,43] and rates of adsorption[19,22] between the Tweens and SDS were expected to yield observable differences in PB behaviour. It should be noted however, that in order to improve the precision of the current technique in future studies it will be necessary to select surfactants with highly consistent purity and composition.

6.2.2 Characterisation of Surfactant Solutions

Each surfactant solution was studied at two different concentrations (see Table 1). Concentrations of SDS were chosen to represent ~2× and ~20× the CMC according to literature values[22,42-44], however it was necessary to amend this to ~10× and ~20× the CMCs of T20 and T80 due to the poor PB stability in the experimental setup at lower concentrations. Furthermore, these high concentrations would have been expected to dramatically reduce the impact of the characteristic adsorption times, τ_γ, of surfactant at the PB interface, where $\tau_\gamma = {\Gamma_m}^2/{C_0}^2 D_s$, with Γ_m representing the limiting surface excess[45].

Values for D_s and Γ_e of each surfactant were taken from representative values produced by dedicated experimental studies of DST in literature[19,22]. These values can also be found in Table 1, where it can be seen that the diffusion coefficients for SDS were approximately 100× larger than those for the Tween systems, suggesting much faster rates of SDS adsorption than Tween adsorption. It should be noted here that the decreasing values of D_s with increasing surfactant concentration made by Bąk*, et al.*[22] for the Tweens is in agreement with observations made by other authors for different non-ionic surfactants[46-49]. This decrease is most likely due to the increasing number of micelles formed with increasing surfactant

concentration above the CMC[50], where monomer exchange with micelles increasingly dominates over monomer diffusion to the interface[51].

Surfactant	C_0 [mM]	Γ_e [mol/m^2]	n	D_s [m^{2}s^{-1}]
Tween® 20[22]	0.61	3.50×10^{-6}	1	7.00×10^{-12}
	1.22	3.50×10^{-6}	1	1.50×10^{-12}
Tween® 80[22]	0.15	2.20×10^{-6}	1	10.00×10^{-12}
	0.30	2.20×10^{-6}	1	2.00×10^{-12}
SDS[19]	17.40	6.75×10^{-6}	2	5.30×10^{-10}
	182.00	6.75×10^{-6}	2	5.30×10^{-10}

Table 6.1. Characterisation of surfactant property variables for aqueous solutions of T20, T80 and SDS based on representative literature values[19,22].

A Krüss Processor® Tensiometer K100 (Krüss GmbH, Germany) with density hook attachment and silicon density standard was used to measure liquid density, while surface tension was measured using a Wilhelmy Plate attachment. The solution dynamic viscosity was measured using a Malvern Kinexus® Pro rheometer (Malvern Panalytical, UK) with Double-Gap geometry, which provided excellent measurement sensitivity for the low viscosity solutions studied here. All measurements were carried out at $T = 295$K, and presented data are average values with absolute errors of one standard deviation.

6.2.3 The PB-Node Setup

In order to create the isolated PB's required for analysis at controlled liquid flow rates, the isolated PB-Node setup of Clarke*, et al.*[14] was used. More details of this setup can be found in literature[10,14], however it relies on the principle of a closed tripod frame that can be

withdrawn from surfactant solution to produce and arrangement of liquid films that terminate in a spatially 'ideal' PB and node (see Figure 6.5). PBs were directly injected with additional surfactant solution at controlled liquid flow rates (20µl/min $\leq Q \leq$ 180µl/min) and imaged, to create geometric PB profiles of PB radius, R, vs. height below the liquid injection nozzle, 0 $\leq Z \leq l_1$ (see Figure 6.2).

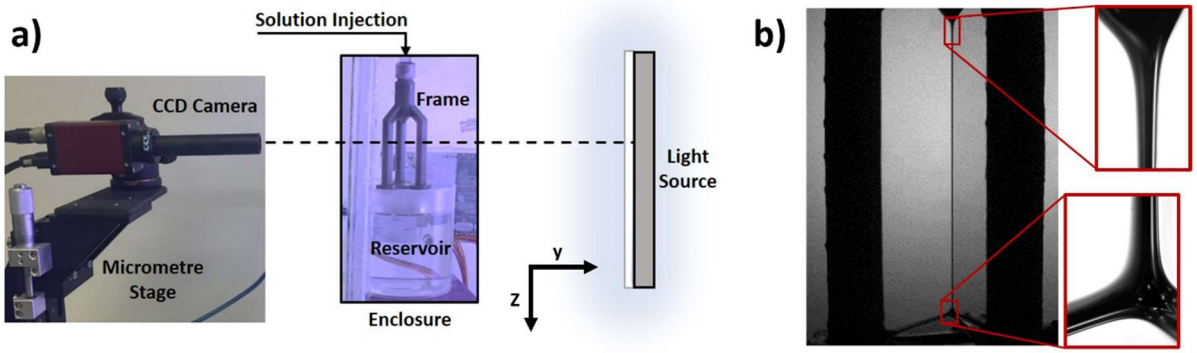

Figure 6.5. The isolated PB-Node setup of Clarke*, et al.*[14]. a) Imaging setup showing camera, frame setup and rear light source. b) Images of PB/node profiles at different magnifications, with the highest resolution of 1.5µm per image pixel. Reprinted with permission from C. Clarke, A Lazidis, F Spyropoulos, and I. T. Norton, "Measuring the impact of channel length on liquid flow through an ideal plateau border and node system," Soft Matter 15, 1879–1889 (2019). Copyright 2019 The Royal Society of Chemistry.

6.2.4 Model Fitting

Due to difficulties in utilising automated fitting methods, as discussed in previous work[10], manual fitting of Equation (6.2) to PB profile sections was able to consistently produce good agreement between theory and experimental data.

Measured PB profiles were divided into a maximum of four fitting regions, based on a coverage of the PB profile from $0 \leq Z \leq l_1$ with a minimum R^2 value of 0.9 being required for each solution. These solutions did not include the distortion regions (i) and (ii) in Figure 6.2 as discussed above. Examples of dividing PB profiles into fitting regions in order to calculate their respective surfactant residence times, τ_{Res}, is shown in Figure 6.6.

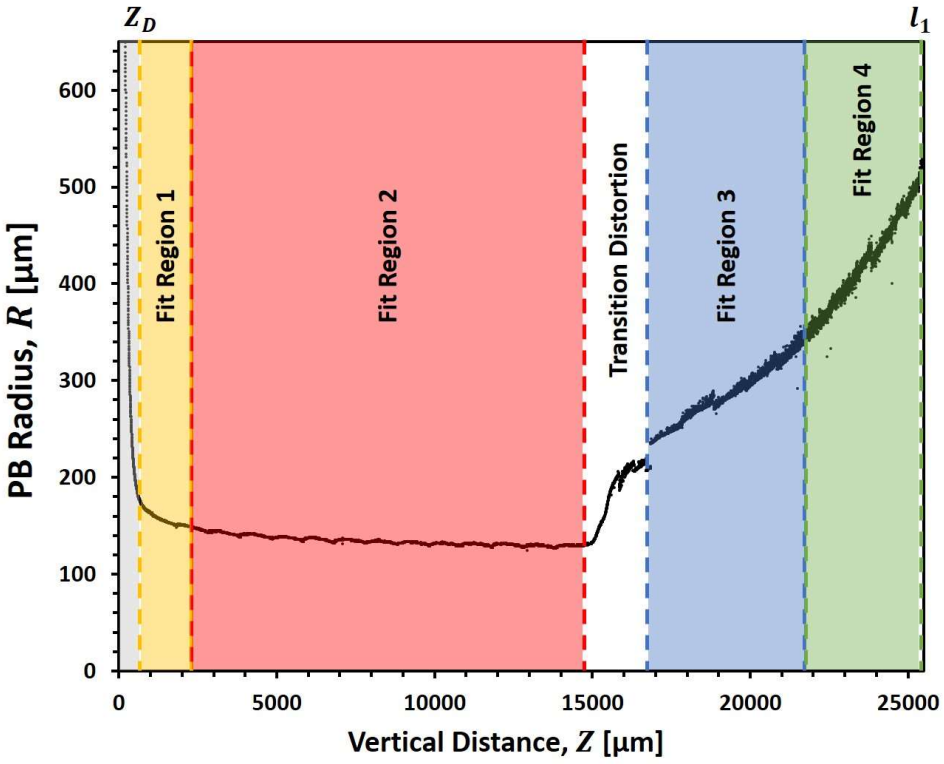

Figure 6.6. Example of PB profile divided into PBs fitting regions to calculate their respective surfactant residence times, τ_{Res}.

6.3 Results

6.3.1 Solution Properties

The measured surfactant solution parameters as well as those taken from representative literature are presented in Table 2. As anticipated, the dynamic viscosity of solutions was only

slightly higher than that of pure water at ~8.9×10^{-4} Pa·s at 25°C[52]. Values for the equilibrium surface tension were in good agreement with those found in existing literature[19,22,44,53-56]. This provided increased confidence that the literature values[19,22] for Γ_e and D_s in Table 1 were reasonable representations of the surfactant behaviour in this study. A trend of decreasing surface tension with increasing surfactant concentration above the CMC was observed for all surfactants, however this variation was within the measurement errors shown for the tween systems and is often seen in literature for SDS systems[19,44,56]. This may represent the effect of trace impurities (e.g. lauryl alcohol), which are common in SDS systems. However, as the measured SDS surface tensions were almost identical to those measured by Kinoshita*, et al.*[19] from which Γ_e and D_s were taken, these were still determined to be a good representation of the system in this study.

6.3.2 Relaxation-Expansion Model

Fitting of Equation 2 to PB profiles was carried out in accordance to the theory and procedure outlined above. A maximum of four fits was applied to any one PB profile, providing an excellent description of its geometry. Average R^2 values were consistently in excess of 0.9 for all liquid flow rates. This marked a significant improvement on previous fit quality[10], where flow profiles transitioning between types in Figure 6.1a and 1b were poorly characterised. Figure 6.7 shows the fits applied to profiles of 17.4mM SDS, 0.61mM T20 and 0.15mM T80 at $Q = 20$µl/min and $Q = 100$µl/min, with corresponding values for the inertial flow parameter, I, shown.

	Surfactant Concentration [mM]	**Density [mg/ml]**	**Viscosity [Pa·s] (10^{-4})**	**Equilibrium Surface Tension [mN/m]**
Tween® 20	0.61	997.70 ± 0.30	9.56 ± 0.07	36.3 ± 0.2
Tween® 20	1.22	997.90 ± 0.10	10.23 ± 0.48	35.9 ± 0.5
Tween® 80	0.15	997.90 ± 0.10	8.84 ± 0.03	40.0 ± 0.5
Tween® 80	0.30	997.60 ± 0.40	9.69 ± 0.23	39.2 ± 0.5
SDS	17.40	998.70 ± 0.90	9.84 ± 0.05	37.9 ± 0.1
SDS	182.00	1005.00 ± 0.50	13.65 ± 0.14	35.4 ± 0.1

Table 6.2. Averaged measurements of surfactant solution bulk and surface properties.

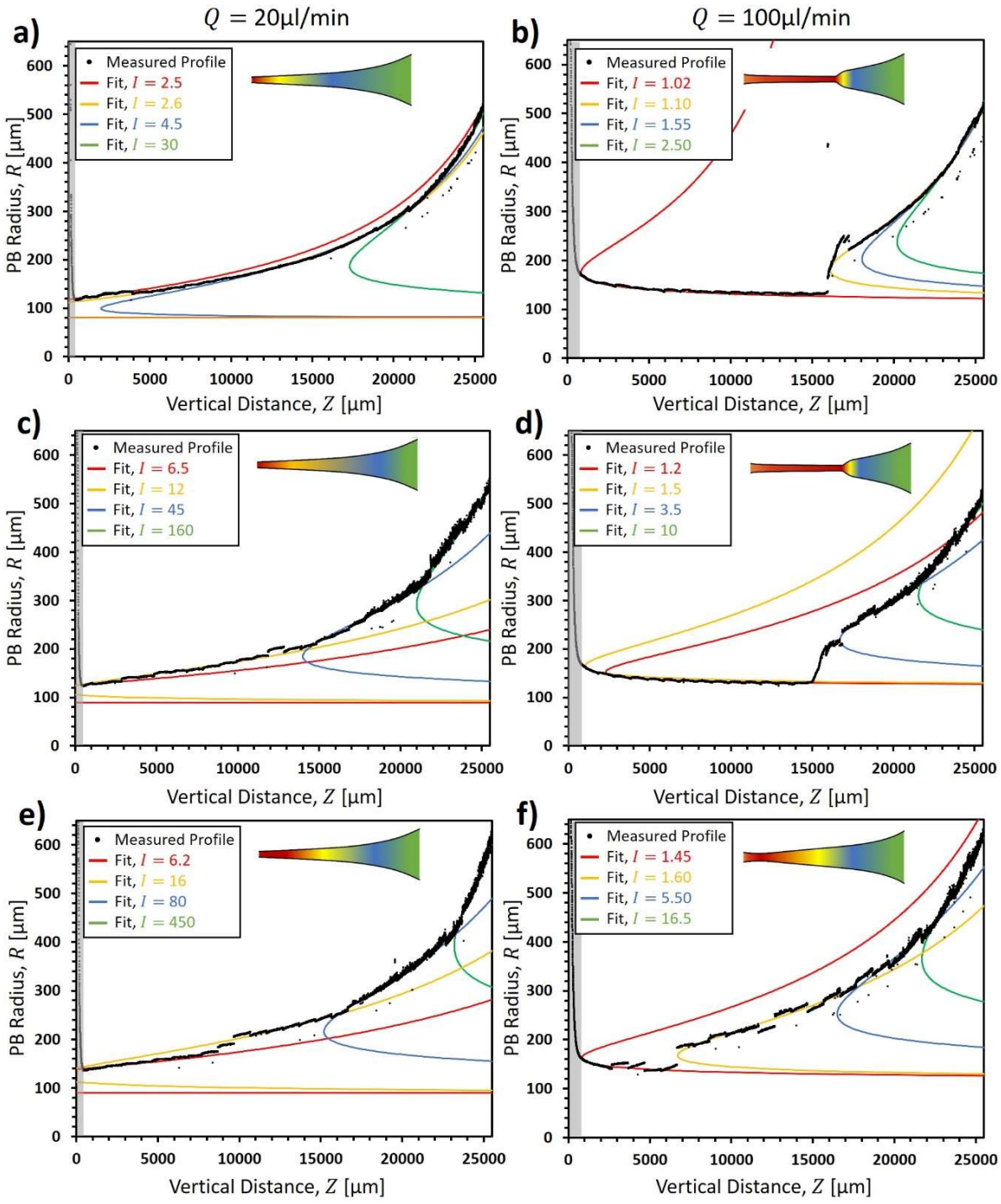

Figure 6.7. Fits of Equation (6.2) to PB profiles for: a), b) 17.4mM SDS; c), d) 0.61mM T20; and e), f) 0.15mM T80. a), c) and e) are for liquid flow rates of Q = 20µl/min. b), d) and f) are for liquid flow rates of Q = 100µl/min. Inset diagrams provide visualisations of the behaviour of I along the equivalent vertical PB cross-sections.

6.3.3 Inertial Flow Parameter

Values for the inertial flow parameter, I, were shown to exhibit a strong linear relationship with $1/V^2$, taking the form $I = (m/V^2) + 1$ with m being the gradient of the straight line (see Figure 6.8). This appeared to reflect the $1/u^2$ dependence of I in Equation (6.7). The intercept of 1 is a key physical limit of, I, where the relationship measured here of $I \to 1$ as $D \to 0$ represents the tendency of these systems towards ideal plug-flow through the PB. This was in line with the expected behaviour of high mobility surfactants.[34,57] Little discernible difference was observed in these relationships due to bulk surfactant concentration; however, a clear difference in gradient was seen between the Tween and SDS systems. The average gradient of SDS solutions compared to that of Tween solutions was $m = 0.003$ and $m = 0.037$ respectively, suggesting flow profiles of Tween systems to be more Poiseuille-like than SDS.

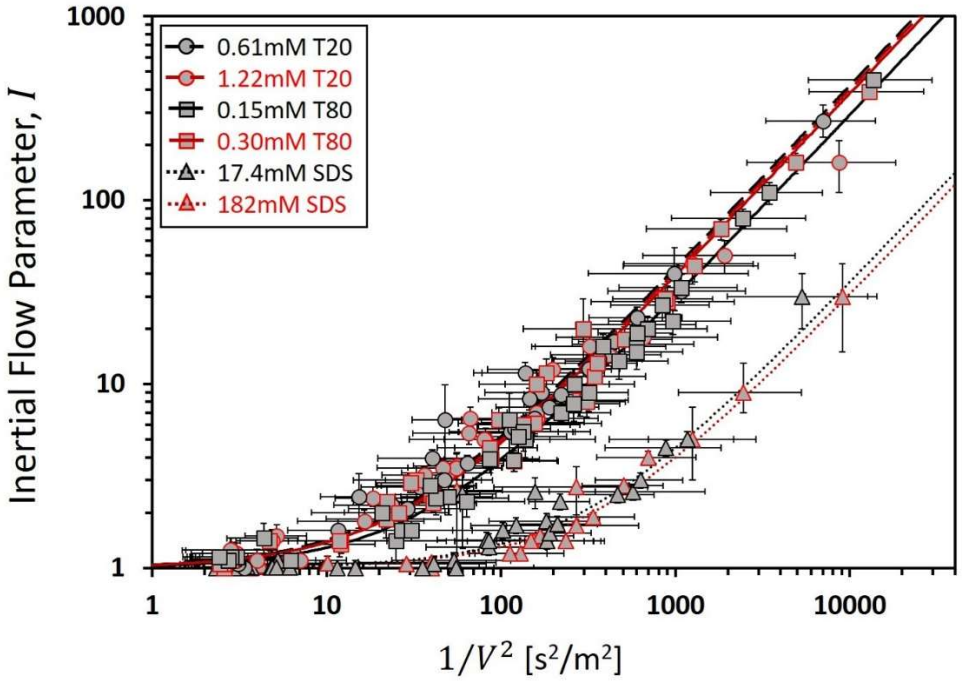

Figure 6.8. Values of the inertial flow parameter, I, as a function of the inverse square of the average flow velocity in the fitting region, $1/V^2$. Linear fits to data take the form of $I = (m/V^2) + 1$ where m is the gradient of the straight line.

6.3.4 Dynamic PB Surface Tension

PB residence times were calculated as outlined above, and then used to calculate PB DST using Equations (6.9) and (6.10), with $t = \tau_{Res}$. As SDS has been extensively studied using other experimental techniques, it was possible to directly compare the DST values calculated here with those measured in literature[19,20]. DST calculated for 17.4mM SDS was the most comparable, with measured literature DST available for 15mM and 10mM samples. This showed a very strong agreement (see Figure 6.9) and confirmed that only the IIA corrected form of the W-T long time approximation (i.e. Equation (6.10)) was required for this study.

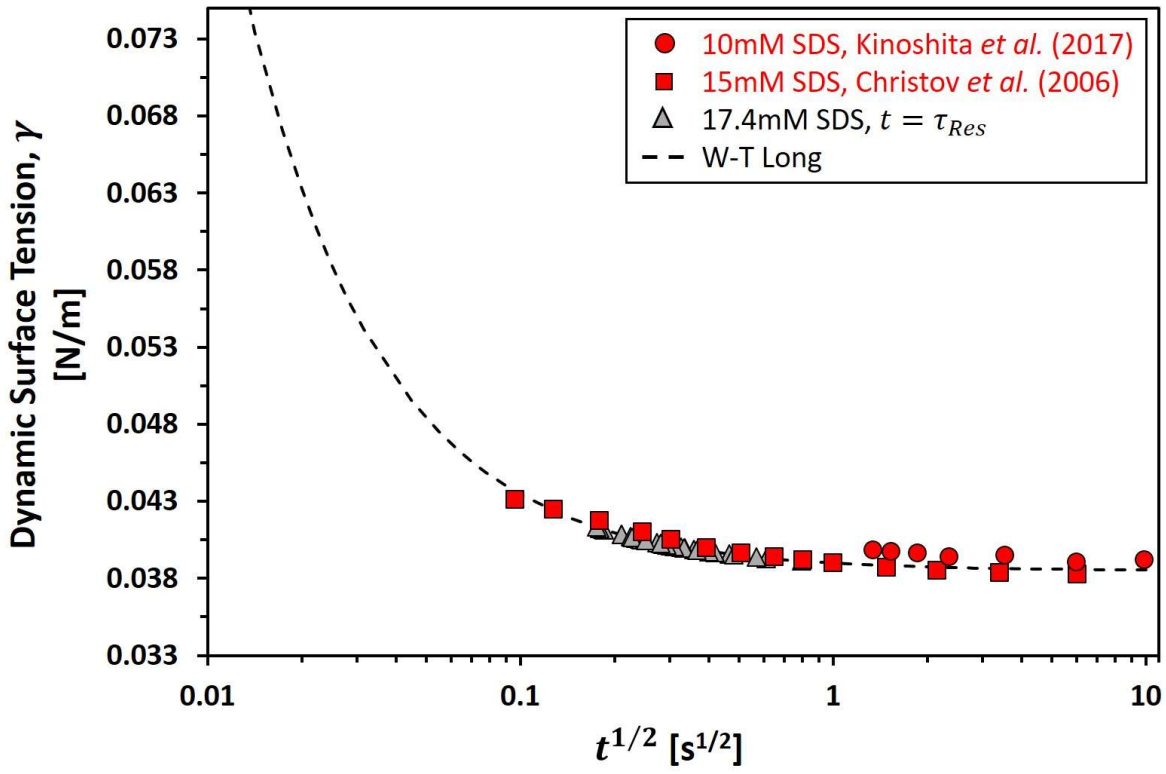

Figure 6.9. Comparison of calculated DST, γ, of 17.4mM SDS using the W-T long time approximation with IIA correction with $t = \tau_{Res}$, in comparison to experimental values for 10mM SDS[19] and 15mM SDS[20] from existing literature.

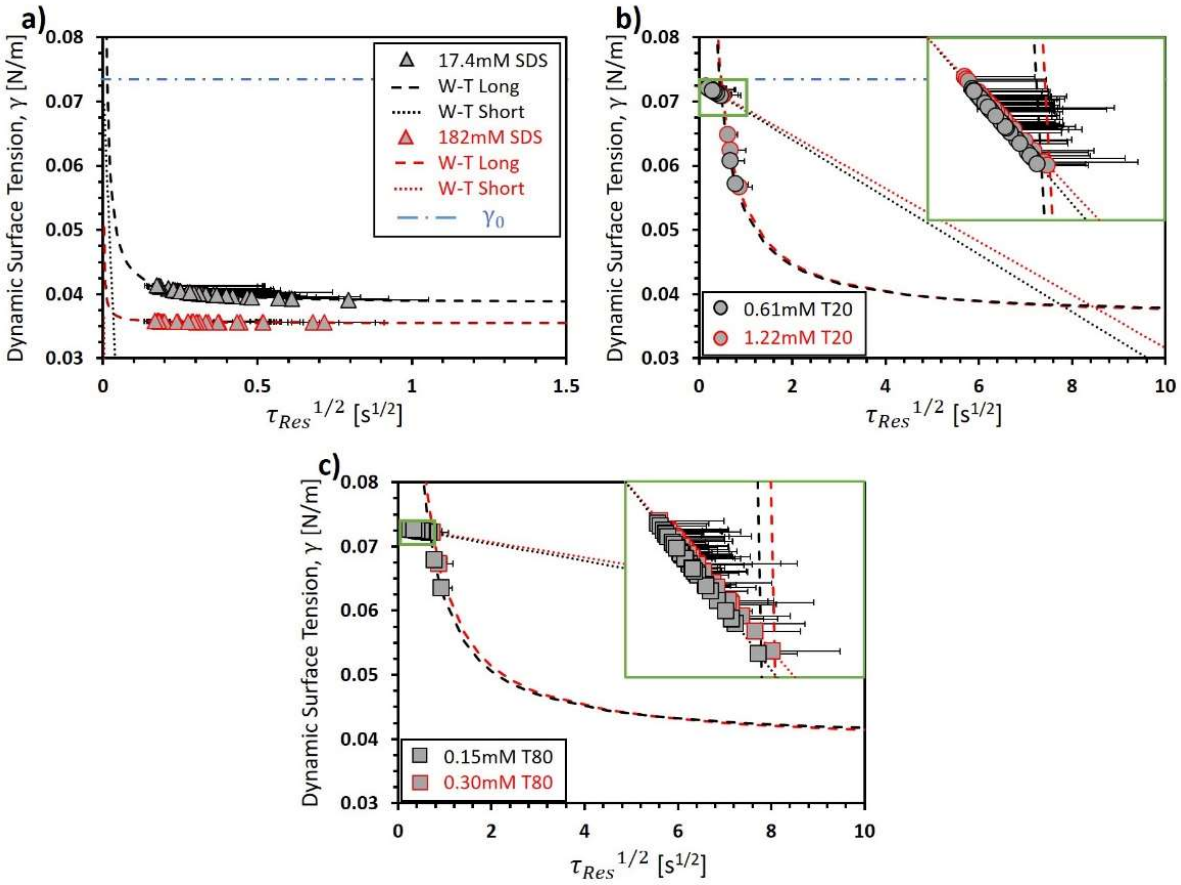

Figure 6.10. Calculated DST, γ, of a) SDS, b) T20 and c) T80 based on the average PB residence time of surfactant molecules, τ_{Res}. Errors are not shown for γ, as values would follow the lines of the W-T long and short time approximations shown for any changes in $\tau_{Res}{}^{1/2}$.

Figure 6.10 highlights the dramatic differences between γ for SDS and Tween solutions, which result from the faster adsorption rates of SDS. While SDS approached γ_e within its PB residence times ($\gamma \rightarrow \gamma_e$), the Tween systems at many Q's remained closer to the surface tension of pure water ($\gamma \rightarrow \gamma_0$). This implied that for high fluid velocities, the rate of adsorption of T20 and T80 resulted in poor surfactant coverage of the PB interface. Indeed, this would explain why lower concentrations of Tweens than those used here were unable to

produce stable PBs for analysis, and why even at higher concentrations, PBs of both T20 and T80 were more prone to collapse than those of SDS.

When discussing PB stability, it must be remembered that the collapse of these systems is primarily attributed to the rupture of films adjoining the PB rather than the breaking of the PB itself. As the liquid flow rates through adjoining films are generally considered significantly smaller than those through PBs[58], it could be expected that surfactant residence time in these films was higher and thereby resulted in lower film surface tension. In this instance, one would expect the presence of Gibbs Marangoni forces due to the resulting concentration gradient of surfactant between film and PB interfaces[59]. The questions concerning stability therefore, relate to the extent of this concentration gradient and the rate at which surfactants could diffuse from the adjoining film interfaces to those of the PB. When one considers that film drainage has also been shown to result in 'younger' interfaces, the suggestion is that in the very early stages of foam drainage, slower adsorbing LMWS may provide little contribution to foam stability. Answering such questions is beyond the scope of the current study, however could be highly relevant in assessing foamability and short timescale stability of LMWS foams.

It has already been noted that the assumption of homogeneous surface tension in each of the separate PB fitting regions prevents an analysis that includes Gibbs-Marangoni Effects in this instance. However, it is clear from Figure 6.10 that the variation in surfactant residence times calculated here would be expected to result in vertical surface tension gradients, $\nabla\gamma$, along the PB. Indeed, this was seen from the differences in surface tension between neighbouring sections of PB. As the surface coverage of the PB increases with increasing Z (i.e. increasing t), the resulting Marangoni stresses would be expected to oppose the concentration gradient,

therefore opposing liquid flow. In this respect therefore, it would be expected that the role of Marangoni forces would decrease bulk flow velocities adjacent to the interface, thereby increasing surfactant residence times and reducing the surface tension gradient. While the results presented here therefore provide a good indication of the expected magnitudes of PB surface tension, a full dynamic equation describing the PB profile geometry is still required in order to enact precision measurements of the physical parameters described here.

An important issue regarding the calculation of PB surface tensions for PB profiles was the errors involved in calculating timescales, t. As can be seen from Figure 6.10a, the errors in τ_{Res} for SDS would have had little impact on the calculated γ according to the W-T approximations. However, Figure 6.10b shows that the errors in τ_{Res} for T20 and T80 could have resulted in decreases in γ of up to 15%, making this a significant source of error for these systems. As the bulk of the error in τ_{Res} originated from the approximation of the PB geometry between $Z = 0$ and $Z = Z_D$ (see Figure 6.3), this highlights the need for the precise characterisation of the full PB geometry, regardless of the subsequent method of analysis.

6.3.5 PB Surface Viscosity

When comparing γ with PB surface shear viscosity, μ_s, Clarke*, et al.*[10] found the counterintuitive result that μ_s *decreased* with *increasing* surfactant concentration at the interface. Figure 6.11 shows that this was no longer the case when the theory proposed here is applied. The plotted data points represent values extracted from PB fitting regions where the minimum radius was approaching the equilibrium radius (i.e. $R_{min} \rightarrow R_e$). As discussed previously, the closer the values of R_{min} to R_e, the more reliable the visual relationship between γ and μ_s. As such, data points are categorised in to those whose R_{min} were ≤10%

(green), ≤15% (orange) and ≤20% (red) greater than their R_e values, therefore helping to provide an indication of the strength of the trends.

The extrapolation of data trends in Figure 6.11 are clearly largely approximated, however; the purpose here was to show that relationships similar to those observed between surface tension and other surfactant concentration variables (e.g. bulk concentration, surface concentration[19,22]) fit well with the data here. Ultimately, this suggests the far more intuitive result that surface viscosity *increases* with *increasing* surfactant concentration at the PB interface. This relationship exists between the two extremes of a clean air-water interface with a surface viscosity of zero, and a surfactant saturated air-water interface with a corresponding maximum surface viscosity depending on the surfactant species. While maximum μ_s for T20 and T80 could not be established based on the data here, the maximum μ_s for SDS was suggested to be $\sim 1 \times 10^{-8}$g/s. This is in line with the previous lower limit set by Clarke*, et al.*[14], as well as the high precision measurements made by Zell*, et al.*[34], whose studies of planar interfaces showed that soluble LMWS systems (including T20 and SDS) had surface viscosities lower than the measurement sensitivity of existing techniques (i.e. $\mu_s < 10^{-5}$g/s).

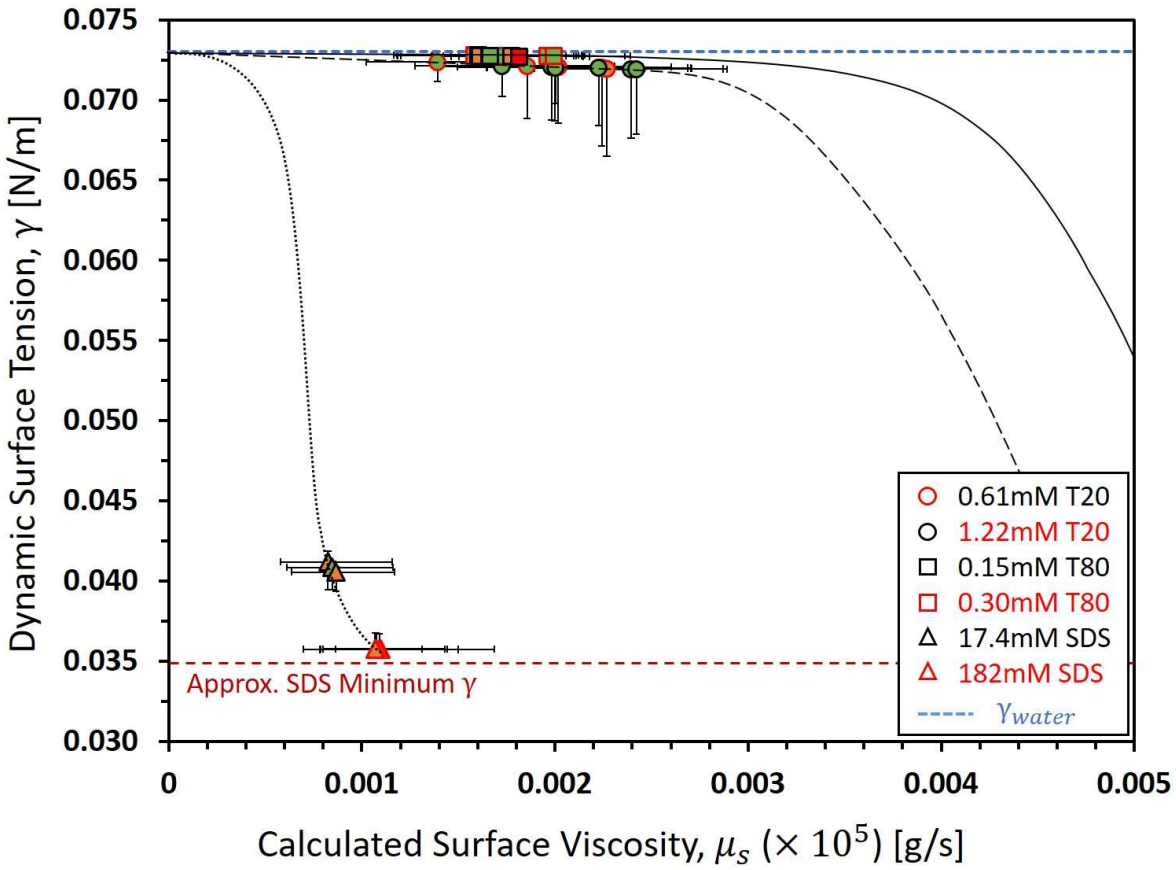

Figure 6.11. Calculated DST, γ, vs. calculated surface viscosity, μ_s, for concentrations of SDS, T20 and T80. Fill colours of data points represent how close values of R_{min} were to R_e with R_{min} ≤+10% (green), ≤ +15% (orange) and ≤ +20% (red). Black lines indicate suggested trends based on standard surface tension vs. surfactant concentration relationships.

It is also clear from the revised theory applied here, that the apparent surface shear thinning observed by Clarke*, et al.*[10],[14] for both SDS and Tween systems was likely to have been largely a result of the restrictions imposed on fitting variables in these cases. Data from this study showed that μ_s was virtually independent of average liquid shear rate at the concentrations and liquid flow rates studied, with any variations in μ_s that did occur being attributed to changes in surface tension (see Figure 6.12).

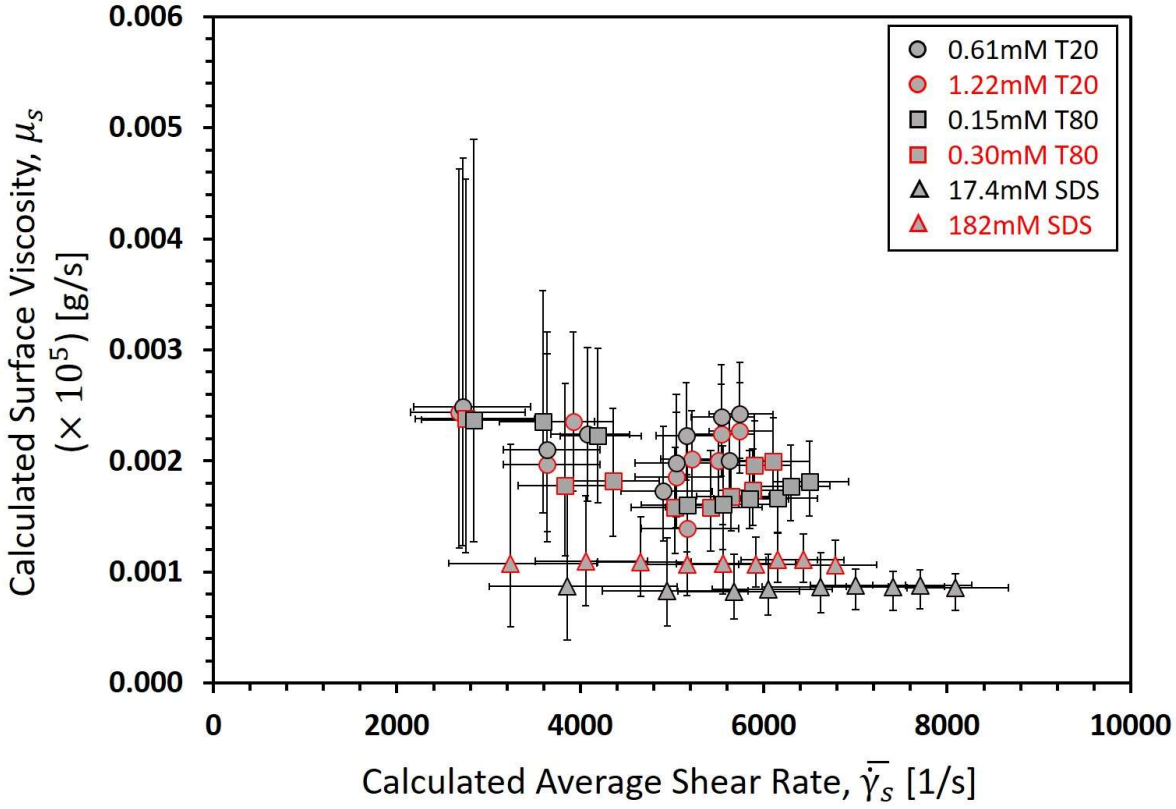

Figure 6.12. Calculated surface viscosity, μ_s, vs. calculated average liquid shear rate, $\overline{\dot{\gamma}_s}$ for SDS, T20 and T80 solutions.

6.4 Conclusions

The novel experimental setup of Clarke*, et al.*[10],[14] was further investigated for the soluble surfactants SDS, T20 and T80. The hypothesis that increasing liquid flow velocity through ideal isolated Plateau borders of a foam microstructure could result in 'younger' PB interfaces was assessed using a novel analytical technique. Analysis of measured PB profiles indicated that the average timescales over which soluble LMWS molecules could reside in the PB were similar to those required for surfactant molecules to diffuse to the air-water interface. As such, the adsorption kinetics of each surfactant were shown to play a major role in the flow rate dependence of PB geometries and their stability.

The liquid flow rates resulting in the highest DST were always in the range 40µl/min$< Q <$100 µl/min, which is within the range of liquid flow rates generally observed during macroscopic foam drainage. This implies that LMWS surfactants with longer adsorption timescales could have detrimental effects on macroscopic foam stability during the early stages of foam drainage. This effect is likely to be compounded by the adjoining 'young' films also formed at this stage[32].

The physical parameters derived from the present model each PB system were consistent with those expected for high mobility LMWS. Liquid flow profiles tended towards plug-flow, with surface shear viscosity for all systems at levels far below the measurement sensitivity of existing direct measurement methods, as proposed by Zell*, et al.*[34]. The increase in surface viscosity increased with surface surfactant concentration, while showing no discernible relationship to liquid shear rate. As such, the refinement of the model and fitting procedure in this study was able to address the counterintuitive findings of previous work[10,14].

The present study demonstrates how the geometric analysis of controlled, isolated, foam systems has the potential to yield precision data regarding their complex and dynamic nature. A static geometric profile solution is able to provide a good description of vertical PB profiles at constant liquid flow rates, however a complete approach requires that the dynamic nature of the interface be taken to account in a dynamic geometric profile equation. Only then can the full potential of this technique be realised.

6.5 References

1 J. Wang; A. V. Nguyen; S. Farrokhpay, A Critical Review of the Growth, Drainage and Collapse of Foams, *Advances in Colloid and Interface Science* **2016**, *228*, 55-70.

2 R. J. Pugh, *Bubble and Foam Chemistry*; Cambridge University Press: Cambridge, United Kingdom, **2016**.

3 E. Dickinson, 6 - Colloidal Systems in Foods Containing Droplets and Bubbles. In *Understanding and Controlling the Microstructure of Complex Foods*, McClements, D. J., Ed. Woodhead Publishing: **2007**; pp 153-184.

4 D. Weaire; S. Hutzler, *The Physics of Foams*; Oxford University Press: New York, **1999**.

5 J. S. Lioumbas; E. Georgiou; M. Kostoglou; T. D. Karapantsios, Foam Free Drainage and Bubbles Size for Surfactant Concentrations Below the Cmc, *Colloids and Surfaces A: Physicochemical and Engineering Aspects* **2015**, *487*, 92-103.

6 O. Pitois; C. Fritz; M. Vignes-Adler, Liquid Drainage through Aqueous Foam: Study of the Flow on the Bubble Scale, *Journal of Colloid and Interface Science* **2005a**, *282*, 458-465.

7 O. Pitois; N. Louvet; E. Lorenceau; F. Rouyer, Node Contribution to the Permeability of Liquid Foams, *Journal of Colloid and Interface Science* **2008**, *322*, 675-677.

8 A. Anazadehsayed; N. Rezaee; J. Naser, Numerical Modelling of Flow through Foam's Node, *Journal of Colloid and Interface Science* **2017**, *504*, 485-491.

9 I. Cantat; S. Cohen-Addad; F. Elias; F. Graner; R. Höhler; O. Pitois; F. Rouyer; A. Saint-Jalmes; S. Cox, *Foams: Structure and Dynamics*; Oxford University Press: New York, **2013**.

10 C. Clarke; F. Spyropoulos; I. T. Norton, Surface Rheological Measurements of Isolated Food Foam Systems, *Physics of Fluids* **2019**, *31*, 092002.

11 M. Durand; D. Langevin, Physicochemical Approach to the Theory of Foam Drainage, *The European Physical Journal E* **2002**, *7*, 35-44.

12 A. Anazadehsayed; N. Rezaee; J. Naser; A. V. Nguyen, A Review of Aqueous Foam in Microscale, *Advances in Colloid and Interface Science* **2018**, *256*, 203-229.

13 D. Weaire; S. Hutzler; G. Verbist; E. Peters; I. Prigogine; S. A. Rice, A Review of Foam Drainage, *Advances in Chemical Physics* **1997**, *102*.

14 C. Clarke; A. Lazidis; F. Spyropoulos; I. T. Norton, Measuring the Impact of Channel Length on Liquid Flow through an Ideal Plateau Border and Node System, *Soft Matter* **2019**, *15*, 1879-1889.

15 O. Pitois; C. Fritz; M. Vignes-Adler, Hydrodynamic Resistance of a Single Foam Channel, *Colloids and Surfaces A: Physicochemical and Engineering Aspects* **2005b**, *261*, 109-114.

16 K. Koczó; G. Rácz, Flow in a Plateau Border, *Colloids and Surfaces* **1987**, *22*, 95-96.

17 F. Elias; E. Janiaud; J.-C. Bacri; B. Andreotti, Elasticity of a Soap Film Junction, *Physics of Fluids* **2014**, *26*, 037101.

18 S. Gauchet; M. Durand; D. Langevin, Foam Drainage. Possible Influence of a Non-Newtonian Surface Shear Viscosity, *Journal of Colloid and Interface Science* **2015**, *449*, 373-376.

19 K. Kinoshita; E. Parra; D. Needham, Adsorption of Ionic Surfactants at Microscopic Air-Water Interfaces Using the Micropipette Interfacial Area-Expansion Method: Measurement of the Diffusion Coefficient and Renormalization of the Mean Ionic Activity for Sds, *Journal of Colloid and Interface Science* **2017**, *504*, 765-779.

20 N. C. Christov; K. D. Danov; P. A. Kralchevsky; K. P. Ananthapadmanabhan; A. Lips, Maximum Bubble Pressure Method: Universal Surface Age and Transport Mechanisms in Surfactant Solutions, *Langmuir* **2006**, *22*, 7528-7542.

21 J. Liu; C. Yang; C. Zhang; U. Messow, Theory of Diffusion-Controlled Adsorption Kinetics at the Expanding Planar Surface with a Constant Area Rate, *Colloid and Polymer Science* **2005**, *284*, 92-96.

22 A. Bąk; W. Podgórska, Interfacial and Surface Tensions of Toluene/Water and Air/Water Systems with Nonionic Surfactants Tween 20 and Tween 80, *Colloids and Surfaces A: Physicochemical and Engineering Aspects* **2016**, *504*, 414-425.

23 O. E. Pérez; C. C. Sánchez; A. M. R. Pilosof; J. M. Rodríguez Patino, Dynamics of Adsorption of Hydroxypropyl Methylcellulose at the Air–Water Interface, *Food Hydrocolloids* **2008**, *22*, 387-402.

24 V. N. Paunov; B. P. Binks; N. P. Ashby, Adsorption of Charged Colloid Particles to Charged Liquid Surfaces, *Langmuir* **2002**, *18*, 6946-6955.

25 C. D. Dushkin; T. H. Iliev; Y. S. Radkov, Dynamic Surface Tension of Micellar Solutions Studied by the Maximum Bubble Pressure Method, *Colloid and Polymer Science* **1995**, *273*, 370-378.

26 V. B. Fainerman; V. D. Mys; A. V. Makievski; J. T. Petkov; R. Miller, Dynamic Surface Tension of Micellar Solutions in the Millisecond and Submillisecond Time Range, *Journal of Colloid and Interface Science* **2006**, *302*, 40-46.

27 B. P. Radoëv; D. S. Dimitrov; I. B. Ivanov, Hydrodynamics of Thin Liquid Films Effect of the Surfactant on the Rate of Thinning, *Colloid and Polymer Science* **1974**, *252*, 50-55.

28 I. B. Ivanov; D. S. Dimitrov, Hydrodynamics of Thin Liquid Films, *Colloid and Polymer Science* **1974**, *252*, 982-990.

29 V. G. Levich, *Physicochemical Hydrodynamics*; Longman Higher Education, **1959**, p 700.

30 L. E. Scriven; C. V. Sternling, The Marangoni Effects, *Nature* **1960**, *187*, 186-188.

31 A. Sheludko, Thin Liquid Films, *Advances in Colloid and Interface Science* **1967**, *1*, 391-464.

32 P. G. de Gennes, "Young" Soap Films, *Langmuir* **2001**, *17*, 2416-2419.

33 Chapter 6 - Transport Processes in Microfluidic Applications. In *Coulson and Richardson's Chemical Engineering (Seventh Edition)*, Chhabra, R.; Shankar, V., Eds. Butterworth-Heinemann: **2018**; pp 529-546.

34 Z. A. Zell; A. Nowbahar; V. Mansard; L. G. Leal; S. S. Deshmukh; J. M. Mecca; C. J. Tucker; T. M. Squires, Surface Shear Inviscidity of Soluble Surfactants, *Proceedings of the National Academy of Sciences* **2014**, *111*, 3677-3682.

35 V. B. Fainerman; A. V. Makievski; R. Miller, The Analysis of Dynamic Surface Tension of Sodium Alkyl Sulphate Solutions, Based on Asymptotic Equations of Adsorption Kinetic Theory, *Colloids and Surfaces A: Physicochemical and Engineering Aspects* **1994**, *87*, 61-75.

36 A. V. Nguyen, Liquid Drainage in Single Plateau Borders of Foam, *Journal of Colloid and Interface Science* **2002**, *249*, 194-199.

37 R. A. Leonard; R. Lemlich, A Study of Interstitial Liquid Flow in Foam. Part I. Theoretical Model and Application to Foam Fractionation, *AIChE Journal* **1965**, *11*, 18-25.

38 A. M. Kraynik *Foam Drainage*; United States, 1983-11-01, 1983.

39 H. Vatanparast; F. Shahabi; A. Bahramian; A. Javadi; R. Miller, The Role of Electrostatic Repulsion on Increasing Surface Activity of Anionic Surfactants in the Presence of Hydrophilic Silica Nanoparticles, *Scientific Reports* **2018**, *8*, 7251.

40 T. J. Vogel. Dynamic Behavior of Self-Assembled Langmuir Films Composed of Soluble Surfactants and Insoluble Amphiphiles. The Ohio State University, 2011.

41 A. Casandra; M.-C. Chung; B. A. Noskov; S.-Y. Lin, Adsorption Kinetics of Sodium Dodecyl Sulfate on Perturbed Air-Water Interfaces, *Colloids and Surfaces A: Physicochemical and Engineering Aspects* **2017**, *518*, 241-248.

42 K. L. Mittal, Determination of Cmc of Polysorbate 20 in Aqueous Solution by Surface Tension Method, *Journal of Pharmaceutical Sciences* **1972**, *61*, 1334-1335.

43 A. Cifuentes; J. L. Bernal; J. C. Diez-Masa, Determination of Critical Micelle Concentration Values Using Capillary Electrophoresis Instrumentation, *Analytical Chemistry* **1997**, *69*, 4271-4274.

44 S.-Y. Lin; Y.-Y. Lin; E.-M. Chen; C.-T. Hsu; C.-C. Kwan, A Study of the Equilibrium Surface Tension and the Critical Micelle Concentration of Mixed Surfactant Solutions, *Langmuir* **1999**, *15*, 4370-4376.

45 E. Nowak; Z. Xie; N. M. Kovalchuk; O. K. Matar; M. J. H. Simmons, Bulk Advection and Interfacial Flows in the Binary Coalescence of Surfactant-Laden and Surfactant-Free Drops, *Soft Matter* **2017**, *13*, 4616-4628.

46 J. G. Göbel; G. R. Joppien, Dynamic Interfacial Tensions of Aqueous Triton X-100 Solutions in Contact with Air, Cyclohexane,N-Heptane, Andn-Hexadecane, *Journal of Colloid and Interface Science* **1997**, *191*, 30-37.

47 B. B. Niraula; T. K. Chun; H. Othman; M. Misran, Dynamic-Interfacial Properties of Dodecyl-B-D-Maltoside and Dodecyl-B-D-Fructofuranosyl-A-D-Glucopyranoside at Dodecane/Water Interface, *Colloids and Surfaces A: Physicochemical and Engineering Aspects* **2004**, *248*, 157-166.

48 U. Teipel; N. Aksel, Adsorption Behavior of Nonionic Surfactants Studied by Drop Volume Technique, *Chemical Engineering & Technology* **2001**, *24*, 393-400.

49 K. Staszak; K. Prochaska, Estimation of Diffusion Coefficients Based on Adsorption Measurements in Model Extraction Systems, *Chemical Engineering & Technology* **2005**, *28*, 985-990.

50 T. M. Ferreira; D. Bernin; D. Topgaard, Chapter Three - Nmr Studies of Nonionic Surfactants. In *Annual Reports on Nmr Spectroscopy*, Webb, G. A., Ed. Academic Press: **2013**; Vol. 79, pp 73-127.

51 R. D. Brazee; M. Bukovac; J. A. Cooper; H. Zhu; D. L. Reichard; R. D. Fox, Surfactant Diffusion and Dynamic Surface Tension in Spray Solutions, *Transactions of the ASAE* **1994**, *37*, 51-58.

52 Anton-Paar Viscosity of Water. https://wiki.anton-paar.com/en/water/ **2008**. (accessed 18/04/2019).

53 I. C. Bellettini; R. Eising; A. C. Felippe; J. B. Domingos; E. Minatti; V. G. Machado, Association of Branched Polyethylene Imine with Surfactants in Aqueous Solution, *Química Nova* **2015**, *38*, 787-793.

54 B. A. Kerwin, Polysorbates 20 and 80 Used in the Formulation of Protein Biotherapeutics: Structure and Degradation Pathways, *J Pharm Sci* **2008**, *97*, 2924-35.

55 M. Milanović; V. Krstonošić; L. Dokic; M. Hadnađev; T. Dapčević Hadnađev, Insight into the Interaction between Carbopol® 940 and Ionic/Nonionic Surfactant, *Journal of Surfactants and Detergents* **2015**, *18*.

56 CR *Characterization of Surfactant Mixtures*; AR204e; Krüss GmbH: 1996; p 9.

57 A. Saint-Jalmes; Y. Zhang; D. Langevin, Quantitative Description of Foam Drainage: Transitions with Surface Mobility, *Eur. Phys. J. E* **2004**, *15*, 53-60.

58 A. Saint-Jalmes, Physical Chemistry in Foam Drainage and Coarsening, *Soft Matter* **2006**, *2*, 836-849.

59 G. J. Elfring; L. G. Leal; T. M. Squires, Surface Viscosity and Marangoni Stresses at Surfactant Laden Interfaces, *Journal of Fluid Mechanics* **2016**, *792*, 712-739.

Chapter 7

A Summary of the Key Conclusions of this Thesis and Recommendations for Future Work

7.1 Conclusions

The development of the experimental protocols and theory that accompany the PB-node setup for studying the geometry of microscale foam channels and their junctions has led to a number of insights. Detailed conclusions presented for the work in each experimental chapter have either been published or are pending publication, however, an overview of the key research findings of this thesis is given here.

7.1.1 The Microscale Geometries of Foam Plateau Borders

I. Fundamental foam channel geometries vary with channel length, liquid flow rate and choice of emulsifier.

Previous studies of isolated foam channels have reported only one fundamental foam channel geometry, wherein a vertical channel gradually expands from its initial height into either an adjoining node or bulk liquid (Figure 7.1a)[1-5]. Present study has demonstrated this channel to be just one end of a spectrum of channel geometries that can exist (Figures 1b &1c), depending on the emulsifier properties, channel length and liquid flow rate[6,7].

II. All of the observed foam channel geometries can be well described by a single solution to the foam drainage equation.

Using the foam drainage equation[8,9] for a vertical, thin-filmed PB, Clarke*, et al.*[7] derived a solution that was able to explain each of the PB profiles shown in Figure 7.1. This solution ultimately showed that PB profiles can exhibit both relaxation and expansion and that the degree to which a profile demonstrates either of these traits is dependent upon the position and geometry of the adjoining node.

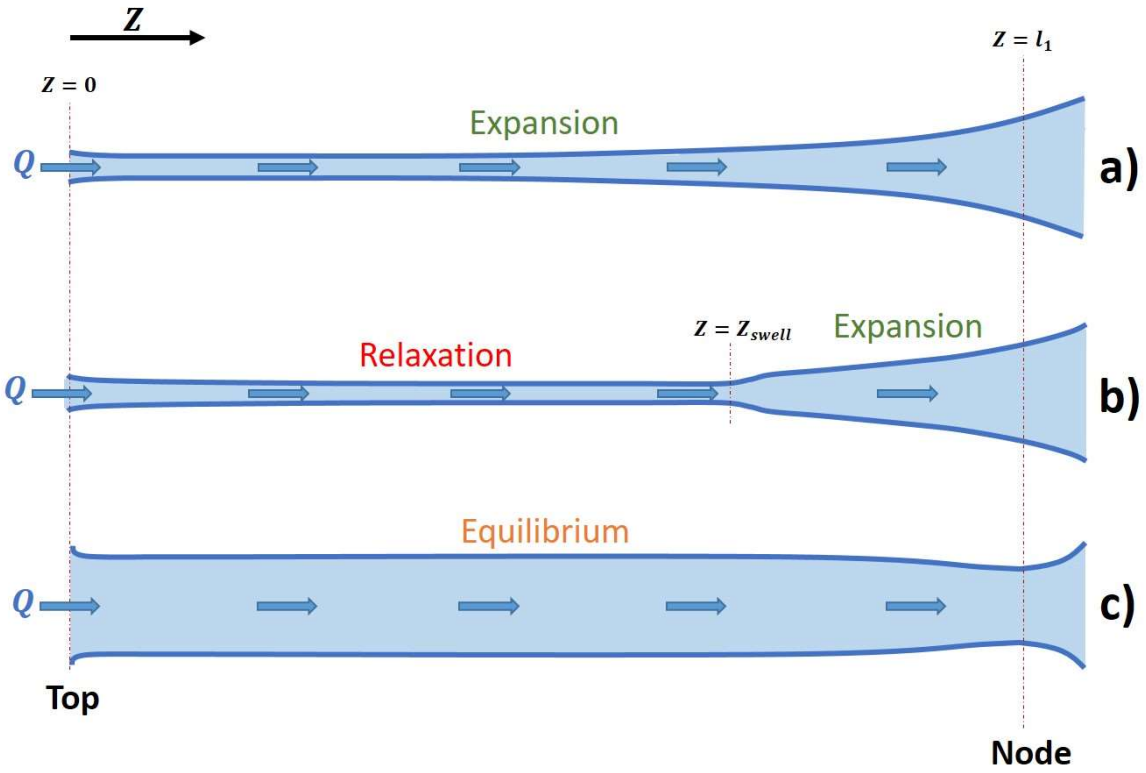

Figure 7.1. Schematics of isolated PB vertical profiles demonstrating: a) The conventional expansion profile; b) The expansion-relaxation profile discovered by Clarke, et al.[6] for LMWS at high liquid flow rates and long PB lengths; c) The equilibrium-contraction profile discovered by Clarke, et al.[7] for high molecular weight emulsifiers.

7.1.2 Flow Dissipation within Foam Channels

III. Viscous and inertial dissipation can vary substantially within a single foam channel depending on the channel length and rate of liquid flow.

The observations made in this thesis suggest that the non-linear profiles of isolated foam channels at constant liquid flow rates can result in significant variations to viscous and inertial flow parameters. The fact that these variations are both flow rate and PB length dependent, suggests that the general simplified assumption of a straight PB with average radius may be

insufficient to correctly characterise these systems in macroscopic foams. Furthermore, it appears that the presence of the node greatly influences the adjoining PB geometry, suggesting that the separate treatment of PBs and nodes to describe macroscopic drainage may also be questionable.

IV. The surface viscosity of an isolated foam channel stabilised by low molecular weight surfactants appears to be substantially lower than that predicted by most commercial surface rheological measurement techniques.

While the theory presented here is only suitable for predicting the surface shear viscosity of foam channels in their equilibrium state, it is clear that these values are substantially lower than predicted by conventional measurement techniques. These findings follow a trend of decreasing surface viscosity for such systems, as measurement sensitivity has increased[10]. The virtually zero values of surface shear viscosity measured here support the assumption of a 'node dominated flow regime' for most LMWS surfactants, wherein viscous dissipation in the foam channels is considered to be negligible in comparison to dissipation within the nodes[10,11].

7.1.3 Foam Channel Surface Tension

V. A non-uniform surface tension is proposed to exist along the foam channel interface. The extent of this effect appears to depend upon the emulsifier adsorption dynamics relative to liquid flow rates.

The theory and observations presented in Chapter 6 suggest the presence of a surface tension gradient along the PB interface that is governed by the rate of surfactant adsorption and the average residence time of surfactant molecules within the PB. Indeed, such a finding has

already been made in the literature for isolated soap films under free drainage conditions[12]. At the constant liquid flow rates provided by the PB-node setup, PB surface tension gradients are sustained and can be studied from the resulting PB geometries fitted with the geometric foam equation derived here. The surface tension was subsequently linked to the surface shear viscosity, where an increased surfactant concentration at the air-liquid interface decreased surface tension while increasing the surface viscosity.

7.2 Recommendations for Future Work

The PB-node setup has so far proven to be capable of making high-resolution measurements of PB geometries under carefully controlled flow conditions. It is the belief of this author that there is still much potential in this experimental setup for conducting additional experimental investigations of microscale foam dynamics. The three studies discussed here represent the most poignant of these potential investigations, with the potential to answer further questions raised by the current research.

I. Study the impact of controlled variation in bulk and surface parameters for LMWS systems such as bulk and surface viscosity.

Initial tests of the PB-node setup have shown it to be capable of measuring foam channel geometries of SDS and Tween 20 with added glucose or glycerol to control the dynamic viscosity of the liquid. As a well-known inhibitor of liquid drainage, studying the impact of increasing liquid viscosity on PB geometries could provide useful information relating to how this affects viscous dissipation and foam channel stability for different surfactants. Similarly, chemically altering the surface viscosity of the channel interface could provide more

information that relates surfactant adsorption dynamics to bulk liquid flow. For example, additions of salts, such as sodium chloride, can substantially alter the bulk and surface properties of SDS. The resulting shielding of the electrostatic repulsion between SDS molecules can increase the CMC and lower the surface tension, as well as changing the shape of the SDS micelles (from spherical to worm-like), altering the bulk viscosity of the system[13]. Furthermore, additions of 1-Dodecanol have been shown by various authors[2,3,14] to dramatically decrease the mobility of SDS at the air-liquid interface.

II. ***Analyse the geometries of isolated nodes using theory analogous to that presented in this thesis for isolated PBs.***

As already discussed, the measurement of surface shear viscosity in the PB-node setup suggests the viscous dissipation within isolated PBs of low molecular weight surfactants to be virtually zero. This implies that the viscous dissipation within the adjoining node must be considerably higher to be in agreement with the theory of a 'node dominated drainage regime' that is usually measured for corresponding macroscopic foam systems. In order to confirm this, it would be prudent to measure the flow rate dependent node geometries for these systems and relate this to their viscous dissipation. As channel or node-dominated drainage regimes ultimately separate and compare the flow dissipation of these structures, the ability to directly study the transition between them could prove valuable. Indeed, it has already been suggested here that the node can dramatically influence the adjoining PB geometry; suggesting a clear-cut distinction between node and PB dissipation is inaccurate.

III. Assess the degree of coupling of PB flow with that in adjoining films by studying the flow rate and length dependent coloured fringe patterns observed in the adjoining films during these studies.

While this study has essentially neglected the influence of flow in adjoining films, it has been suggested by theory that a degree of coupling between films and PBs can exist[15-17]. During the investigation of the PB-node setup, coloured fringe patterns were observed in the adjoining films, which circulated in a manner that was dependent on the liquid flow rate and PB length. As the presence of coloured fringes in thin films is well known to represent regions of localised film thinning[18], this suggested the circulation of the liquid in these films. The ability to record the circulation of these films at controlled PB liquid flow rates in the PB-node setup could be a useful tool for directly studying PB-film coupling, thus directly linking these dominant microscale foam structures.

7.3 References

1 F. Elias; E. Janiaud; J.-C. Bacri; B. Andreotti, Elasticity of a Soap Film Junction, *Physics of Fluids* **2014**, *26*, 037101.

2 O. Pitois; C. Fritz; M. Vignes-Adler, Liquid Drainage through Aqueous Foam: Study of the Flow on the Bubble Scale, *Journal of Colloid and Interface Science* **2005a**, *282*, 458-465.

3 O. Pitois; C. Fritz; M. Vignes-Adler, Hydrodynamic Resistance of a Single Foam Channel, *Colloids and Surfaces A: Physicochemical and Engineering Aspects* **2005b**, *261*, 109-114.

4 O. Pitois; N. Louvet; E. Lorenceau; F. Rouyer, Node Contribution to the Permeability of Liquid Foams, *Journal of Colloid and Interface Science* **2008**, *322*, 675-677.

5 F. Rouyer; B. Haffner; N. Louvet; Y. Khidas; O. Pitois, Foam Clogging, *Soft Matter* **2014**, *10*, 6990-6998.

6 C. Clarke; A. Lazidis; F. Spyropoulos; I. T. Norton, Measuring the Impact of Channel Length on Liquid Flow through an Ideal Plateau Border and Node System, *Soft Matter* **2019**, *15*, 1879-1889.

7 C. Clarke; F. Spyropoulos; I. T. Norton, Surface Rheological Measurements of Isolated Food Foam Systems, *Physics of Fluids* **2019**, *31*, 092002.

8 G. Verbist; D. Weaire; A. M. Kraynik, The Foam Drainage Equation, *Journal of Physics: Condensed Matter* **1996**, *8*, 3715.

9 D. Weaire; S. Hutzler; G. Verbist; E. Peters; I. Prigogine; S. A. Rice, A Review of Foam Drainage, *Advances in Chemical Physics* **1997**, *102*.

10 Z. A. Zell; A. Nowbahar; V. Mansard; L. G. Leal; S. S. Deshmukh; J. M. Mecca; C. J. Tucker; T. M. Squires, Surface Shear Inviscidity of Soluble Surfactants, *Proceedings of the National Academy of Sciences* **2014**, *111*, 3677-3682.

11 A. Saint-Jalmes; Y. Zhang; D. Langevin, Quantitative Description of Foam Drainage: Transitions with Surface Mobility, *Eur. Phys. J. E* **2004**, *15*, 53-60.

12 P. G. de Gennes, "Young" Soap Films, *Langmuir* **2001**, *17*, 2416-2419.

13 H. Vatanparast; F. Shahabi; A. Bahramian; A. Javadi; R. Miller, The Role of Electrostatic Repulsion on Increasing Surface Activity of Anionic Surfactants in the Presence of Hydrophilic Silica Nanoparticles, *Scientific Reports* **2018**, *8*, 7251.

14 A. M. Poskanzer; F. C. Goodrich, Surface Viscosity of Sodium Dodecyl Sulfate Solutions with and without Added Dodecanol, *The Journal of Physical Chemistry* **1975**, *79*, 2122-2126.

15 V. Carrier; S. Destouesse; A. Colin, Foam Drainage: A Film Contribution?, *Physical Review E* **2002**, *65*, 061404.

16 R. Phelan; D. Weaire; S. McMurry; S. J. Cox, The Deformation of Soap Film Junctions by Applied Forces, *Philosophical Magazine Letters* **1999**, *79*, 887-896.

17 F. Rouyer; E. Lorenceau; O. Pitois, Film Junction Effect on Foam Drainage, *Colloids and Surfaces A: Physicochemical and Engineering Aspects* **2008**, *324*, 234-236.

18 R. J. Pugh, *Bubble and Foam Chemistry*; Cambridge University Press: Cambridge, United Kingdom, **2016**.

Appendix A

Matlab code used in the processing of raw PB profile images

A1.1 Measuring PB Profile Geometries

The Matlab code below was written to measure the length and radius of foam channels from the raw images collected at 1mm increments along the PB length.

```
clc;
format long g;
format compact;
fontSize = 20;

c = 0.161254480773981;

ScaleFactor = 9.64285714285714; % Insert Micrometre to Pixel
conversion factor
RotFactor = -90;          % Image rotational offset
Xmin = 0;                 % Choose cropping distance [pixels] from
                            left hand side of image (remove
                            unnecessary image details)
ZeroOffset = 55;          % Choose cropping distance from top of
                            image[pixels](identify zero height of
                            channel)
cols = 2000;              % Choose width of image[pixels](starting
                            from left hand side across
rows = 1300;              % Choose height of image[pixels]
                            (starting from top down)
RGeom = 2/sqrt(3);        % Channel width to radius conversion
                            factor

Zoff = -0.72;             % Micrometre stage zero offset [mm]
Imoff = 19;               % Image increment offset [mm] (based on
                            Images taken at 1mm increments))
Offset = (Zoff+Imoff)/1000;    % Image height offset [micrometres]
                                 gives zero height of image
                                 relative to zero position of foam
                                 channel.
Img=imread('19_80ulpmin_1.tiff');% Read image with file name in
                                    Pink'increment_flowrate_repeat
                                    .file'
figure;                   % Display original image
imshow(Img)
title('Original');
```

```
RotImg = imrotate(Img,RotFactor,'bilinear'); % Rotate image by
                                               RotFactor
figure;                                      % Display rotated
                                               image
imshow(RotImg)
title('Rotated');

threshold=[0.0001, 0.05];      % Set lower and upper edge
                                 detection thresholds
BW2 = edge(RotImg,'canny',threshold);   % Use 'Canny' edge
                                          detection algorithm
figure;                                 % Display Canny edge
                                          detected image
imshow(BW2)
title('Canny Filter');

crp=imcrop(BW2,[Xmin ZeroOffset cols rows]); % Crop image[xmin
                                               ymin width height]
figure;                          % Display cropped image
imshow(crp)
title('Slice 19 @ 80ulpmin_1');

widths = zeros(rows, 1);     % Define starting row for measured
                               widths
Radii = zeros(rows, 1);      % Define starting row for widths
                               converted to radii
Height = zeros(rows, 1);     % Define starting row for distance
                               from top of image (height)
HeightSI = zeros(rows, 1);   % Define starting row for distance
                               converted to SI units
AreaSI = zeros(rows, 1);     % Define starting row for Cross-
                               sectional area in SI units
for row = 1 : rows           % Begin loop conditions for pixel row
                               by pixel row image scan
    thisRow = crp(row, :);   % Define current row
    leftPixel = find(thisRow, 1, 'first');  % Find the first
                                              black pixel (Black
                                              = 1)
    LeftScaled = leftPixel*ScaleFactor;     % Convert pixel
                                              distance to microns
    LeftRadScaled = LeftScaled*RGeom;       % Apply geometric
                                              conversion
    rightPixel = find(thisRow, 1, 'last');  % Find the last black
                                              pixel
    RightScaled = rightPixel*ScaleFactor;   % Scaling as before
```

```
    RightRadScaled = RightScaled*RGeom;
    YScaled = row*ScaleFactor;              % Convert row number
                                              to height [microns]
    if isempty(leftPixel) || isempty(rightPixel)
        continue; % Skip rows with only one pixel i.e. part of an
                    edge is missing
    end
    widths(row) = RightScaled - LeftScaled;  % Calculate and
                                               output width
    Radii(row) = RightRadScaled -  LeftRadScaled; % Calculate
                                                    radius
    Height(row) = YScaled;                   %Output Height
    AreaSI(row)= c*(((Radii(row))/1000000).^2);
    HeightSI(row) = ((Height(row))/1000000)+ Offset;
end

HeightArea = [HeightSI,AreaSI];
HeightArea(~any(HeightArea,2), : ) = [];  %remove zero or nan
                                           rows
AreaSI = HeightArea(:, 2);
HeightSI = HeightArea(:, 1);

% Remove 'missing edge' measurements
% If edges are badly defined and other edges are picked up INSIDE
the object, the loop will still measure a width between the first
and last edge in the image row. If you have a good idea of
roughly how many pixels wide your object is, you can neglect
measurements below this minimum width
OriginalMeasure = [Radii Height];
condition = OriginalMeasure(:,1) < 50;  % Set min. width [pixels]
OriginalMeasure(condition,:) = [];
RealRadii = OriginalMeasure(:,1);       % Output Radii neglecting
                                          false widths
RealHeight = OriginalMeasure(:,2);      % Rename Height
```

A1.2 Combining Incremental Profile Data into Single Profile Dataset

The following Matlab code was designed to take the height and corresponding triplicate radius data from each image increment and combine these into a single height vs. average cross-sectional area (easily converted back to radius using $S = cR^2$) dataset for the full foam channel. This is demonstrated for three image increments but can be extended to any number of increments.

```
clc;
format long g;
format compact;
fontSize = 20;

%Import raw data of heights and corresponding radii e.g. [height
1, area 1, area 2, area 3, height 2, area 2 etc.]
M = RawData;

M0 = M(1:end,1:4);
M1 = M(1:end,5:8);
M2 = M(1:end,9:12);

%Check for any nan and leave row blank if so
M0(any(isnan(M0),1),:)=[];
M1(any(isnan(M1),1),:)=[];
M2(any(isnan(M2),1),:)=[];

%Average triplicate cross-sectional area measurements
X0Av = mean([M0(:,2),M0(:,3),M0(:,4)], 2);
X1Av = mean([M1(:,2),M1(:,3),M1(:,4)], 2);
X2Av = mean([M2(:,2),M2(:,3),M2(:,4)], 2);

%Make new matrices of height vs. average area data
M0Av = [M0(:,1), X0Av];
M1Av = [M1(:,1), X1Av];
M2Av = [M2(:,1), X2Av];

%Combine profile for increments 0 and 1, averaging cross
sectional areas for overlapping heights. Outputs new matrix of
combined 0 and 1 increment profile measurements.
```

```
x = M0Av(:,1);
Val1 = M1Av(1,1);

[ d, ix ] = min( abs(x-Val1) );
x(ix-1:ix+1);

L0i = ix;
L0Av = M0Av(ix:end,1);
L1Av = M1Av(1:end-ix+1,1);
L01Av = mean([L0Av, L1Av], 2);
AVl = size(L01Av);
L01Avg = [M0Av(1:ix-1, 1); L01Av; M1Av(AVl(1)+1:end,1)];
S0Av = M0Av(ix:end,2);
S1Av = M1Av(1:end-ix+1,2);
S01Av = mean([S0Av, S1Av], 2);
AVs = size(S01Av);
S01Avg = [M0Av(1:ix-1, 2); S01Av; M1Av(AVs(1)+1:end,2)];
M01Avg = [L01Avg, S01Avg];

plot(L01Avg, S01Avg, 'b-', 'LineWidth', 2);
grid on;
xlabel('Height in Meters', 'FontSize', fontSize);
ylabel('Area in Meters Squared', 'FontSize', fontSize);

%Combine profile for combined 0-1 and 2 increment, averaging
cross sectional areas for overlapping heights. Outputs new matrix
of combined 0-2 increment profile measurements.

x = M01Avg(:,1);
Val1 = M2Av(1,1);

[ d, ix ] = min( abs(x-Val1) );
x(ix-1:ix+1);

L1i = ix;
L1Av = M01Avg(ix:end,1);
L1AvSize = size(L1Av);
L1AvL = L1AvSize(1);
L2Av = M2Av(1:L1AvL,1);
L12Av = mean([L1Av, L2Av], 2);
AVl = size(L12Av);
L12Avg = [M01Avg(1:ix-1, 1); L12Av; M2Av(AVl(1)+1:end,1)];
S1Av = M01Avg(ix:end,2);
S1AvSize = size(S1Av);
S1AvL = S1AvSize(1);
```

```
S2Av = M2Av(1:S1AvL,2);
S12Av = mean([S1Av, S2Av], 2);
AVs = size(S12Av);
S12Avg = [M01Avg(1:ix-1, 2); S12Av; M2Av(AVs(1)+1:end,2)];
M12Avg = [L12Avg, S12Avg];

plot(L12Avg, S12Avg, 'b-', 'LineWidth', 2);
grid on;
xlabel('Height in Meters', 'FontSize', fontSize);
ylabel('Area in Meters Squared', 'FontSize', fontSize);

%Output combined profile of height vs. cross-sectional area.

Raw = [L12Avg, S12Avg];
```

A1.3 Fit PB Relaxation Equation to Measured Profiles

The following code was designed to fit the profile relaxation equation (Equation 4.5) to the relaxation regions of measured channel profiles as described in Chapter 4. This code was added directly to the profile measurement code shown previously. The fitting variables, R_0, R_e and L were used to match theory to profiles and subsequently output for analysis.

```
clc;
format long g;
format compact;
fontSize = 20;

%First import data from combined profile measurement with height
as Lexp and corresponding area as Sexp. Areas are converted to
radii.
c = 0.161254480773981;
FitHeight = Lexp;
FitRadii = (Sexp/c).^0.5;


% Display the Fitting Region.
plot(FitHeight, FitRadii, 'b-', 'LineWidth', 2);
grid on;
```

```
xlabel('Height in Micrometers', 'FontSize', fontSize);
ylabel('Radius in Micrometers', 'FontSize', fontSize);

%Curve Fitting (calls function createFit detailed below)
[fit2, gof] = createFit(FitHeight, FitRadii);

%Export Coefficients
Coeff = coeffvalues(fit2);
L = Coeff(1);
Re = Coeff(2);
Ro = Coeff(3);
%Determine R-Square value
Rsqr = gof.rsquare;

Outputs = [Rsqr, Ro, Re, L];


%The fitting function 'createFit' was defined in a separate
command file and linked to the code above.

function [fit2, gof] = createFit(FitHeight, FitRadii)

%% Fit: 'Data_Fit'.
[xData, yData] = prepareCurveData( FitHeight, FitRadii );

% Set up fittype and options.
ft = fittype( 'Re + ((Ro-Re)*exp(((-1)*x)/L))', 'independent',
'x', 'dependent', 'y' );
opts = fitoptions( 'Method', 'NonlinearLeastSquares' );
opts.Display = 'Off';
opts.Lower = [10 0 0];
opts.StartPoint = [1000 100 150];

% Fit model to data.
fitresult = fit( xData, yData, ft, opts );


%Identify and remove outliers caused incorrect image edges.
fdata = feval(fitresult,xData);
CheckOutliers = abs(fdata - yData) > 0.5*std(yData);
outliers = excludedata(xData, yData,'indices',CheckOutliers);
opts2 = fitoptions( 'Method', 'NonlinearLeastSquares' );
opts2.Display = 'Off';
opts2.Lower = [10 0 0];
opts2.StartPoint = [1000 100 150];
```

```
opts2.Exclude = outliers;

%Fit Curve to data with outliers removed
[fit2, gof] = fit(xData,yData,ft,opts2);

% Plot fit with data.
figure( 'Name', 'Data_Fit' );
h2 = plot( fit2, xData, yData, outliers);
%outliers here indicates highlight of outliers in diff colour
legend( h2, 'PB Radii vs. Height NO OUTLIERS', 'Fitted Theory',
'Location', 'NorthEast' );
% Label axes
xlabel FitHeight
ylabel FitRadii
grid on

end
```

Appendix B

Derivation of key equations

B1.1 Derivation of the Standard Drainage Theory

Equations (4.5), (5.1) and (6.1) describe the standard drainage theory when applied to an ideal vertical PB with liquid flow field, $\vec{u}$. An abridged version of the full derivation provided by Elias *et al.*[17] is given here in order to provide context, although it is recommended that readers refer to Elias *et al.*[17] for further detail.

Equations (4.5), (5.1) and (6.1) are ultimately derived from the Navier-Stokes equation for fluid momentum (Equation (B1)) where P is the pressure and $\vec{f}$ is the external volume force. $\vec{f}$ itself can be described as the summation of the two forces $\overrightarrow{f_l}$ and $\overrightarrow{f_r}$ (Equation (B2)), where the volume force, $\overrightarrow{f_l}$, includes a 'line tension' effect due to the minimisation of PB surface energy and $\overrightarrow{f_r}$ is the elastic restoring force exerted on the PB by its three adjoining films.

$$\frac{d\vec{u}}{dt} = \vec{g} + \nu\Delta\vec{u} + \left(\vec{f} - \vec{\nabla}P\right)/\rho \tag{B1}$$

$$\vec{f} = \overrightarrow{f_l} + \overrightarrow{f_r} \tag{B2}$$

The surface free energy of the PB can be expressed as $E_s = -2\gamma l_1 cR$, where l_1 describes the length of the PB. At this point, we must also introduce a curvilinear coordinate, $\overrightarrow{s_v}$, which follows any deformation in the PB, a vector tangential to the PB, $\overrightarrow{t_v}$, and a vector normal to the PB, $\overrightarrow{n_v}$. The 'line tension', $\vec{T}$, of the PB is then expressed as:

$$\vec{T} = \frac{\partial(E_s)}{\partial l_1|_V \overrightarrow{t_v}} = -\gamma cR\overrightarrow{t_v} \tag{B3}$$

From this, we can derive the external volume force acting on the PB element between s_v and ds_v as:

$$\overrightarrow{f_l} = \left(\frac{1}{cR^2 ds_v}\right)\frac{d\vec{T}}{ds_v}ds_v = -\frac{\gamma}{R^2}\frac{dR}{ds_v}\overrightarrow{t_v} - \frac{\gamma}{R}\frac{d\overrightarrow{t_v}}{ds_v} \tag{B4}$$

Finally a force per unit length exerted by the three films is introduced in the form of Equation (B5) where $\vec{\chi}$ is a dimensionless vector and $S = cR^2$ is the PB cross-sectional area. A specific derivation of $\vec{\chi}$ can be found in Elias *et al.*[17].

$$\gamma\vec{\chi}=S\overrightarrow{f_r} \tag{B5}$$

At this point, we must also introduce the variables D and I, which are defined in Equations (5.5) and (6.6), and (5.6) and (6.7) respectively in the main manuscript, and describe the viscous and inertial terms of the fluid flow. These were obtained by averaging across the PB horizontal cross-section[17], and can ultimately be used to describe the shape of the liquid flow velocity profiles.

$$D = -R^2\overline{\Delta u}/\bar{u} \tag{5.5, 6.6}$$

$$I = \overline{u^2}/_{\bar{u}^2} \tag{5.6, 6.7}$$

When in the steady state, substituting Equations(B4), (B5), (5.5, 6.6) and (5.6, 6.7) into Equation (B1) becomes:

$$I(\vec{\bar{u}}\cdot\vec{\nabla})\vec{\bar{u}} = \vec{g} - \frac{Dv}{R^2}\vec{\bar{u}} - \frac{\gamma}{\rho R^2}\frac{dR}{ds_v}\overrightarrow{t_v} - \frac{\gamma}{\rho R}\frac{d\overrightarrow{t_v}}{ds_v} + \frac{\gamma\vec{\chi}}{\rho cR^2} \tag{B6}$$

As $\vec{\bar{u}}$ is tangential to the PB axis, this can be rewritten as Equation (B7), where the parameter, κ, is introduced to describe the curvature in the vertical plane.

$$I\left[\bar{u}^2\kappa\overrightarrow{n_v} + \bar{u}\frac{d\bar{u}}{ds_v}\overrightarrow{t_v}\right] = \vec{g} - \frac{Dv}{R^2}\bar{u}\overrightarrow{t_v} - \frac{\gamma}{\rho R^2}\frac{dR}{ds_v}\overrightarrow{t_v} - \frac{\gamma}{\rho R}\kappa\overrightarrow{n_v} + \frac{\gamma\vec{\chi}}{\rho cR^2} \tag{B7}$$

In the ideal case of a vertical, undistorted PB, Equation (B7) can be projected along the tangential vector to yield Equations (4.5), (5.1) and (6.1), where the curvilinear coordinate s_v becomes equivalent to the

vertical coordinate Z. Here, the definition $\bar{u} = Q/cR^2$ is used to describe the relationship between liquid flow rate and average flow velocity across the PB horizontal cross-section.

$$\frac{dR}{dZ} = \frac{cDvQ \quad {}^2R^4}{\left(\frac{2IQ^2}{R}\right) - \left(\frac{c^2R^2\gamma}{\rho}\right)} \qquad (4.5, 5.1, 6.1)$$